



**QUEEN'S  
UNIVERSITY  
BELFAST**

## Chemical tracers of a highly eccentric AGB-main-sequence star binary

Danilovich, T., Malfait, J., Sande, M. V. D., Montarges, M., Kervella, P., De Ceuster, F., Coenegrachts, A., Millar, T. J., Richards, A. M. S., Decin, L., Gottlieb, C. A., Pinte, C., De Beck, E., Price, D. J., Wong, K. T., Bolte, J., Menten, K., Baudry, A., de Koter, A., ... Zijlstra, A. A. (2024). Chemical tracers of a highly eccentric AGB-main-sequence star binary. *Nature Astronomy*, 8, 308-327. <https://doi.org/10.1038/s41550-023-02154-y>

**Published in:**  
Nature Astronomy

**Document Version:**  
Peer reviewed version

**Queen's University Belfast - Research Portal:**  
[Link to publication record in Queen's University Belfast Research Portal](#)

**Publisher rights**  
Copyright 2024 The Authors  
This work is made available online in accordance with the publisher's policies. Please refer to any applicable terms of use of the publisher.

**General rights**  
Copyright for the publications made accessible via the Queen's University Belfast Research Portal is retained by the author(s) and / or other copyright owners and it is a condition of accessing these publications that users recognise and abide by the legal requirements associated with these rights.

**Take down policy**  
The Research Portal is Queen's institutional repository that provides access to Queen's research output. Every effort has been made to ensure that content in the Research Portal does not infringe any person's rights, or applicable UK laws. If you discover content in the Research Portal that you believe breaches copyright or violates any law, please contact [openaccess@qub.ac.uk](mailto:openaccess@qub.ac.uk).

**Open Access**  
This research has been made openly available by Queen's academics and its Open Research team. We would love to hear how access to this research benefits you. – Share your feedback with us: <http://go.qub.ac.uk/oa-feedback>

# 1 Chemical tracers of a highly eccentric binary orbit

2 T. Danilovich<sup>1,2</sup>, J. Malfait<sup>1</sup>, M. Van de Sande<sup>3</sup>, M. Montargès<sup>4</sup>, P. Kervella<sup>4</sup>,  
3 F. De Ceuster<sup>1</sup>, A. Coenegrachts<sup>1</sup>, T. J. Millar<sup>5</sup>, A. M. S. Richards<sup>6</sup>, L. Decin<sup>1,7</sup>,  
4 C. A. Gottlieb<sup>8</sup>, C. Pinte<sup>2,9</sup>, E. De Beck<sup>10</sup>, D. J. Price<sup>2</sup>, K. T. Wong<sup>11</sup>, J. Bolte<sup>12,1</sup>,  
5 K. M. Menten<sup>13</sup>, A. Baudry<sup>14</sup>, A. de Koter<sup>15,1</sup>, S. Etoka<sup>6</sup>, D. Gobrecht<sup>16</sup>, M. Gray<sup>6,17</sup>,  
6 F. Herpin<sup>14</sup>, M. Jeste<sup>13</sup>, E. Lagadec<sup>18</sup>, S. Maes<sup>1</sup>, I. McDonald<sup>6,19</sup>, L. Marinho<sup>14</sup>,  
7 H. S. P. Müller<sup>20</sup>, B. Pimpanuwat<sup>6,17</sup>, J. M. C. Plane<sup>7</sup>, R. Sahai<sup>21</sup>, S. H. J. Wallström<sup>1</sup>,  
8 J. Yates<sup>22</sup>, and A. Zijlstra<sup>6</sup>

9 <sup>1</sup>Institute of Astronomy, KU Leuven, Celestijnenlaan 200D, 3001 Leuven, Belgium

10 <sup>2</sup>School of Physics & Astronomy, Monash University, Wellington Road, Clayton 3800, Victoria, Australia

11 <sup>3</sup>School of Physics and Astronomy, University of Leeds, Leeds LS2 9JT, UK

12 <sup>4</sup>LESIA, Observatoire de Paris, Université PSL, CNRS, Sorbonne Université, Université Paris Cité, 5 place Jules  
13 Janssen, 92195 Meudon, France

14 <sup>5</sup>Astrophysics Research Centre, School of Mathematics and Physics, Queen's University Belfast, University Road,  
15 Belfast BT7 1NN, UK

16 <sup>6</sup>JBCA, Department Physics and Astronomy, University of Manchester, Manchester M13 9PL, UK

17 <sup>7</sup>School of Chemistry, University of Leeds, Leeds LS2 9JT, UK

18 <sup>8</sup>Harvard-Smithsonian Center for Astrophysics, 60 Garden Street, Cambridge, MA 02138, USA

19 <sup>9</sup>Univ. Grenoble Alpes, CNRS, IPAG, Grenoble, France

20 <sup>10</sup>Department of Space, Earth and Environment, Chalmers University of Technology, Onsala Space Observatory,  
21 43992 Onsala, Sweden

22 <sup>11</sup>Theoretical Astrophysics, Division for Astronomy and Space Physics, Department of Physics and Astronomy,  
23 Uppsala University, Box 516, SE-751 20 Uppsala, Sweden

24 <sup>12</sup>Department of Mathematics, Kiel University, Heinrich-Hecht-Platz 6, 24118 Kiel, Germany

25 <sup>13</sup>Max-Planck-Institut für Radioastronomie, 53121 Bonn, Germany

26 <sup>14</sup>Université de Bordeaux, Laboratoire d'Astrophysique de Bordeaux, 33615 Pessac, France

27 <sup>15</sup>University of Amsterdam, Anton Pannekoek Institute for Astronomy, 1090 GE Amsterdam, The Netherlands

28 <sup>16</sup>Department of Chemistry and Molecular Biology, University of Gothenburg, Kemigården 4, 412 96 Gothenburg,  
29 Sweden

30 <sup>17</sup>National Astronomical Research Institute of Thailand, Chiangmai 50180, Thailand

31 <sup>18</sup>Université Côte d'Azur, Laboratoire Lagrange, Observatoire de la Côte d'Azur, F-06304 Nice Cedex 4, France

32 <sup>19</sup>School of Physical Sciences, The Open University, Walton Hall, Milton Keynes, MK7 6AA, UK

33 <sup>20</sup>Universität zu Köln, I. Physikalisches Institut, 50937 Köln, Germany

34 <sup>21</sup>California Institute of Technology, Jet Propulsion Laboratory, Pasadena CA 91109, USA

35 <sup>22</sup>University College London, Department of Physics and Astronomy, London WC1E 6BT, United Kingdom

## 36 Abstract

37 Binary interactions have been proposed to explain a variety of circumstellar structures  
38 seen around evolved stars, including asymptotic giant branch (AGB) stars and plane-  
39 tary nebulae. Studies resolving the circumstellar envelopes of AGB stars have revealed

40 spirals, discs and bipolar outflows, with shaping attributed to interactions with a com-  
41 panion. For the first time, we have used a combined chemical and dynamical analysis to  
42 reveal a highly eccentric and long-period orbit for W Aquilae, a binary system contain-  
43 ing an AGB star and a main sequence companion. Our results are based on anisotropic  
44 SiN emission, the first detections of NS and SiC towards an S-type star, and density  
45 structures observed in the CO emission. These features are all interpreted as having  
46 formed during periastron interactions. Our astrochemistry-based method can yield strin-  
47 gent constraints on the orbital parameters of long-period binaries containing AGB stars,  
48 and will be applicable to other systems.

## 49 Main

50 The asymptotic giant branch (AGB) is a late evolutionary stage of low and intermediate  
51 mass stars ( $\sim 1$  to 8 solar masses,  $M_{\odot}$ ). This stage is characterised by mass-losing stellar  
52 winds, rich in molecular gas and dust, which form an extended, expanding circumstel-  
53 lar envelope (CSE) around the star [1]. AGB stars eventually transition through the  
54 planetary nebula phase and end as white dwarf stars, having chemically enriched their  
55 host galaxies through their mass loss [2]. Binary companions can have a significant im-  
56 pact on this process, potentially affecting mass-loss rates and chemistry [3, 4], and are  
57 thought to shape both the eventual planetary nebula [5] and the CSE during the AGB  
58 phase [6]. Binary stars with an AGB component are also the progenitors of various ex-  
59 otic objects, including Barium stars, CH stars, extrinsic S-stars, and novae [7]. Hence,  
60 understanding binary systems containing AGB stars, especially through observations,  
61 is important for understanding their overall evolutionary progress, the initial-final mass  
62 relation, and the evolution of their host galaxies.

63 Recent observations of some AGB stars have identified the signatures of binary com-  
64 panions imprinted in the structure of the CSE. In only a few cases, however, is the pre-  
65 cise nature of the companion and its effects on the CSE known, thereby limiting the  
66 study of such systems. Systems with directly detected companions include Mira, which  
67 comprises an oxygen-rich AGB star and a white dwarf, in which the companion has  
68 contributed to the shaping of the CSE structure [8, 9], and L<sub>2</sub> Pup, an oxygen-rich AGB  
69 star surrounded by a disc with a planetary companion [10]. Bipolar structures around  
70  $\pi^1$  Gru have been attributed to a recently detected close companion [11], adding to the  
71 small number of AGB systems with directly detected companions. The spiral structures  
72 observed around the carbon stars AFGL 3068 and R Scl [12, 13, 14], and the bipolar  
73 structures around the carbon star V Hya [15], indicate the possible presence of binary  
74 companions that have not been directly detected. A more complete understanding of  
75 circumstellar structures will come from knowing both cause (e.g. a stellar or plane-  
76 tary companion) and effect (the CSE structure) and should allow us to draw more direct  
77 links between AGB stars and planetary nebulae, which have been observed to display a

78 multitude of complex asymmetric structures [16, 6].

79 W Aquilae (W Aql) is a binary system at a distance of 395 pc (Methods 3.1). It con-  
80 tains an S-type AGB star, which has a mixed carbon-oxygen chemistry ( $C/O \sim 1$ ) and  
81 may be transitioning from being oxygen-rich to carbon-rich, and an F9 main sequence  
82 star [17, 18] located to the southwest of the AGB star at a projected separation of  $\sim 0.5''$   
83 [19]. W Aql has been extensively studied through observations taken with a variety  
84 of telescopes [19, 20, 21, 22, 23, 24]. Spatially resolved observations of the polarised  
85 dust [19] and CO [22] around the AGB star have shown a large-scale asymmetry in the  
86 direction of the F9 companion, a sign that binary interactions may be shaping the CSE.  
87 However, the asymmetry exists at larger scales than the present separation of the two  
88 stars, from  $\sim 10''$  to  $\sim 100''$  [19, 22, 20]. Some indications of spiral structure in the  
89 CSE were seen in observations taken by the Atacama Large Millimetre/submillimetre  
90 Array (ALMA) at a resolution of  $\sim 0.4''$  [22] but it was unclear whether these could be  
91 caused by the F9 star.

## 92 1 Results

93 We have analysed new, high resolution ALMA observations of the W Aql system with  
94 spatial resolutions to  $\sim 0.024''$ , i.e. approximately twice the K-band stellar diameter  
95 [25], and 40% larger than the millimetre stellar diameter (Methods 3.4.2). We com-  
96 bined these with photometric observations, new smooth particle hydrodynamics mod-  
97 els, and chemical kinetics models to put new constraints on the orbit of the system. [We](#)  
98 [have shown that all the observations are consistent with the hypothesis of a highly ec-](#)  
99 [centric orbit, based primarily on the distributions of molecular species which formed](#)  
100 [during periastron passage and the structures seen in the CO observations, making such](#)  
101 [an interpretation highly probable.](#)

### 102 1.1 Species formed during periastron passage

103 From a detailed examination of the ALMA data (Methods 3.4), we identified several  
104 molecules exhibiting spatially asymmetric emission. Most notable was SiN, which has  
105 only been detected towards one other AGB CSE [26]. In Fig. 1a we plot a zeroth  
106 moment (integrated intensity) map of SiN, which shows emission in a roughly triangular  
107 wedge mainly to the northeast of the AGB star. To further understand the spatial origin  
108 of the emission, we constructed a position-velocity diagram (Fig. 1b), which reveals an  
109 arc of SiN emission that lies side-on ( $90^\circ$ ), i.e. perpendicular to the plane of the sky  
110 (Methods 3.4.3).

111 The absence of (approximate) spherical symmetry in the emission suggests a spatial  
112 and/or temporal dependence for the formation of SiN around W Aql. Chemical kinetics  
113 models indicate that the production of SiN is higher in the presence of UV photons —

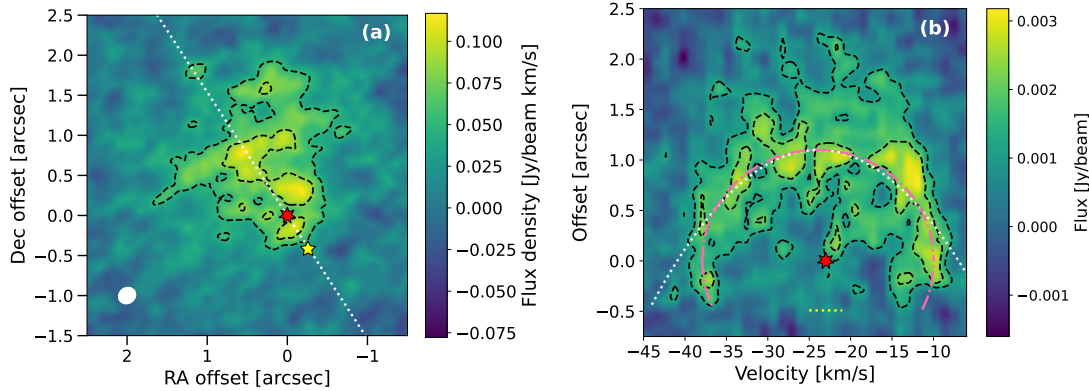


Figure 1: **(a)** Zeroth moment map of SiN ( $N, J = 6, 13/2 \rightarrow 5, 11/2$ ) towards W Aql with contours at levels of  $3$  and  $5\sigma$ . The position of the AGB star is indicated by the red star at  $(0,0)$  and the current location of the F9 star is indicated by the yellow star to the southwest. North is up and east is to the left. The dotted white line indicates the axis used for the PV diagram in (b) and the white ellipse in the bottom left corner indicates the size of the synthesised beam. **(b)** Position-velocity diagram of SiN towards W Aql, taken at a position angle of north  $33^\circ$  east, as indicated by the dotted white line in (a). Dashed black contours are at levels of  $3$  and  $5\sigma$ , a dotted white parabola is fit to the data (see Methods 3.4.3), and a dash-dotted pink ellipse is plotted to emphasise the shape of the emission in the PV diagram. The position and LSR velocity ( $v_{\text{LSR}} = -23 \text{ km s}^{-1}$ ) of the AGB star is indicated by the red star, and the horizontal yellow dotted line indicates the present offset of the F9 star.

114 such as can be provided by a main sequence companion [4] like the F9 component of  
 115 W Aql, but only in sufficiently dense regions of the CSE (see Methods 3.6 for further  
 116 details of the chemistry initiated by the companion's UV field). We posit that: (1) the  
 117 binary orbit is highly eccentric and inclined  $i \sim 90^\circ$ ; (2) the formation of the arc of SiN  
 118 was triggered close to periastron (Figs. 4 and A.10), when the F9 star passed close to  
 119 the AGB star and irradiated part of the dense inner AGB wind; and (3) this temporarily  
 120 drove chemical reactions through increased (but not complete) photodissociation and  
 121 photoionisation, including those reactions which led to the formation of SiN (Methods  
 122 3.6.1). We used radiative transfer modelling to estimate the abundance of SiN in the  
 123 arc and found a peak abundance of  $1.5 \times 10^{-7}$  relative to  $\text{H}_2$  (Methods 3.5), which is in  
 124 general agreement with the expectations from chemical models containing an F9-like  
 125 companion (Methods 3.6.1). Further evidence in support of this formation mechanism  
 126 is provided by the presence of SiC and NS emission towards W Aql. These are the  
 127 first detections of SiC and NS towards an S-type AGB star and their emission is also  
 128 asymmetric (with a weaker signal to noise ratio (SNR) than SiN; see Methods 3.4.3 and

129 3.4.4, and Figs A.5 and B.15 in the Extended Data and Supplementary Materials). The  
130 presence of SiC and NS is consistent with chemical model predictions [4] for the effect  
131 of the periastron passage of the F9 star on the chemistry of the CSE (Methods 3.6.1 and  
132 3.6.2).

## 133 1.2 Photodissociation of common species

134 Farther from the AGB star, such as where the F9 star is presently located, the wind is  
135 less dense ( $\sim 3 \times 10^5 \text{ cm}^{-3}$  compared with  $\sim 10^9 \text{ cm}^{-3}$  at 10 au from the AGB star)  
136 and the chemistry tends to be initiated by photodissociation by the interstellar radiation  
137 field. The density in this region is too low for species like SiN to form, however, we see  
138 evidence of the F9 star driving additional photodissociation in the zeroth moment maps  
139 of SiO, SiS, CS and HCN (Fig. A.6 in the Extended Data), all of which show extended  
140 emission to the northeast and truncated emission to the southwest, in the direction of the  
141 present position of the F9 star. The central channels of SiS and CS, in particular, show  
142 significantly lower molecular emission around the F9 star (Fig. B.18 in the Supplemen-  
143 tary Materials). Spectra centred on the current position of the F9 star show very few  
144 detected molecular lines and the line profiles of CS, SiO and HCN show less emission  
145 around the LSR velocity compared with spectra centred on the AGB star or at the same  
146 distance from the AGB star but on the opposite side of the CSE (see Methods 3.4.8 and  
147 Fig. A.9 in the Extended Data).

148 Additional evidence of the F9 star driving photodissociation is found by comparing  
149 the distribution of  $\text{H}^{13}\text{CN}$  with the distribution of  $^{13}\text{CN}$  (note,  $^{12}\text{CN}$  was not covered by  
150 our observations), because CN is a photodissociation product of HCN [27]. As shown  
151 in Fig. 2,  $^{13}\text{CN}$  is found to be present mainly in the region in which the  $\text{H}^{13}\text{CN}$  emission  
152 is truncated. This is consistent with the F9 star driving the photodissociation of  $\text{H}^{13}\text{CN}$   
153 and hence creating  $^{13}\text{CN}$ . We also plot the zeroth moment map of the  $J = 27 - 26$   
154 transition of HCCCN (the next member in the cyanopolyne family, hereafter  $\text{HC}_3\text{N}$ ,  
155 see Fig. 2), which shows emission on the same side of the AGB star as  $^{13}\text{CN}$ , albeit  
156 over a much smaller region. The other observed transitions of  $\text{HC}_3\text{N}$  show a similar  
157 distribution (Fig. B.16 in the Supplementary Materials). Because  $\text{HC}_3\text{N}$  forms from CN  
158 (Methods 3.6.3), its asymmetric distribution indicates an asymmetric CN distribution  
159 and hence provides further evidence of anisotropic photo-processes in the CSE.

## 160 1.3 Structures in CO emission

161 CO is an abundant stable molecule, commonly used as a density tracer in CSEs. We  
162 plot high resolution ( $0.132'' \times 0.123''$ ) channel maps of CO emission in Fig. A.7 in the  
163 Extended Data and first focus on the central three channels closest to the AGB stellar  
164 velocity  $v_{\text{LSR}} = -23 \text{ km s}^{-1}$  (Fig. 3a). With the aid of angle-radius plots (Fig. A.8),  
165 we identified two key circular structures in the CO emission, with radii of  $1.35''$  and

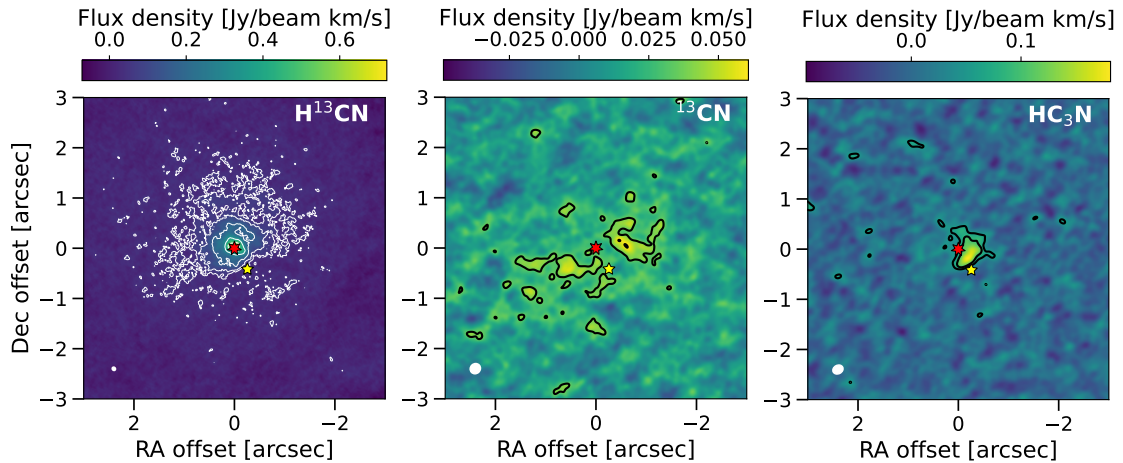


Figure 2: Zeroth moment maps of  $\text{H}^{13}\text{CN}$  (left),  $^{13}\text{CN}$  (centre), and  $\text{HC}_3\text{N}$  ( $J = 27 \rightarrow 26$ , right) towards W Aql. Full transition details are given in Table 1. Contours are at levels of  $3$  and  $5\sigma$ , and additionally  $10$ ,  $20$ , and  $30\sigma$  for  $\text{H}^{13}\text{CN}$ . The position of the AGB star is indicated by the red star at  $(0,0)$  and the location of the F9 companion is indicated by the yellow star to the southwest. North is up and east is left. The white ellipses in the bottom left corners indicate the sizes of the synthesised beams.

166 10.75'', with centres offset from the present position of the AGB star by 0.1'' and 1.5''  
 167 to the north. These are shown in black and white in Fig. 3a. Other circular structures are  
 168 highlighted in red and pink and, because these are offset to the southwest, we presume  
 169 they were formed through different processes to the black and white circles and focus  
 170 on the latter first.

171 To better understand the origin of the circular structures, we performed hydrody-  
 172 namic simulations for highly eccentric systems based on the W Aql system (details in  
 173 Methods 3.7). From these we found that highly elliptical orbits ( $e \gtrsim 0.8$ ) result in almost  
 174 spherical structures in the wind, which appear circular and slightly offset away from the  
 175 present position of the companion when viewed edge-on ( $i = 90^\circ$ ) relative to the plane  
 176 of the orbit (Fig. 3c). These structures are generated during periastron passages and are  
 177 very similar to the black and white circles seen in the ALMA CO data, even more so  
 178 when the hydrodynamical model is processed with a radiative transfer code (Fig. 3d).  
 179 The fact that the outer edge of the SiN emission overlaps with the inner circular struc-  
 180 ture (Fig. 3b) also suggests they were formed contemporaneously, i.e. during the most  
 181 recent periastron passage. We also determined that the different emission distributions  
 182 seen in blue (elongated) and red (circular) channels of our ALMA observations are re-  
 183 produced in the hydrodynamic model (Fig. A.12). Based on all of these results, we can  
 184 constrain the orbital parameters of the W Aql system.

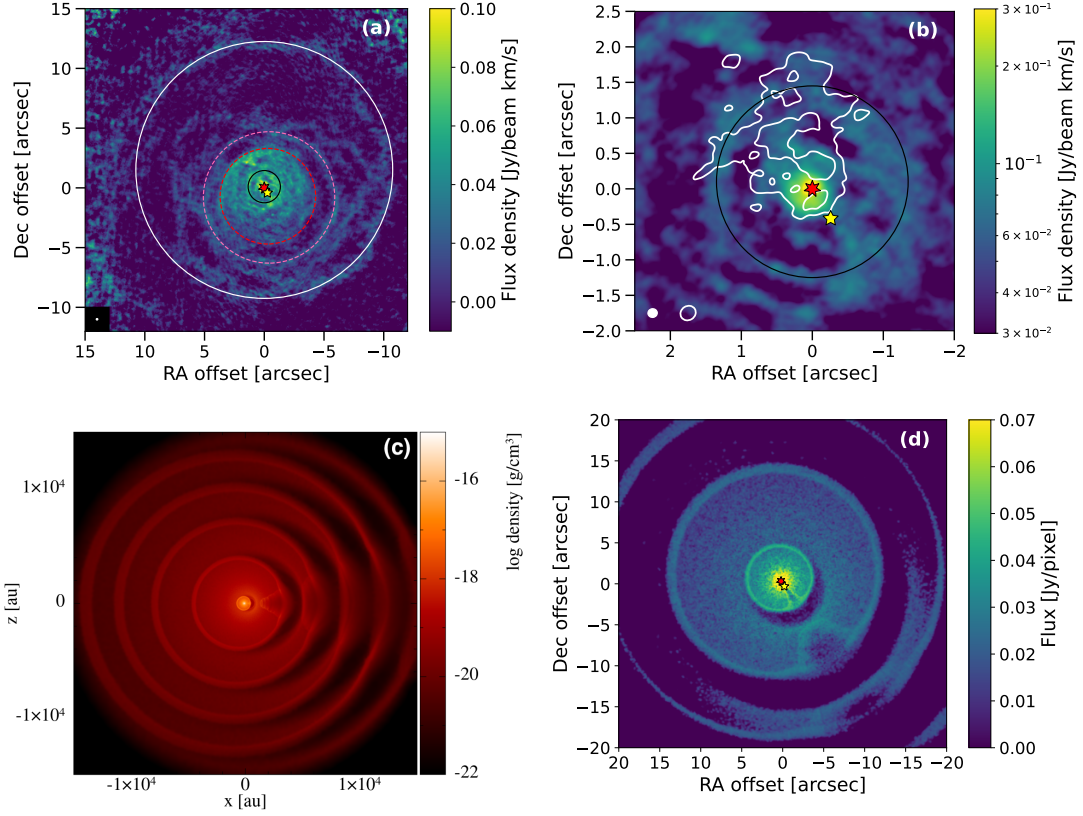


Figure 3: **(a)** A plot of the three central CO channels observed with ALMA summed together (see channels highlighted in Fig. A.7). We include circles (white, black, red, pink) to guide the eye to structures in the emission. The location of the AGB star is shown as a red star and the present location of the companion is shown as a yellow star. North is up and east is left. The synthetic beam size is shown as a white ellipse inside a black square in the bottom left corner. **(b)** Same as the central part of (a), including the black circle, but plotted on a logarithmic colour scale to emphasise structure. The white contours are the SiN zeroth moment map as shown in Fig. 1(a). The filled ellipse in the bottom left corner shows the synthetic beam for the CO data, while the unfilled ellipse is the synthetic beam of the SiN data. **(c)** Density distribution in a 2D slice through a plane perpendicular to the orbital plane ( $y = 0$ ), similar to the edge-on orientation of the W Aql system, from a 3D SPH model with masses  $M_{\text{AGB}} = 1.6 M_{\odot}$  and  $M_2 = 1.06 M_{\odot}$ , eccentricity  $e = 0.92$ , and semimajor axis  $a = 125$  au. The barycentre of the system is located at 0,0 and at the scale plotted ( $1 \times 10^4$  au  $\approx 25''$ ) the AGB and F9 stars cannot be distinguished. See Methods 3.7 for more details. **(d)** The central channel of (c) after processing with a radiative transfer model to convert the model density to CO ( $2 \rightarrow 1$ ) intensity, taking photodissociation into account (see Methods 3.7 for details). Star positions are taken from the model in (c).



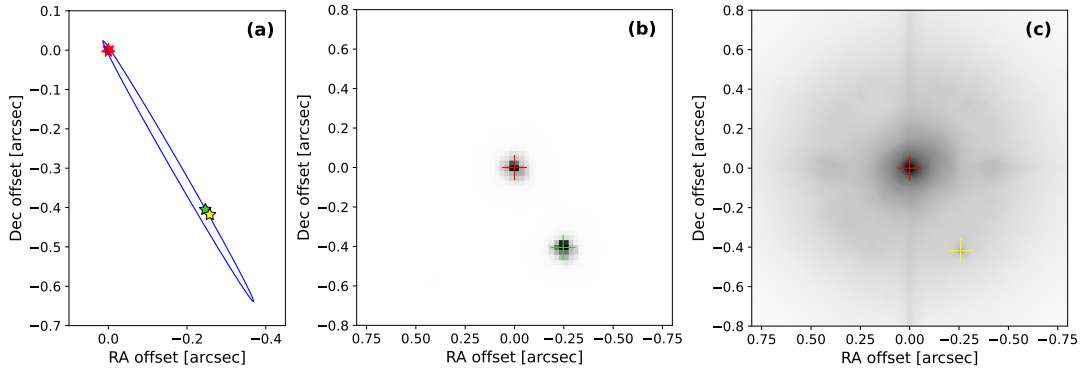


Figure 4: Plots of the orbit of the W Aql system as seen in the plane of the sky. In all panels, north is up and east is left. The orbital parameters shown are for eccentricity  $e = 0.93$  and periastron separation  $r_p = 1.5 \times 10^{14}$  cm. Although we find the inclination to be  $i = 90 \pm 7^\circ$ , we plot the orbit with  $i = 85^\circ$  so that it is possible to see the ellipse. **(a)** Plot of the orbit of the W Aql system in the frame of the AGB star. The location of the AGB star is shown as a red star at (0,0), the position of the F9 star from the SPHERE observation is shown as a yellow star and from the HST observation as a green star. **(b)** B-band image of W Aql observed with HST in 2004 [19], plotted with a linear intensity scale. The measured centres of the AGB and F9 stars are indicated with the red and green crosses, respectively. **(c)** VLT/SPHERE-ZIMPOL image of W Aql in the VBB filter, observed in 2019 [28], plotted with a logarithmic intensity scale. The measured centres of the AGB and F9 stars are indicated with the red and yellow crosses, respectively.

## 185 1.4 Orbital parameters

186 From the circular structures seen in Fig. 3, we estimate the orbital period to be  $1082^{+89}_{-108}$   
 187 years. Based on the expansion time of the inner circle and the arc of SiN, we estimate  
 188 the time since the most recent periastron to be  $172 \pm 22$  years (Methods 3.8). The SiN PV  
 189 diagram indicates an orbital inclination of  $i = 90 \pm 7^\circ$  (Methods 3.4.3). Combining these  
 190 results with resolved images of W Aql (Methods 3.3), we found a series of numerical  
 191 solutions that reproduce the observations within their uncertainties (Methods 3.9). All  
 192 our solutions (Table A.3 in the Extended Data) have high eccentricities ( $e > 0.9$ ) and  
 193 small periastron distances ( $r_p \leq 2 \times 10^{14}$  cm = 13 au), with long periods  $\sim 1100$  years.  
 194 A solution with  $e = 0.93$ ,  $r_p = 1.5 \times 10^{14}$  cm (10 au) and period 1051 years is plotted  
 195 in Fig. 4, where it is superposed on resolved images to show the agreement with the  
 196 positions of the stars.

## 2 Discussion

For the first time, we have identified in observations, with the aid of astrochemistry, molecular species that formed during a periastron passage of an AGB + main sequence (F9) binary system. Through our analysis of these species, in combination with structures in the CO and resolved images of the two stars, we were able to constrain the binary orbit to a limited number of solutions, all having high eccentricities and almost edge-on inclinations. Our analysis opens up a new method for studying binary systems containing AGB stars by observing spatially resolved emission of key molecular species.

SiN was crucial to our analysis because it is distributed asymmetrically in the W Aql CSE — alerting us to a non-standard formation pathway — and was detected with a sufficiently high SNR to be readily analysed. The other two molecules that we identified as being created during periastron, SiC and NS, strengthened our argument but their lower SNR in the present observations would not have allowed us to draw firm conclusions in the absence of SiN. However, we note that all three molecules have the potential to serve as diagnostic tools for identifying binary interactions in other systems, especially with targeted observations at high SNR. Based on the predictions of chemical models that consider the presence of a Sun-like companion [4], SiN and SiC are expected to be good tracers of stellar companions to S-type and oxygen-rich AGB stars, but probably not carbon stars (unless notably asymmetric emission is detected), because carbon-rich CSEs are expected to have higher abundances of both molecules without the presence of a companion. NS is predicted to have higher abundances around carbon stars in the presence of a white dwarf companion, but not if the companion is a main-sequence star. For S-type and oxygen-rich AGB stars, NS is expected to be a good tracer of either a white dwarf or a Sun-like companion. While there may be other molecules that are enhanced or destroyed in the presence of a companion, a comprehensive list is difficult to compile [4]. After checking all detected molecular lines for asymmetries, we do not find any additional candidates for tracers of binary-induced chemistry towards W Aql.

The timing between our observations and the present orbital configuration of W Aql contributed to our being able to use SiN to characterise the orbit. If the W Aql system was instead observed  $\sim 200$  years prior to the next periastron, rather than  $\sim 200$  after the most recent periastron, it is unlikely that SiN would have been detected. In that case, in the  $\sim 900$  years since the previous periastron, the SiN arc would have expanded with the CSE to around 4 times farther from the AGB star than what we presently observe. At that radial distance, most of the SiN would have been destroyed through photodissociation by the interstellar radiation field [4]. This is also why we do not detect SiN that was created contemporaneously with the white circle in CO (Fig. 3a) during the second most recent periastron passage,  $\sim 1300$  years ago. **That said, SiN has already persisted for  $\sim 200$  years since the periastron interaction, and may continue to be detectable for another 50 to 100 years, based on the expansion velocity and excitation**

237 conditions. This means that the imprint of the periastron interaction will be potentially  
238 detectable for around a quarter of the total orbital period, a much larger portion than if  
239 we had to rely on, for example, observing changing stellar positions or radial velocities  
240 around periastron (see Table A.3). The high eccentricity and small periastron separation  
241 of the system also contributed to favourable conditions for the formation of SiN around  
242 W Aql. As noted above and in Methods 3.6, the companion-initiated photochemistry is  
243 most impactful in the dense inner CSE, meaning that the tracers of this photochemistry  
244 — SiN, SiC and NS — may not be formed in sufficiently high quantities to be detected  
245 for binary systems with wider orbits, where the companion passes through regions of the  
246 CSE with lower number densities. Despite these potential limitations, molecular tracers  
247 in the CSE generally persist for a relatively long time (hundreds of years, depending on  
248 the molecule) and allow us to probe the system on longer time scales than direct imaging  
249 or radial velocity measurements, which can only be taken on human timescales. Hence,  
250 molecular tracers are invaluable for constraining binary systems with long orbital peri-  
251 ods.

252 The W Aql system may be unusual for having such a highly eccentric orbit, but it is  
253 not unique nor is it impossible for it to have formed with such a high eccentricity. In fact,  
254 studies of eccentricity distributions that include wider binaries find a tendency for the  
255 mean eccentricity to be higher for subsamples with larger periods [29, 30]. Indeed, for  
256 long-period binaries, orbital circularisation during their formation is not expected [31].  
257 Furthermore, a large statistical analysis of binary systems found that solar-type stars  
258 in binaries are more likely to have long periods than short periods, i.e. the companion  
259 frequency distribution for solar-type primaries peaked at periods of  $\log P[\text{days}] = 5.5$   
260 [31], very close to the period we found for W Aql ( $\log P_{\text{WAql}}[\text{days}] = 5.6$ ). Both the  
261 aforementioned studies focussed primarily on main sequence stars, but our result for  
262 W Aql shows that wide binaries with high eccentricities can survive to the AGB phase.  
263 Our hydrodynamic model, which takes into account the gravitational effect of the sec-  
264 ondary star on the wind and vice versa, exhibits a very slightly increasing orbital period  
265 (owing to the mass lost by the AGB star) but negligible changes in eccentricity, and  
266 does not show precession over  $\sim 5000$  years. While 5000 years may seem too short a  
267 time to make a definitive judgement, we point out that the expansion of the CSE dur-  
268 ing this time represents a larger spatial extent than the cool dust emission imaged by  
269 Herschel/PACS (at 70 and 160  $\mu\text{m}$  [20]). Despite the high eccentricity that we find for  
270 W Aql, none of our orbital solutions (Table A.3) have periastron separations smaller  
271 than the Roche limit, so no direct interaction between the two stars is expected and  
272 no evidence of such an interaction is seen in the ALMA observations. This suggests a  
273 relatively stable, if slowly evolving, system from which we could expect the eventual  
274 formation of a planetary nebula characterised by elongation to the southwest and per-  
275 haps a variety of additional arcs, analogous to what is presently seen in the AGB CSE,  
276 including at larger scales [19, 20, 22].

277 Other binary systems containing AGB stars have also been found to have long peri-  
278 ods (based mainly on spiral-like structures in CO observations) including AFGL 3068  
279 ( $\sim 800$  years [13]), R Scl (445 years [14, 32]), and II Lup (128 years [33]). In compari-  
280 son, AGB stars that have close companions, such as  $\pi^1$  Gru (current projected separation  
281 6 au [34, 11], period unknown) and V Hya (8.5 year period [35, 15]), both of which are  
282 triple systems that also have wide companions, have less spherical and more disrupted  
283 CSEs with, for example, bipolar outflows. Unlike the former group with more spherical  
284 CSEs, these triple systems are more likely to go on to form bipolar planetary nebulae.  
285 The very high eccentricity of W Aql precludes the presence of a stable third compan-  
286 ion and, despite the small periastron separation, we can consider it to be a relatively  
287 undisrupted system, suggesting the eventual formation of a relatively regular planetary  
288 nebula, i.e. perhaps more closely resembling the Ring Nebula than the Butterfly Nebula.

289 The study we have presented here adds to the small number of AGB stars with  
290 known companions and orbital parameters. While previous studies have struggled to  
291 explain the range of eccentricities observed for e.g. post-AGB stars, most of these have  
292 focussed on shorter orbital periods, ranging up to 1000 days, rather than 1000 years,  
293 owing to observational limitations [36]. The W Aql system provides further evidence  
294 that highly eccentric systems with long orbital periods exist during the AGB phase and  
295 that such eccentricity could be inherited by binary systems in later evolutionary phases,  
296 such as post-AGB stars and Barium stars [37]. The method used here — which entails  
297 the combination of chemical tracers and hydrodynamical models — can be used to de-  
298 tect the characteristic effects of main sequence binary companions in other AGB CSEs.  
299 Rather than solely searching for structures in the CSE, future studies can also check for  
300 anisotropies in molecular emission and the production of particular molecular species  
301 to confirm or rule out the presence of a stellar companion.

## 302 **3 Methods**

### 303 **3.1 Distance**

304 Many of the measurements and calculations in the present work rely on the value of the  
305 distance to the W Aql system and, more specifically, to the AGB component. Previ-  
306 ous modelling of W Aql has assumed a distance of 395 pc, calculated from a period-  
307 magnitude relation [21]. Prior to this, a variety of distances were assumed for W Aql,  
308 ranging from 230 to 680 pc [38, 39, 40, 41]. Recently, distances have been calculated  
309 based on high-precision parallax observations from the Gaia mission [42]. Values of  
310  $374 \pm 22$  pc [24] and  $380^{+68}_{-49}$  pc [43] were found using different methods based on the  
311 Gaia Early Data Release 3 [44]. In this work, we continue to use a distance of 395 pc  
312 because this value falls within the uncertainties of both Gaia-derived values, and be-  
313 cause it has been previously used in many radiative transfer models for the AGB star

314 [21, 22, 23, 24] and various stellar and circumstellar parameters such as luminosity  
315 and mass-loss rate have been derived relative to this value (Table A.2). We note that  
316 if the true distance is not exactly the adopted one, then the derivations of various pa-  
317 rameters would be altered in the following way: mass-loss rate and relative molecular  
318 abundances would tend to increase for a larger distance, although molecular abundances  
319 may not change significantly after the mass-loss rate was updated, owing to a degen-  
320 eracy between the impact of distance and density (the latter being directly related to  
321 mass-loss rate) on the line intensity. Our derived projected separations would increase  
322 linearly with distance, which would in turn result in a larger calculated orbital period.

## 323 3.2 Stellar masses

324 The companion to the AGB star was identified as a main sequence star classified as F8 to  
325 G0 [18], implying the stellar mass is in the range  $1.09 - 1.04 M_{\odot}$  [45]. For the purposes  
326 of this study we have assumed the companion is an F9 star with a mass of  $1.06 M_{\odot}$ .

327 The situation for the AGB component is more complicated. Previous studies com-  
328 paring oxygen isotopic ratios with stellar evolution models have calculated an initial  
329 stellar mass for the AGB star of  $1.6 \pm 0.2 M_{\odot}$  [46, 47]. Although the current mass-loss  
330 rate of the AGB star is relatively high at  $\dot{M} = 3 \times 10^{-6} M_{\odot} \text{ yr}^{-1}$  [22], stellar evolution  
331 models indicate that a significant decrease in stellar mass (i.e.  $> 0.1 M_{\odot}$ ) is not expected  
332 to occur until the final stages of the thermally pulsing AGB phase (i.e. during and after  
333 the last one or two thermal pulses [48]). Ergo, we assume  $1.6 M_{\odot}$  for the present AGB  
334 mass and hence assume a total system mass of  $2.66 M_{\odot}$ .

## 335 3.3 Spatially resolved imaging

336 W Aql was observed with the Advanced Camera for Surveys (ACS) on the Hubble  
337 Space Telescope (HST) at 400 nm on 12 October 2004 (Fig. 4b, [19]). It was observed  
338 again with VLT/SPHERE-ZIMPOL at 735.4 nm on 9 July 2019 (Fig. 4c, [28]). Both  
339 HST and SPHERE images were taken during a similar phase of the AGB pulsation, ap-  
340 proximately halfway between maximum and minimum light. Another HST observation  
341 was taken with the Wide Field/Planetary Camera (WFPC) at 550 nm in 1993 [20], but  
342 this was taken before the first servicing mission, and the degraded angular resolution  
343 makes it unusable for our study.

344 We measured the positions of the AGB and F9 stars using the python package  
345 `lmfit`<sup>1</sup>. We find the separation between the two stars is  $475 \pm 1.0$  mas in the HST epoch,  
346 and  $491 \pm 1.8$  mas in the SPHERE epoch. For HST, the astrometry is well characterised  
347 and the uncertainties were estimated based on the noise of the images. For SPHERE,  
348 the astrometric uncertainty includes the orientation with respect to north, the distortion,

---

<sup>1</sup><https://lmfit.github.io/lmfit-py/index.html>

349 the plate scale stability and the statistical position uncertainty [49] The change in pro-  
350 jected distance between the two stars is then calculated to be  $16 \pm 0.25 \pm 1.79$  mas (to  
351 distinguish between the systematic and statistical uncertainties) in 14.75 years, with the  
352 projected motion of the F9 star approximately following a straight line away from the  
353 AGB star. This motion does not contradict a highly inclined, nearly edge-on orbit, with  
354 inclination,  $i \sim 90^\circ$ . The 2019 SPHERE position corresponds to a projected separation  
355 of 194 au, at our adopted distance of 395 pc.

356 These results indicate that the orbital period must be long, particularly as compared  
357 with the timescale of our observations. For example, a circular orbit with a radius of  
358 194 au gives a period of 1660 years for our assumed system mass of  $2.66 M_\odot$ . An  
359 extremely elliptical orbit with an apastron of 194 au and a periastron of 3 au (a value  
360 chosen so the F9 star does not pass through the AGB star, since we see no evidence of  
361 such an extreme interaction) results in a period of 600 years. Note that neither of these  
362 orbits properly consider the motion seen between the HST and SPHERE epochs and are  
363 merely illustrative. The ephemeris of such a long orbit cannot be constrained through  
364 direct photometric imaging in a reasonable timeframe, because the observations would  
365 need to be taken decades and centuries apart. Hence, we require other markers in the  
366 circumstellar environment of the AGB star to constrain the orbital parameters of the  
367 W Aql system.

## 368 **3.4 ALMA results**

369 High spatial resolution observations of W Aql were obtained with the Atacama Large  
370 Millimetre/submillimetre Array (ALMA) as part of the ATOMIUM Large Programme<sup>2</sup>  
371 [50]. More than 110 molecular lines were detected towards W Aql, including CO, SiN,  
372 SiC, and HC<sub>3</sub>N, which are analysed here. We detected the SiC and NS radicals for  
373 the first time towards an S-type star. Previously, SiN was detected and HC<sub>3</sub>N was ten-  
374 tatively detected towards W Aql with the APEX telescope [47]. We present spatially  
375 resolved emission of SiN and HC<sub>3</sub>N for the first time. The SiN, SiC and HC<sub>3</sub>N emis-  
376 sion show two types of asymmetric morphologies, both different to the more extensive  
377 circumstellar structures revealed by the CO observations at high spatial resolution.

### 378 **3.4.1 Data reduction**

379 W Aql was observed with three array configurations of ALMA. This enabled us to  
380 observe small structures at high angular resolutions (down to  $0.024'' \times 0.021''$ ) while  
381 still retrieving larger structures (up to a maximum recoverable scale, or MRS, of  $8.9''$ )  
382 that would otherwise be resolved out [50]. While these are the extremes of resolution

---

<sup>2</sup>Programme ID: 2018.1.00659.L, PI L. Decin

383 and MRS available in the ATOMIUM dataset, the precise properties the data we analyse  
384 can be found in Table 1 for each transition.

385 We combined the three data sets to maximise the sensitivity of images, using the  
386 Common Astronomy Software Applications for Radio Astronomy (CASA [51]). We  
387 used the combined data to make spectral image cubes for each transition in Table  
388 1, weighting the contributions of the baselines to optimise the resolution and surface  
389 brightness sensitivity. The velocity resolution is  $1.1\text{--}1.3\text{ km s}^{-1}$  depending on frequency,  
390 and in some cases we averaged 2 or more channels to increase sensitivity. The typical  
391 rms noise is  $\lesssim 2\text{ mJy}$ . All velocities are adjusted to the LSR frame. The relative astro-  
392 metric accuracy of the extended configuration alone is  $\sim 0.002''$  and  $\sim 0.005''$  for the  
393 combined data at slightly lower resolution. The flux scale for the combined images is  
394 accurate to  $\sim 10\%$ . The chances of interferometric noise causing artefacts  $\geq 5\sigma$  in these  
395 images is negligible. The relative position accuracy of measurements is at least equal  
396 to the synthesised beam divided by the SNR [52], so for  $\text{SNR} = 5$  this is  $\sim 40\text{ mas}$  for  
397 SiN, SiC, NS, HC<sub>3</sub>N, and <sup>13</sup>CN, around  $25\text{ mas}$  for CO, and  $12\text{ mas}$  for SiO, SiS, CS  
398 and HCN.

399 Moment zero (integrated intensity) maps were made by summing all the channels  
400 with emission above  $\sim 3\sigma_{\text{rms}}$ . Position-velocity (PV) diagrams were made by selecting  
401 a tilted rectangular slice (‘slit’) covering the moment zero emission (spanning a width  
402 of  $3''$ ) at the angle shown in Fig. 1 (though other angles were tested, see Methods 3.4.3),  
403 and measuring the flux density in this region for each channel in increments along the  
404 slice. The peak of the continuum emission was assumed to be the position of the AGB  
405 star. In the channel maps and moment zero maps, the position of the AGB star is at  
406 (0,0). A small secondary peak, associated with the position of the F9 star, was detected  
407 in the continuum emission and will be analysed in a future paper.

408 To check whether our observations suffered from resolved-out flux, we compared  
409 spectra extracted from the ALMA data with previous observations of the same lines  
410 taken with the APEX single antenna [47] as shown in Fig. B.13. For CO we found 66%  
411 of the flux was resolved out, whereas all the flux was recovered by ALMA for SiN. We  
412 were unable to make the same comparison for SiC, which is a first detection, or HC<sub>3</sub>N,  
413 which was at best only tentatively detected with APEX [47]. Although only a third of  
414 the CO flux was recovered by ALMA, it is only smooth large-scale flux that is resolved  
415 out. This large scale flux is mostly associated with smoother bulk outflows, whereas  
416 our analysis in the present work focuses on smaller structures in the wind — i.e., the  
417 missing CO flux does not impede the present study.

418 Out of the other molecular lines discussed here and which have previously been ob-  
419 served, we found that about 28% of the flux in H<sup>12</sup>CN  $J = 3 \rightarrow 2$  was resolved out (Fig.  
420 B.17). Some degree of lost flux was expected because this line was not observed with  
421 the most compact configuration of ALMA. The corresponding transition in H<sup>13</sup>CN was  
422 not observed with APEX [47] but since it was observed with the compact configuration

Table 1: Molecular lines in the ground vibrational state used in our analysis.

Molecule	Transition	Frequency [GHz]	Ref. for freq.	$u_{\text{cent}}$ [km s <sup>-1</sup> ]	Ang. res. [ $''$ ]	MRS [ $''$ ]	Recovered flux
CO	$J = 2 \rightarrow 1$	230.538	[53]	...	$0.132 \times 0.123$	5.3	...
				-23.4	$0.829 \times 0.679$	8.9	33%
SiN	$N, J, F = 6, 13/2, 13/2 \rightarrow 5, 11/2, 11/2$	262.156 <sup>†</sup>	[26]	-23.7	$0.222 \times 0.198$	4.7	100%
SiC	$^3\Pi_2 J = 6 \rightarrow 5$	236.288	[54, 55]	-23.8	$0.199 \times 0.184$	2.6	...
NS	$^2\Pi_{1/2} f J, F = 11/2, 13/2 \rightarrow 9/2, 11/2$	253.968 <sup>‡</sup>	[56]	...	$0.187 \times 0.171$	2.5	...
HC <sub>3</sub> N	$J = 25 \rightarrow 24$	227.419	[57]	-22.5	$0.204 \times 0.181$	5.4	...
	$J = 26 \rightarrow 25$	236.513	[57]	-21.8	$0.208 \times 0.191$	2.6	...
	$J = 27 \rightarrow 26$	245.606	[57]	-21.4	$0.213 \times 0.172$	5.0	...
	$J = 28 \rightarrow 27$	254.700	[57]	-20.8	$0.190 \times 0.172$	2.5	...
SiO	$J = 5 \rightarrow 4$	217.105	[58]	-22.6	$0.063 \times 0.055$	5.7	85%
SiS	$J = 12 \rightarrow 11$	217.818	[59]	-21.4	$0.063 \times 0.055$	5.7	91%
CS	$J = 5 \rightarrow 4$	244.936	[60]	-22.5	$0.078 \times 0.066$	5.0	79%
HCN	$J = 3 \rightarrow 2$	265.886	[61]	-23.0	$0.061 \times 0.053$	2.4	72%
H <sup>13</sup> CN	$J = 3 \rightarrow 2$	259.012	[62]	-22.2	$0.073 \times 0.064$	4.8	...
<sup>13</sup> CN	$N, F_1, F_2, F = 2, 0, 2, 3, \rightarrow 1, 0, 1, 2$	217.303 <sup>‡</sup>	[63]	...	$0.213 \times 0.199$	5.7	44%
	$N, F_1, F_2, F = 2, 1, 3, 4, \rightarrow 1, 1, 2, 3$	217.467 <sup>‡</sup>	[63]	...			48%

**Notes:** All frequencies are rest frequencies and all velocities are with respect to the local standard of rest. (†) Frequency and corresponding quantum numbers of central hyperfine component are given. (‡) Frequency and corresponding quantum numbers of the brightest hyperfine component are given. Listed in column 4 are the primary references which provide the measured frequencies and the spectroscopic designation of the transitions observed here. The Cologne Database for Molecular Spectroscopy, CDMS [64, 65], provides a comprehensive list of the best estimate of the transition frequencies, the excitation energies, and the quantum mechanical line strengths. Column 5 gives the central velocity of the line as obtained from fitting a soft parabola (see Methods 3.4.1). Column 7 gives the maximum recoverable scale for the ALMA observations.

of ALMA and shows more extended emission than H<sup>12</sup>CN, we can assume very little, if any, flux was resolved out for H<sup>13</sup>CN. For SiO, SiS and CS, most of the flux was recovered, with only about 10–20% lost, as can be seen in Fig. B.17, where we have compared the spectra of these three molecules and H<sup>12</sup>CN observed with APEX and ALMA.

The <sup>13</sup>CN emission in  $N = 2 \rightarrow 1$  at 217 GHz has a low SNR. Therefore, to better determine the spatial distribution of <sup>13</sup>CN, we combined the two most intense components of the many possible fine and hyperfine structure transitions of the  $N = 2 \rightarrow 1$  transition that span a 450 MHz wide range centred on 217.257 GHz. We extracted the channels in the calibrated visibility data in the frequency ranges corresponding to  $v_{\text{LSR}} = -23 \pm 50$  km s<sup>-1</sup> around each of the rest frequencies and combined the channel selections aligned in velocity. The combined data set was assigned a fictitious rest frequency of 217.3055 GHz so that its central velocity corresponded to  $-23$  km s<sup>-1</sup>, and we then made an image cube from the stacked visibility data and analysed this following the same procedure as for the other data cubes. Finally, we checked the two multiplets



438 of  $^{13}\text{CN}$  listed in Table 1 individually for resolved-out flux and found that a little less  
 439 than half of the flux was recovered for these lines.

440 For all the spectral lines studied here, except for  $^{13}\text{CN}$  and NS, we fit soft parabola  
 441 profiles [66]

$$F(\nu) = F_0 \left( 1 - \left[ \frac{\nu - \nu_{\text{cent}}}{\nu_{\infty}} \right]^2 \right)^{\gamma/2} \quad (1)$$

442 where  $\nu_{\text{cent}}$  is the central velocity of the line profile and  $F_0$  is the flux at the centre of the  
 443 line. The parameters  $F_0$ ,  $\nu_{\text{cent}}$ ,  $\nu_{\infty}$ , and  $\gamma$  are left as free parameters in the fit. Primarily  
 444 this is done to obtain the central line velocities, which are included in Table 1. The  
 445 soft parabola profile was chosen over a Gaussian profile because the majority of the  
 446 lines studied here exhibit double-peaked emission and hence significantly deviate from  
 447 Gaussian line profile shapes.  $^{13}\text{CN}$  was excluded from this analysis because its hyperfine  
 448 structure dominates its line profile, and NS was excluded because the spectrum is too  
 449 noisy to obtain a reasonable fit. The central velocities of the lines were generally in  
 450 agreement with the previously measured stellar LSR velocity of  $\nu_{\text{LSR}} = -23 \text{ km s}^{-1}$   
 451 [21, 47] and will be discussed in more detail in the following sections.

### 452 3.4.2 AGB angular diameter

453 We took the calibrated data for all ALMA configurations combined, excluding channels  
 454 with line emission, and fit a uniform disc (UD) to the visibilities (as in [67]). This  
 455 gave a diameter of 16.6 mas, containing 8.0 mJy. There was negligible ellipticity or  
 456 displacement of the centroid. At mm wavelengths, a UD is expected to be a better  
 457 representation of stellar brightness distribution than a Gaussian distribution. The SNR  
 458 is  $> 100$ , suggesting sub-mas precision, based on the nominal uncertainty of beam size  
 459 divided by SNR, but taking into account possible irregularities in the stellar disc, we  
 460 adopt a conservative uncertainty of 3 mas. The diameter of  $16.6 \pm 3 \text{ mas}$  is the size  
 461 of the the surface where electron-neutral free-free emission dominates and is optically  
 462 thick (at these wavelengths [68]) and corresponds to a radius of  $3.3 \pm 0.6 \text{ au}$  at our  
 463 adopted distance. We note that the resolution of the continuum image from the extended  
 464 array is  $21 \times 24 \text{ mas}$  [50], while for the combined continuum image it is  $40 \times 33 \text{ mas}$ .  
 465 The optical diameter is  $11.6 \pm 1.8 \text{ mas}$  [25], 34% smaller than our value. Vlemmings  
 466 et al. [68] found that the mm-wave diameters of a small sample of AGB stars were  
 467 15–50% greater than the optical diameters, consistent with our finding. It has also been  
 468 found that, in general, the mm-wave diameters of the ATOMIUM sample are 30–100%  
 469 larger than the optical diameters [69].

### 470 3.4.3 SiN and SiC

471 The SiN line we observe towards W Aql ( $N, J = 6, 13/2 \rightarrow 5, 11/2$ ) is a blend of three  
 472 closely-spaced hyperfine components separated by about 0.8 and 0.5 MHz (Fig. B.13),

473 and the frequency of the centroid is 262,155.78 MHz. The lower spin-rotation compo-  
 474 nent ( $N, J = 6, 11/2 \rightarrow 5, 9/2$ ) at 262.650 GHz falls just outside of the frequency range  
 475 covered by our observations. The SiC line detected towards W Aql corresponds to the  
 476  $J = 6 \rightarrow 5$  transition in the lowest fine structure ladder  $^3\Pi_2$  [54]. The corresponding  
 477  $J = 6 \rightarrow 5$  rotational transitions in the  $^3\Pi_1$  and  $^3\Pi_0$  upper fine structure ladders fell  
 478 between the frequency bands covered by our observations.

479 Neither SiN nor SiC were detected for any other stars in the ATOMIUM sample,  
 480 all of which are oxygen-rich aside from one other S-type AGB star ( $\pi^1$  Gru). SiC has  
 481 been previously detected towards 12 carbon-rich AGB stars [70], but the present work  
 482 represents the first detection of SiC in the envelope of an S-type AGB star. SiN has been  
 483 previously detected towards W Aql [47] and only one other star: the nearby carbon-rich  
 484 AGB star CW Leo [26], which is suspected of having a companion [71, 72, 73]. Spa-  
 485 tially resolved Submillimeter Array (SMA) observations towards CW Leo show the SiN  
 486 mainly distributed in a shell-like pattern, with some brighter, asymmetric, emission to  
 487 the south-west [74]. However, a detailed analysis of these observations has not yet been  
 488 published and, consequently, we lack detailed spatial information for SiN around other  
 489 stars with which to compare our W Aql results. Spatially resolved SiC emission has  
 490 also been observed towards CW Leo, for which SiC was not detected in the innermost  
 491 regions of the CSE but rather in outer shells [75], possibly also showing some asymme-  
 492 try to the south-west [74]. Further discussion of SiC distributions is given in Methods  
 493 3.6.1).

494 The integrated intensity maps of SiN (Fig. 1a) and SiC (Fig. A.5a) show emission  
 495 primarily north and east of the AGB star. The SiN emission has a higher SNR and is  
 496 hence more readily analysed. Therefore, we have focussed our analysis on SiN, but note  
 497 that the SiC observations agree with the conclusions drawn from SiN.

498 We produced a series of position-velocity diagrams of SiN using a wide slit (total  
 499 width  $3''$ ) to encompass all the emission seen in the zeroth moment map (Fig. 1a).  
 500 Using a narrower slit (such as  $0.3''$ ) resulted in a lower SNR in the PV diagram, making  
 501 an analysis more troublesome. We tested all possible slit angles passing through the  
 502 position of the AGB star in increments of  $5^\circ$  and then  $1^\circ$  around the angles producing  
 503 the most distinct PV diagrams. The final slit position of  $33^\circ$  east of north was chosen on  
 504 the basis of the clarity and intensity of the associated PV diagram. Even though the slit  
 505 angle was determined independently, we find that it passes through the present position  
 506 of the F9 star (Fig. 1a). As shown in Fig. 1b, the PV diagram of SiN exhibits an arc-like  
 507 structure in position-velocity space, tracing a little more than half an ellipse centred on  
 508 the AGB star. We fit a parabola to the points in the PV diagram with intensities  $\geq 3\sigma$   
 509 above the noise, weighted by the flux at those points. The peak of the parabola, plotted  
 510 in white in Fig. 1b, is at  $-24.1 \text{ km s}^{-1}$ , which is in agreement with the central velocity  
 511 we find for the spectral line (Table 1). The emission distribution in the PV diagram  
 512 does not precisely follow the shape of the parabola, particularly at the negative offset

513 and extreme velocity edges of the emission, so we also plot a partial ellipse based on  
 514 the position of the parabola (using the centre and peak of the parabola and with the  
 515 half-width along the velocity axis set to  $14 \text{ km s}^{-1}$ ), which better follows the shape of  
 516 the emission at the most extreme velocities. We followed a similar procedure for SiC  
 517 to produce a PV-diagram and fit a parabola to the arc of emission (Fig. A.5b). For SiC,  
 518 the peak of the parabola is at  $-23.5 \text{ km s}^{-1}$ . We similarly plot a partial ellipse based on  
 519 the parabola fit (velocity half-width  $13 \text{ km s}^{-1}$ ), which also follows the emission at the  
 520 most extreme velocities more closely.

521 In concert, the zeroth moment map and the PV diagram show that the SiN emission  
 522 forms an arc to one side of the system, which is close to edge-on or perpendicular to  
 523 the plane of the sky. We also plot the summed blue and red channels of SiN separately  
 524 in Fig. B.14. Owing to the noisy edges of the contours, we could not conclusively  
 525 determine whether there is an offset between them along the axis connecting the present  
 526 positions of the AGB and F9 stars. Consequently, we take the orbital inclination of the  
 527 system to be  $i = 90 \pm 7^\circ$ , where the uncertainty is derived from the beam size. The  
 528 lack of spherical symmetry in the SiN emission suggests a spatial dependence for the  
 529 formation of SiN, as discussed in Methods 3.6 and depicted in Fig. A.10. Despite the  
 530 lower SNR of the SiC emission, the similar structure seen in the PV-diagram for SiC  
 531 indicates a similar formation history for both SiN and SiC.

#### 532 3.4.4 NS

533 Two rotational transitions of NS were covered by the ATOMIUM observations — the  
 534  $J = 11/2 \rightarrow 9/2$  hyperfine split multiplets in the  $^2\Pi_{1/2}$  and  $^2\Pi_{3/2}$  spin-orbit fine structure  
 535 components. Neither rotational transition was detected in spectra centred on the AGB  
 536 star. However guided by predictions from chemical models (Methods 3.6.2 and [4]),  
 537 we conducted a more careful search for NS. The transition in the ground  $^2\Pi_{1/2}$  compo-  
 538 nent lies very close to the edge of our frequency band and is difficult to discern in the  
 539 spectra, but we successfully detected it in the zeroth moment map (Fig. B.15a), which  
 540 constitutes the first detection of NS towards an S-type AGB star. The corresponding  
 541 rotational transition in the upper ( $^2\Pi_{3/2}$ ) spin-orbit component at  $255.597 \text{ GHz}$  [56] lies  
 542 about  $322 \text{ K}$  above the ground state and is estimated to be about three times less intense.  
 543 We found an upper limit for the  $^2\Pi_{3/2}$  component of  $3\sigma = 0.047 \text{ Jy beam}^{-1} \text{ km s}^{-1}$  in a  
 544 zeroth moment map that covers the same velocity extent as that observed for the ground  
 545  $^2\Pi_{1/2}$  component.

546 Prior to this, NS had been detected towards just one AGB star, the oxygen-rich  
 547 IK Tau [76, 77] (and notably has not been detected towards the nearby carbon star  
 548 CW Leo). An enhanced abundance of NS is expected to be a good tracer of binarity  
 549 for S-type or oxygen-rich AGB stars with main sequence or white dwarf companions  
 550 [4]. We checked the ATOMIUM data for NS detections towards other sources. While  
 551 we could rule out NS detections in several sources, for a selection of others (the AGB

stars IRC +10011 and IRC –10529, and the red supergiants VX Sgr and AH Sco) we could not conclusively confirm or rule out the presence of NS for three reasons. First, the  $^2\Pi_{1/2}$  component at 253.968 GHz lies close to the edge of an observed band in frequency space, meaning that the line may be partially truncated, as it is for W Aql. Second, that line lies close to the SO<sub>2</sub> ( $J_{K_a,K_c} = 15_{6,10} \rightarrow 16_{5,11}$ ) line at 253.957 GHz and, for the oxygen-rich sources mentioned above, we cannot easily disentangle which emission comes from SO<sub>2</sub> and which might come from NS. (This is not a problem for W Aql, towards which no SO<sub>2</sub> lines are detected, including more intrinsically intense lines covered by our observations.) Disentangling NS and SO<sub>2</sub> emission is made more difficult because both lines are truncated by the edge of the observed band. Finally, we also checked for emission from the  $^2\Pi_{3/2}$  component at 255.597 GHz but could not confirm the detection of this line of NS. For the AGB stars mentioned above, we did not detect emission above the noise of our observations. However, if we take the expected intensity of the  $^2\Pi_{3/2}$  component to be a third that of the truncated and possibly blended line around 253.968 GHz, we determine that the expected intensity is below the noise of our observations. For the two red supergiants, the potential NS line is blended with a high-energy SO<sub>2</sub> line, ( $J_{K_a,K_c} = 51_{7,45} \rightarrow 50_{8,42}$ ) at 255.595 GHz. Therefore, to determine whether NS is present in these or other ATOMIUM stars, observations of other NS transitions that do not overlap with SO<sub>2</sub> or other molecular lines are required.

In addition to the zeroth moment map, we also constructed a PV diagram of NS (Fig. B.15b). The only significant region of emission that is  $3\sigma$  above the noise in the PV diagram is located on the red side of the PV diagram and not notably offset from the position of the AGB star. This is close to some of the most intense regions seen in the SiN and SiC PV diagrams. We note that because the NS line is on the edge of the observed band, some redder emission might not have been recovered by our observations. To emphasise that this is a true detection of NS rather than a misidentified line, we plot the spectrum of the NS line with the spectra of the SiN and SiC lines in Fig. B.15c. All lines were extracted from circular apertures with radii  $0.25''$ , centred on the continuum peak, which was chosen to best show the NS line. All three lines have a double-peaked profile, with SiN and NS having a brighter red peak than blue peak. Although the NS spectrum is truncated at  $-9 \text{ km s}^{-1}$ , it can be seen rising in a profile similar to the SiN and SiC red peaks. Deeper observations targeting NS would confirm this behaviour.

### 3.4.5 HC<sub>3</sub>N

Four successive rotational lines of HC<sub>3</sub>N were detected towards W Aql as part of the ATOMIUM project (Table 1). Prior to this, the three lowest transitions in this group were tentatively detected towards W Aql with APEX [47]. A comparison of the lines tentatively detected with APEX and our ALMA data suggests that the ALMA data does not suffer from resolved-out flux. It should also be noted that the  $J = 25 \rightarrow 24$  and

591  $J = 27 \rightarrow 26$  lines were observed with all three ALMA configurations (including  
 592 the compact configuration), while the  $J = 26 \rightarrow 25$  and  $J = 28 \rightarrow 27$  lines were  
 593 observed with only the extended and medium configurations. All four lines have similar  
 594 intensities when the spectra are extracted from our combined data cubes, as expected  
 595 for lines with similar energies (the lower level energies span 131–165 K) and Einstein  $A$   
 596 coefficients. Taken together, our observations confirm that there is no flux resolved out  
 597 for the observations with the medium configuration. Most of the  $\text{HC}_3\text{N}$  flux is located  
 598 south and west of the present location of the AGB star (Figs. 2 and B.16), in direct  
 599 contrast with the observed flux of SiN and SiC (Figs. 1 and A.5).

### 600 3.4.6 CO

601 The CO  $J = 2 \rightarrow 1$  line has the most extended emission distribution of all the spectral  
 602 lines observed towards W Aql as part of the ATOMIUM Programme. Although only  
 603 one third of the flux was recovered by ALMA (Methods 3.4.1), our analysis focuses on  
 604 smaller structures in the wind, which are not affected by resolved-out flux.

605 Many complex structures are seen in the CO emission, making a definitive analysis  
 606 difficult. We first examined the inner wind region, where an overdensity thought to be  
 607 (part of) a spiral arm was reported [23]. In this region, we found an approximately  
 608 circular structure that corresponds very well to the location of the overdensity and to the  
 609 radius of the observed SiN emission. In Fig. 3b, we plot the CO emission close to the  
 610 AGB star using a logarithmic colour scale and overplot the contours of SiN (as seen in  
 611 Fig. 1a) and a black circle to guide the eye to the roughly circular structure. The radius  
 612 of this circle is  $1.35''$  and its centre is  $0.1''$  to the north of the AGB star.

613 Additional circular structures in the CO emission were more difficult to concretely  
 614 identify, so we plotted the radial intensity against anticlockwise angle to help find such  
 615 structures (Fig. A.8). Circular structures centred on the AGB star would appear as  
 616 horizontal lines in such a plot, whereas off-centre circular structures appear as sinusoids.  
 617 Using the angle-radius plot, we found off-centre circles corresponding to: (red) the edge  
 618 of the bright central region with a radius of  $4''$ , (pink) a circular structure surrounding  
 619 this region, with a radius of  $5.5''$ , and (white) another circle with radius  $10.75''$  which  
 620 falls close to the edge of the ALMA field of view. The white circle is offset in the  
 621 same direction (north) as the black circle. Note that the sinusoid corresponding to the  
 622 black circle identified above can be seen more clearly in the angle-radius plot when it  
 623 is zoomed in on the structures closer to the AGB star (bottom panel of Fig. A.8). [In](#)  
 624 [Fig. B.25](#) we show the same angle-radius plots as in Fig. A.8, but exclude the coloured  
 625 lines highlighting the aforementioned structures.

626 We plot all these circular structures in Fig. 3a over the averaged central three chan-  
 627 nels of the CO emission. From our analysis with the hydrodynamic model (Methods  
 628 3.7) we come to the conclusion that the black and white circles were formed during the  
 629 periastron passage of the two stars, in which case they are expected to be offset to the

630 opposite side of the AGB star from the F9 star. The periastron origin of the black circle  
631 is also supported by its co-location with the SiN arc. The red and pink circles, and other  
632 irregular structures, are not directly reproduced by the hydrodynamic model, but this is  
633 likely because of limitations in the model including missing physics around pulsations  
634 and the wind launching mechanism (see discussion in Methods 3.7). Significantly, the  
635 wind is launched at  $13 \text{ km s}^{-1}$  in the hydrodynamic model, whereas previous studies  
636 assume a much lower initial velocity of  $3 \text{ km s}^{-1}$ , close to the sound speed. This dis-  
637 crepancy prevents a dense inner region forming in the hydrodynamic model, such as the  
638 region encircled in red in Fig. 3a. We also note that the formation timescales of the red  
639 and pink circles and other neighbouring features are  $\lesssim 300$  years (taking  $\beta$ -law wind  
640 acceleration into account) and do not match the longer timescale of the binary orbit  
641 inferred from resolved imaging (Methods 3.3).

642 When comparing these circular structures with the lower-resolution ( $0.47 \times 0.41$ )  
643 ALMA observations of CO ( $3 \rightarrow 2$ ) around W Aql [22], in which several circular arcs  
644 were identified, we find that our red, pink and white circles correspond to the locations  
645 of those arcs. In particular, the outermost arc in the earlier data corresponds well with  
646 our white circle, and the innermost two arcs (north and south-west) match the position of  
647 our red circle. The circular region of higher flux that we have indicated in red in Fig. 3a  
648 for CO ( $2 \rightarrow 1$ ) also corresponds to the region of higher flux seen in CO ( $3 \rightarrow 2$ ). The  
649 remaining arcs identified by [22] match our pink circle and a few other structures seen  
650 in our data which do not form full circles. Note that our black circle is too small to be  
651 well resolved in the earlier data.

652 The shell-like structures seen around W Aql have some similarity to previously re-  
653 ported shells around the carbon star CW Leo, which are also not perfectly centred on  
654 the AGB star [71, 78, 79]. Many more shells are seen for CW Leo than W Aql, likely  
655 in part because CW Leo is closer, making emission easier to detect. Studies of the  
656 CW Leo shells have concluded that they could be caused by an eccentric binary orbit  
657 seen perpendicular to the line of sight, and assumed some periods of enhanced mass  
658 loss [71, 79]. Our hydrodynamic models do not assume a variable mass-loss rate (see  
659 Methods 3.7) but still form shell-like structures when viewed perpendicular to the or-  
660 bital plane. This does not mean that the mass-loss rate of W Aql cannot be variable —  
661 indeed variable or anisotropic mass-loss might account for some of the other structures  
662 seen in the CO emission. [The possible effects of variable and anisotropic mass loss are  
663 discussed in more detail in the Supplementary Materials B.2.](#)

664 We also analysed the higher and lower velocity channels of the W Aql CO emission,  
665 particularly in comparison to the hydrodynamic model. A long-standing unexplained  
666 phenomenon is excess emission in the blue wings of the line profiles of CO and other  
667 molecules towards W Aql [21]. In our ALMA observations of CO (Fig. A.7), it is  
668 clear that the blue- and red-shifted channel maps are not symmetric around the LSR  
669 velocity. The blue channels ( $-37$  to  $-30 \text{ km s}^{-1}$ ) show slightly asymmetric emission,

670 with an elongation in the south-west direction, while the red channels ( $-14$  to  $-8$  km s $^{-1}$ )  
671 show emission with more circular symmetry. These differences in shape account for the  
672 excess emission in the blue wing of the line profiles. We also compared these different  
673 emission distributions with the equivalent distributions produced by the hydrodynamic  
674 model after processing by the radiative transfer code MCFOST (Methods 3.7). In Fig.  
675 A.12 we plot two CO channels equidistant from the LSR velocity and the equivalent  
676 model channels. The model also shows the elongated CO emission for the blue channel  
677 and the more circular emission for the red channel, reinforcing that the asymmetry arises  
678 from the companion's interactions with the AGB wind.

### 679 3.4.7 Other molecular species

680 The species SiO, SiS, HCN, and CS are commonly observed in the envelopes of many  
681 AGB stars of all chemical types [38, 80, 81, 82]. All four molecules were observed  
682 previously towards W Aql at a lower spatial resolution of  $0.55'' \times 0.48''$  [23] and were  
683 analysed using radiative transfer models under the assumption of spherical symmetry.  
684 Our new observations were obtained at a much higher angular resolution and the emit-  
685 ting regions for all four molecules are very well resolved (Table 1 and Fig. A.6). The  
686 increased angular resolution allows us to observe asymmetries in the emission. The  
687 emission from all four molecules is more extended to the north-east than to the south-  
688 west. This is a qualitatively similar anisotropy to that seen in SiN, but unlike SiN, the  
689 more common species exhibit roughly spherically symmetric emission across a much  
690 wider fan-like region, running clockwise from east to north west (Fig. A.6). In the con-  
691 text of an eccentric binary companion, we interpret this not as enhanced production of  
692 SiO, SiS, HCN, and CS triggered during the periastron passage (as we conclude in the  
693 cases of SiN and SiC), but as enhanced destruction through photodissociation of SiO,  
694 SiS, HCN, and CS by the F9 companion, during the large portion of the orbital period  
695 it spends to the southwest of the AGB star. If this were not the case, we should see  
696 significantly less emission to the northwest and southeast (i.e. the other regions where  
697 we do not see SiN), but the contours in Fig. A.6 have similar extents from the southeast  
698 to northeast to northwest. This is especially apparent in plots of the central channels of  
699 SiS and CS, shown in Fig. B.18, which show significantly reduced emission near the  
700 F9 star as opposed to on the opposite side of the AGB star. For CS, the  $3\sigma$  contour  
701 centred on the AGB stars extends out to  $0.33''$  ( $\sim 2 \times 10^{15}$  cm) from the AGB star in the  
702 direction of the F9 star, compared with  $0.71''$  ( $\sim 4 \times 10^{15}$  cm) in the opposite direction.  
703 For SiS, the  $3\sigma$  contour centred on the AGB star extends out to  $0.09''$  ( $\sim 5 \times 10^{14}$  cm)  
704 in the direction of the F9 star and out to  $0.23''$  ( $\sim 1 \times 10^{15}$  cm) in the opposite direction.

705 Furthermore, the PV diagrams of CS, SiO and H $^{13}$ CN, taken along the same axis as  
706 we used for SiN and plotted in Fig. B.19, show the brightest emission spatially close  
707 to the AGB star, not in an arc as for SiN or SiC. They also show that the emission is  
708 consistently less extended and less intense on the side of the AGB star where the F9 star

709 is located. Notably, this is not the case for CO, also plotted in Fig. B.19, which does not  
710 show evidence of photodissociation by the F9 star, as expected given its stronger bond  
711 energy and self-shielding [83]. The reduced emission seen in the spectra around the F9  
712 star (Methods 3.4.8) is further evidence of most molecules being destroyed by the F9  
713 flux.

714 Another molecular species that displays highly asymmetric emission around W Aql  
715 is  $^{13}\text{CN}$ . Although the main isotopic species,  $^{12}\text{CN}$ , was not covered in the ATOMIUM  
716 observations, it has previously been observed towards W Aql with the IRAM 30m tele-  
717 scope [84]. We find that, unlike the common molecular species discussed above, the  
718  $^{13}\text{CN}$  emission is mainly seen on the opposite side of the AGB star. As can be seen from  
719 the zeroth moment maps of  $\text{H}^{13}\text{CN}$  and  $^{13}\text{CN}$  in Fig. 2, the  $^{13}\text{CN}$  emission is mainly  
720 observed where the  $\text{H}^{13}\text{CN}$  emission is absent, which is consistent with the generally  
721 accepted notion that CN is a photodissociation product of HCN [27]. This is discussed  
722 in more detail in Methods 3.6.

### 723 3.4.8 Molecular emission around F9 star

724 We extracted spectra in circular apertures of radii 100 mas (corresponding to a projected  
725 radius of 40 au) centred on the F9 star to check for anomalous emission. Very few lines  
726 were detected above the noise in these spectra, with lines originating only from CO,  
727 SiO, CS, and HCN. We compared the line profiles extracted from the region around  
728 the line-of-sight position of the F9 star with profiles of the same sized aperture centred  
729 on the AGB star and plot comparisons for CS, HCN and SiO in Fig. A.9. Notably,  
730 the F9-centred line profiles exhibit relatively more flux in the blue channels and less  
731 flux in the red channels than the corresponding AGB-centred profiles. The F9-centred  
732 profiles also tend to have relatively less emission in the channels close to the LSR ve-  
733 locity. From this, we can estimate that the F9 star is located, spatially, in the region  
734 that corresponds to gas with velocities close to the AGB stellar LSR velocity, i.e. gas  
735 with motions approximately in the plane of the sky. This estimate is possible because,  
736 in an expanding circumstellar envelope, the velocity axis has a correspondence to the  
737 line of sight spatial axis (see, for example, [79]). Although this does not say anything  
738 about the present velocity of the F9 star (it need not be moving at the same velocity  
739 as the AGB circumstellar gas that it is moving through), it is consistent with the stars  
740 being in a highly eccentric orbit, as the present relative motion of the F9 star would be  
741 predominantly in the plane of the sky rather than into or out of the plane of the sky, and  
742 would, in any case, have a low absolute total velocity of  $\sim 2 \text{ km s}^{-1}$ .

743 We also checked the shape of the line profiles extracted for an equivalent 100 mas  
744 aperture on the opposite side of the AGB star from the F9 star (at the same projected  
745 separation) and found that those line profiles were more similar to the AGB-centred  
746 line profiles than those centred on the F9 star (Fig. A.9). Finally, we note that the  
747 phenomenon of the blue peaks being brighter than the red peaks for the F9-centred



748 profiles is the opposite of what we see for the line profiles of SiN and NS (Fig. B.15c)  
 749 centred on the AGB star. This is easily explained by the different formation/destruction  
 750 times of the two groups of molecules: SiN and NS formed during the periastron passage,  
 751 whereas CS, HCN and SiO are presently being (partly) photodissociated by the UV flux  
 752 of the F9 star.

753 The intensity of the UV flux from the F9 star is proportional to the inverse square of  
 754 the distance from the star. This means that the apparent UV flux close to the AGB star,  
 755 taking the projected separation of 194 au, is 24 times less than the flux 40 au from the  
 756 F9 star, and the flux on the opposite side of the AGB star (at a distance of 388 au) is 94  
 757 times weaker. At a distance of 10 au from the F9 star, close to the distance between the  
 758 two stars during periastron, the UV flux would be 380 times higher than the flux on the  
 759 same region at the present stellar separation. Note that these values are rough estimates  
 760 and do not include, for example, UV extinction by dust, which would further reduce the  
 761 UV flux for larger distances when there is more dust between the F9 star and the region  
 762 of interest.

### 763 3.5 Radiative transfer modelling

764 Radiative transfer calculations were undertaken to approximate the abundance of SiN  
 765 in the arc seen in Fig. 1. To achieve this, we extracted the SiN spectra from round  
 766 apertures with radii of 0.25'', evenly spaced with centres separated by 0.3'' starting from  
 767 the continuum peak and moving outwards along the north 33° east line passing through  
 768 the emission. The set-up is shown in Fig. A.11a, where the regions are labelled from A  
 769 to H. The aperture size was chosen so as to not lie outside of the detected SiN emission.  
 770 Furthermore, these regions are centred along the same axis for which we found the best  
 771 PV diagram (Fig. 1b and Methods 3.4), so they are unlikely to overlap with the edges  
 772 of the SiN emission. Therefore, by considering only spectra from the regions plotted  
 773 in Fig. A.11c, we can use a 1D (spherically symmetric) radiative transfer model to  
 774 compare equivalent synthetic spectra and determine the SiN abundance distribution in  
 775 the arc, which can also be approximated by a wedge of a spherical shell. Our approach  
 776 is viable because the SiN emission is expected to be optically thin (and indeed we find  
 777 a peak tangential optical depth of  $\tau \lesssim 0.2$  in the model) and emission in other parts of  
 778 the spherically symmetric model (at different velocities) is not expected to interact with  
 779 emission in the regions of interest.

780 We used the accelerated lambda iteration method (ALI [85]), which has been previ-  
 781 ously used to determine the abundances of various other molecules in the CSE of W Aql  
 782 [23, 24]. We use previously determined circumstellar parameters for W Aql [21], in-  
 783 cluding a radial temperature profile, the mass-loss rate of  $3 \times 10^{-6} M_{\odot} \text{ yr}^{-1}$  [22] and a  
 784 velocity profile described by [21]

$$v(r) = v_0 + (v_{\infty} - v_0) \left(1 - \frac{R_{\text{in}}}{r}\right)^{\beta} \quad (2)$$

785 with  $v_0 = 3 \text{ km s}^{-1}$  the velocity at the dust condensation radius,  $R_{\text{in}} = 2 \times 10^{14} \text{ cm}$ ,  
786  $v_\infty = 16.5 \text{ km s}^{-1}$  the terminal expansion velocity and  $\beta = 2$ . The key stellar and  
787 circumstellar parameters are summarised in Table A.2. We also included a previously  
788 implemented overdensity [23], which was found to improve the radiative transfer model  
789 fit for ALMA observations of CS and  $\text{H}^{13}\text{CN}$  at lower resolutions [23]. The overdensity  
790 relates to an increase in the  $\text{H}_2$  number density by a factor of five between the radii of  
791  $8 \times 10^{15} \text{ cm}$  and  $1.5 \times 10^{16} \text{ cm}$  (Fig. A.11), and is in good agreement with the location of  
792 a region of increased CO emission (a good tracer of density) traced by the black circle  
793 in Fig. 3b. (Previously the overdensity was thought to be part of an unresolved spiral  
794 arm [23].)

795 We include SiN energy levels up to  $N = 20$  in the ground vibrational state and  
796 the 59 radiative transitions connecting those levels. The energy levels and Einstein A  
797 coefficients were calculated using CALPGM [86] and take fine structure into account but  
798 neglect the closely spaced hyperfine structure, which is not resolved in our observations.  
799 There are no calculated or measured collisional (de)excitation rates for SiN, so instead  
800 we use the rates calculated for CN-He [87], scaled by 1.37 to account for the different  
801 reduced mass of the SiN- $\text{H}_2$  system.

802 On the basis that the different extraction apertures shown in Fig A.11a probe differ-  
803 ent regions of the SiN distribution, we tried various shapes for the radial distribution of  
804 SiN abundance in an attempt to reproduce the observed distribution of SiN. These in-  
805 cluded a constant abundance, step functions of different constant SiN abundances, and  
806 Gaussian shells of various widths and positions. We also left the inner and outer radii  
807 of the SiN emitting region as free parameters. We found that while the two apertures  
808 farthest from the continuum peak, G and H, were sensitive to the outer radius and outer  
809 abundance of the SiN distribution, as expected, the inner apertures, A to D, were also  
810 sensitive to these properties, which affected the heights of the emission peaks in their  
811 double-peaked profiles. Conversely, the choice of inner radius and the innermost abun-  
812 dance of SiN mainly affected the heights of the line centres for apertures A to C. These  
813 dependencies were expected given the observed wedge of SiN emission.

814 Our best-fitting model has a constant outer SiN abundance relative to  $\text{H}_2$  of  $1.5 \times$   
815  $10^{-7}$ , from  $6 \times 10^{15} \text{ cm}$  to  $2 \times 10^{16} \text{ cm}$ , and a power-law distribution in the inner part,  
816 starting from an inner radius of  $1.5 \times 10^{15} \text{ cm}$ . This distribution is plotted in Fig. A.11b,  
817 where we also show the  $\text{H}_2$  number density over the same region, including the afore-  
818 mentioned overdensity. As can be seen from Fig. A.11b, the extended peak of the SiN  
819 abundance spans the region of the  $\text{H}_2$  overdensity. This further supports the idea that  
820 both phenomena have a common cause, which we postulate is the periastron passage of  
821 the AGB and F9 stars. The line profiles generated by the best fitting models are plotted  
822 with the spectra in Fig. A.11c.

## 3.6 Chemical modelling

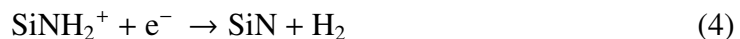
The recent results of Van de Sande and Millar [4] focus on the effect of close companions on the circumstellar chemistry. In Fig. B.20 we reproduce their results for stars with similar wind density to W Aql [Model:  $\dot{M}/v_\infty = 2 \times 10^{-6} M_\odot \text{ yr}^{-1}/(\text{km s}^{-1})$  compared with W Aql:  $\dot{M}/v_\infty = 1.8 \times 10^{-6} M_\odot \text{ yr}^{-1}/(\text{km s}^{-1})$ ], showing the predicted abundances of SiN, SiC and NS for both oxygen- and carbon-rich outflows, with and without an F9-like companion. The companion is approximated by a black body at 6000 K and does not explicitly include chromospheric UV photons. However, observations of W Aql with GALEX in 2006 reveal a detection in the near UV (22.16 mag, 1771–2831 Å) but not in the far UV ( $> 22.5$  mag, 1344–1786 Å) [88], the latter being more important for breaking molecular bonds. If additional chromospheric UV flux is generated around periastron, as has been suggested for other types of stars in close binary systems [89, 90], then this would mainly serve to increase the products of UV photochemistry, such as  $\text{Si}^+$ , which are discussed below. An excessively large UV excess during periastron could possibly destroy a larger variety of molecular species than predicted, but this would occur over a relatively short timescale (see Table A.3 and Methods 3.9) and would not preclude further chemical interactions, including many of the formation channels discussed below, once the stars moved further apart.

### 3.6.1 SiN and SiC

The chemical models [4] show that, in the absence of a companion, the SiN radical is expected to form in a shell-like distribution, with a peak abundance at a radius of around  $10^{16}$  cm from the AGB star (Fig. B.20). The main formation pathway of SiN is via the measured reaction



where  $\text{NH}_3$  is assumed to be a parent species that is formed close to the AGB star and, through observations, has been found to have a peak abundance of  $\sim 2 \times 10^{-5}$  relative to  $\text{H}_2$  [21]. This is followed by dissociative recombination



The main source of  $\text{Si}^+$  is the photodissociation of SiS, i.e.



which occurs very readily in the presence of the F9 companion (see Fig. B.21) and the UV photons it emits [4]; and is confirmed in our observations (Fig. A.6), because SiS is noticeably depleted to the southwest at the present position of the F9 star. We also note that there are minor formation pathways for SiN forming from HNSi and SiC, but

854 both pathways also depend on  $\text{NH}_3$  and  $\text{Si}^+$  and hence are also affected by UV photons  
855 driving the formation of  $\text{Si}^+$ .

856 In the chemical models ([4] and Fig. B.20), the main difference in the SiN abundance  
857 distributions between oxygen- and carbon-rich stars with the same wind density and no  
858 companion, is that the peak relative abundance of SiN is predicted to be  $\sim 10^{-8}$  for the  
859 oxygen-rich star and  $\sim 10^{-7}$  for the carbon-rich star. W Aql is an S-type star whose  
860 chemistry is presumed to be intermediate between the typical carbon-rich and oxygen-  
861 rich stars [21], and that is what has been found for the abundances of HCN in S-type  
862 stars [80]. However we find that the peak abundance of SiN in W Aql ( $1.5 \times 10^{-7}$   
863 relative to  $\text{H}_2$ , see Methods 3.5) is in good agreement with that predicted for a carbon-  
864 rich star, although the asymmetric distribution of SiN implies that the formation process  
865 is anisotropic.

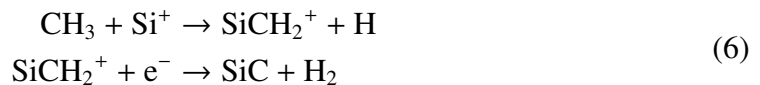
866 Van de Sande and Millar's study [4] focused on the impact of UV photons from  
867 stellar companions on the circumstellar chemistry of AGB stars. They include a set of  
868 models with a main sequence companion with a stellar effective temperature of 6000 K  
869 that is comparable to the temperature of an F9 dwarf [91] (reproduced in Fig. B.20).  
870 The radial abundance profile of SiN is significantly altered by the companion — i.e.,  
871 the peak abundance of SiN in both the carbon- and oxygen-rich winds is higher, and  
872 the abundance of SiN in the inner part of the wind is also higher. For the oxygen-  
873 rich outflow, the inner abundance of SiN is higher at  $\sim 10^{-7}$ , and it remains relatively  
874 constant until it begins to decrease at around  $10^{16}$  cm; SiN does not exhibit a shell-  
875 like distribution, as it would in the absence of a companion, but rather a parent-like  
876 distribution with a high inner abundance followed by a Gaussian decline caused by  
877 photodissociation driven by the interstellar radiation field. For the carbon-rich outflow,  
878 a shell-like distribution is seen in the presence of the companion, but the peak abundance  
879 is higher ( $\sim 10^{-6}$ ) and the inner abundance of SiN is several orders of magnitude higher  
880 ( $\sim 2 \times 10^{-9}$  relative to  $\text{H}_2$ ), than it would be if the companion were not present. An  
881 underlying assumption in these models is that the companion star is always close to  
882 the AGB star [4]. However, this is not the case for W Aql, as the projected distance  
883 between the F9 and AGB stars is presently 194 au or  $2.9 \times 10^{15}$  cm, rather than  $2 -$   
884  $5R_\star$  ( $4 - 10 \times 10^{13}$  cm) as assumed in the chemical models [4]. A highly elliptical  
885 orbit, during which the F9 star passes within a few stellar radii of the AGB star, could  
886 result in the asymmetric emission by SiN that we see in Fig. 1, if the F9 star only  
887 drove the production of SiN while it was sufficiently close to the AGB star. In this  
888 instance, the temporary close proximity of the two stars is relevant, because the wind  
889 region close to the AGB star is the densest and the chemical reactions will occur more  
890 readily. For example, at 5 au from the AGB star, the  $\text{H}_2$  number density is  $3 \times 10^9 \text{ cm}^{-3}$ ,  
891 whereas at the current projected distance of the F9 star, the number density is four  
892 orders of magnitude smaller, at  $3 \times 10^5 \text{ cm}^{-3}$ . Because the rates of chemical reactions  
893 generally depend on (the square of the) number density, a lower number density results

894 in a corresponding decrease in reaction rates, and hence much lower SiN production.  
 895 Even very fast periastron interactions (Table A.3) are still long enough to produce SiN,  
 896 particularly as, for example, the photoionisation of Si to Si<sup>+</sup> (Eq. 5) proceeds very  
 897 quickly in the presence of the companion.

898 Once formed, we expect SiN to persist in the expanding circumstellar envelope until  
 899 it is photodissociated by the interstellar radiation field, based on chemical modelling [4]  
 900 and because it is not expected to participate in the formation of dust or other molecular  
 901 species. In general, the photodestruction timescale of a molecule being dissociated by  
 902 the interstellar radiation field depends on the photodissociation rate for that molecule  
 903 and on the extinction, with higher extinctions meaning that fewer photons will penetrate  
 904 to that region. This is taken into account in the chemical models and accounts for the  
 905 drop off in abundance in the outer regions of the CSE (Fig. B.20), which, for SiN, agrees  
 906 with the location of the drop off we found from radiative transfer modelling (Methods  
 907 3.5). The additional UV photons originating from the F9 star only have a relatively local  
 908 effect on the chemistry of the CSE; as discussed in Methods 3.4.7 and 3.4.8 and shown  
 909 in Figures A.6 and A.9, the F9 star contributes to photodissociation of molecules in its  
 910 vicinity, but not on the opposite side of the CSE.

911 SiC behaves in a broadly similar way to SiN in the chemical models, with and with-  
 912 out the inclusion of a main sequence companion ([4] and the middle panel of Fig. B.20).  
 913 For both carbon- and oxygen-rich CSEs without a companion, SiC is expected to be dis-  
 914 tributed in a shell around the star, albeit with a more shallow gradient on either side of  
 915 the peak than for SiN. For the carbon-rich star with a density similar to W Aql, the peak  
 916 abundance of SiC is located at  $\sim 10^{16}$  cm from the AGB star and is found to be  $\sim 10^{-6}$   
 917 relative to H<sub>2</sub>, while for the oxygen-rich CSE, the peak of  $\sim 5 \times 10^{-9}$  is found slightly  
 918 farther from the star at  $\sim 3 \times 10^{16}$  cm. The presence of an F9-like companion alters the  
 919 SiC distribution in a similar way as for SiN, changing it from a shell-like distribution to  
 920 a more centralised distribution. The abundance in the inner part of the distribution (i.e.,  
 921 in the region from the inner edge of the model to  $\sim 10^{16}$  cm) increases up to  $\sim 2 \times 10^{-5}$   
 922 for carbon-rich CSE; and  $\sim 5 \times 10^{-9}$  for the oxygen-rich CSE, where there is previously  
 923 negligible SiC in this region without a companion (Fig. B.20).

924 Analogous with SiN (Eqs. 3 and 4), SiC mainly forms via



925 with the same source of Si<sup>+</sup> as explained in Eq. 5. CH<sub>3</sub> is formed either via photodis-  
 926 sociation of CH<sub>4</sub>, or through the successive hydrogenation of C. The former pathway  
 927 is dominant for carbon-rich CSEs, while the latter is more likely in oxygen-rich CSEs.  
 928 For an S-type star such as W Aql, both pathways may contribute to CH<sub>3</sub> formation.

929 The formation of both SiN and SiC is driven by Si<sup>+</sup>, which forms through the pho-  
 930 toionisation of Si (Eq. 5). In Fig. B.21 we plot the predicted abundances of Si<sup>+</sup> with and

931 without the presence of the F9 companion [4]. While the abundance of  $\text{Si}^+$  naturally  
 932 rises in the outer part of the envelope (beyond  $\sim 10^{16}$  cm), owing to the interstellar radi-  
 933 ation field, the inner abundance rises significantly in the presence of an F9-like compan-  
 934 ion. We note that although the abundance of  $\text{Si}^+$  rises to  $10^{-9}$  to  $10^{-7}$ , for oxygen- and  
 935 carbon-rich CSEs, respectively, this is still significantly less than the total abundance of  
 936 Si ( $6.5 \times 10^{-5}$  relative to  $\text{H}_2$ , assuming solar elemental abundances [92]), meaning that  
 937 the photoionisation process driven by the F9 star is not expected to ionise all the Si.

### 938 3.6.2 NS

939 In the absence of a companion, NS is expected to form in shell with a peak at about  
 940  $10^{16}$  cm [4]. For a carbon-rich CSE, the addition of an F9 companion does not cause  
 941 a significant difference in the NS distribution. For an oxygen-rich CSE, however, the  
 942 chemical model with an F9 like companion predicts a higher abundance of NS by almost  
 943 an order of magnitude and significantly changes the shape of the distribution, resulting  
 944 in a high abundance of NS in the inner wind ( $\sim 10^{-6}$  which decreases from around  
 945  $5 \times 10^{15}$  cm).

946 NS is formed via the photodissociation of  $\text{N}_2$  [4]



947 Even though the rate of photodissociation of  $\text{N}_2$  is relatively low because of the strong  
 948 bond, the abundance of  $\text{N}_2$  is thought to be high ( $4 \times 10^{-5}$  relative to  $\text{H}_2$  [93]). Therefore,  
 949 even if only  $\leq 1\%$  of  $\text{N}_2$  is destroyed, enough N is liberated to form NS [4]. The  
 950 predicted abundance distribution of N, taking into account the presence of an F9-like  
 951 companion, is plotted in Fig. B.21. The detection of NS is tentative (Fig. B.15), but  
 952 its co-location with the brightest region of SiN (especially in the PV diagram) and the  
 953 predictions of chemical models that include an F9-like companion ([4] and Fig. B.20),  
 954 suggest that NS was likely formed during the periastron passage of the W Aql system,  
 955 when the F9 star irradiated part of the inner wind.

### 956 3.6.3 HCN, CN and $\text{HC}_3\text{N}$

957 HCN, CN and  $\text{HC}_3\text{N}$  are closely linked species which have a wide astronomical litera-  
 958 ture in the context of the cyanopolyynes ( $\text{H}-(\text{C}\equiv\text{C})_n-\text{C}\equiv\text{N}$ ) family of molecules. HCN  
 959 is a parent species formed close to the star [93], and CN has long been known to be a  
 960 photodissociation product of HCN [27]. At low temperatures (below 800 K [94]), where  
 961  $\text{HC}_3\text{N}$  is seen towards W Aql, the main formation pathway for  $\text{HC}_3\text{N}$  is from the two  
 962 parent species HCN and  $\text{C}_2\text{H}_2$  [94, 95]:



963 For most molecular species, chemical fractionation of isotopologues is expected to  
964 be negligible around AGB stars. Hence, we can use the observations of  $\text{H}^{13}\text{CN}$  and  
965  $^{13}\text{CN}$  to understand the formation of  $\text{H}^{12}\text{C}_3\text{N}$ . For the rest of this section, we omit the  
966 isotope labels. As can be seen in Fig. 2, CN is preferentially detected on the side of the  
967 CSE where the F9 star is presently located, coinciding with a region of HCN depletion.  
968 We refer to this phenomenon as depletion because it aligns well with the location of the  
969 F9 star and of CN, and because the extent of HCN to the north east agrees well with the  
970 predicted extent of HCN in the chemical models, in the absence of a companion [4] (see  
971 also discussion in 3.6.4 below). Although the F9 star passes close to the AGB star during  
972 the eccentric orbit, the amount of time the stars spend close together is relatively short,  
973  $\lesssim 2\%$  of the orbital period (Table A.3 and Methods 3.9), compared with the amount  
974 of time the F9 star spends to the south west of the AGB star, providing a relatively  
975 consistent source of UV radiation. A similar pattern of molecular depletion is seen for  
976 SiO, SiS and CS (Fig. 2) for the same reason.

977  $\text{HC}_3\text{N}$  is present on the same side of the CSE as CN (Figs. 2 and B.16), from which  
978 we can infer that the presence of CN preferentially drives the formation of  $\text{HC}_3\text{N}$  to the  
979 south and west of the AGB star. Although  $\text{HC}_3\text{N}$  has long been known to be present  
980 around carbon stars, W Aql is the first S-type AGB star towards which  $\text{HC}_3\text{N}$  has been  
981 observed. Although  $\text{HC}_3\text{N}$  and other carbon-bearing molecules such as  $\text{C}_2\text{H}$  and  $\text{SiC}_2$   
982 seem to indicate a carbon-rich circumstellar chemistry for W Aql [47], the spectroscopic  
983 classification of W Aql marks it as an S-type star [18]. It is possible such carbon-bearing  
984 species are common around (some subset of) S-type stars more generally, but, to date,  
985 W Aql has been studied in the most detail.

986  $\text{HC}_3\text{N}$  has been most widely studied around the nearby carbon star CW Leo, where  
987 it is located mainly in a spherical shell centred on the star, well-resolved in ALMA  
988 observations and as predicted by chemical models [94, 4], with some enhancement in  
989 the inner regions which is thought to be driven by a companion [73]. We do not see  
990 a symmetric shell-like distribution of  $\text{HC}_3\text{N}$  around W Aql (Fig. B.16), however we  
991 interpret the  $\text{HC}_3\text{N}$  that we observe as part of a broken shell that is formed where CN is  
992 more abundant.

993 Although we expect that some CN — and subsequently  $\text{HC}_3\text{N}$  — would have formed  
994 during, or as a result of the periastron passage of the W Aql binary, these two molecules  
995 will have expanded with the CSE (as SiN has), to a radius that is comparable to the  
996 black circle in CO ( $1.35''$ , Fig. 3). At this distance from the AGB star, some CN might  
997 remain but is not easily detectable above the noise in our observations. Some traces of  
998  $^{13}\text{CN}$  are seen north of the AGB star in Fig. 2, but the SNR of the  $^{13}\text{CN}$  observation is  
999 relatively low, partly because more than half of the flux was resolved out (Table 1). We  
1000 also note that  $^{12}\text{CN}$ , expected to be around 10 to 30 times more abundant [21], was not  
1001 covered by our observations. Hence, we cannot conclusively determine how much CN  
1002 is present to the north east of the AGB star, relative to the apparently higher abundance

1003 of CN to the south west, closer to the F9 star. More sensitive observations, ideally cov-  
1004 ering  $^{12}\text{CN}$  and not subject to resolved out flux, would be required to fully understand  
1005 the distribution of CN around W Aql. We note the CN we expect to be co-located with  
1006 SiN, which should have formed during the periastron interaction, is harder to detect  
1007 than SiN is, for several reasons relating to the molecular physics and energy level dis-  
1008 tributions of the two molecules. Although SiN is also subject to hyperfine splitting, the  
1009 three most intense hyperfine components are only separated by  $\sim 1.4$  MHz, a tiny sepa-  
1010 ration compared with the  $30 \text{ km s}^{-1}$  (22 MHz) width of the SiN line, as can be seen in  
1011 Fig. B.13(b). In comparison, the spectrally resolved hyperfine splitting of CN results in  
1012 especially wide lines which have lower peak intensities than they would in the absence  
1013 of hyperfine splitting. This makes them harder to detect above the noise. Furthermore,  
1014 the dipole moment of SiN is around 1.8 times larger than for  $^{13}\text{CN}$  [96, 97], resulting in  
1015 intrinsically brighter lines for SiN.

1016 The excitation conditions of the observed lines of  $\text{HC}_3\text{N}$  are such that we do not  
1017 expect to see these same lines of  $\text{HC}_3\text{N}$  lines farther out in the wind than we do in  
1018 Fig. 2 ( $< 0.5''$ ). Therefore, if any  $\text{HC}_3\text{N}$  is present at a radius of  $1.35''$  from the AGB  
1019 star, we would not have detected it in the present observations. We predict that  $\text{HC}_3\text{N}$   
1020 in this region could be detected in more sensitive observations covering lower-energy  
1021 transition lines.

#### 1022 3.6.4 SiO, SiS and CS

1023 The emission seen from SiO, SiS and CS (Fig. A.6) — like that of HCN — indicates  
1024 photodissociation driven by the F9 star during its time to the southwest of the AGB star,  
1025 unlike SiN, SiC, and NS whose formation is driven by the brief but intense addition  
1026 of UV photons from the F9 star to the inner CSE during the periastron passage. This  
1027 process works because it is the products of photodissociation and photoionisation that  
1028 go on to form the observed SiN, SiC and NS. However, this is not the case for SiO,  
1029 SiS, CS and HCN, which are considered to be parent species in most chemical models  
1030 [4, 93]. Accordingly, the effect of a stellar companion is generally not to increase the  
1031 abundances of these molecules in the inner CSE, but may potentially deplete them [4].  
1032 Taking the case of a main sequence companion in the inner wind, the predictions are as  
1033 follows: (i) for SiO in an oxygen-rich CSE, a minimal decrease of the inner abundance  
1034 is predicted, compared with a decrease of almost an order of magnitude for the carbon-  
1035 rich CSE; (ii) for SiS, the models predict a significant decrease of several orders of  
1036 magnitude (4–6 dex) for both chemical types; however, this dramatic change could be  
1037 the result of an uncertain photodissociation rate for this molecule; (iii) for CS and HCN,  
1038 the change in abundance for both chemical types in the presence of a stellar companion  
1039 is negligible. Hence we can conclude that the asymmetric distributions seen for SiO,  
1040 SiS, CS and HCN (Fig. A.6 and B.18) are caused by photodissociation from the F9  
1041 companion, rather than enhanced formation during periastron.



### 3.7 Hydrodynamic simulations

To better understand the structure in the CO emission, we performed high-resolution 3D smoothed particle hydrodynamic (SPH, [98, 99]) simulations of highly eccentric systems with parameters similar to the W Aql system. These simulations were performed with the SPH code Phantom [100, 101, 102, 103]. The AGB star and companion are represented by gravity-only sink particles, and the wind consists of  $\sim 7 \times 10^6$  SPH gas particles that are gradually launched from boundary shells around the AGB star, with a velocity of  $13 \text{ km s}^{-1}$ , mimicking a free wind and a constant mass-loss rate [101]. Cooling within the wind is regulated by the equation of state for an ideal gas with polytropic index  $\gamma = 1.2$ , and the pulsations and rotation of the AGB star are not taken into account. It is important to note that these hydrodynamic simulations are necessarily simplified compared to observations, as they mainly account for the gravitational impact of the companion on the wind, and neglect the impact of additional effects such as radiation, radiation pressure, pulsations, realistic cooling, and [variable or anisotropic mass loss](#). We also note that the free wind approach does not reproduce velocities lower than  $13 \text{ km s}^{-1}$ , even though lower velocities are expected in the inner wind region (within  $\sim 80 \text{ au}$  of the AGB star). All of these contribute to the differences between the model and observations. Hence we aim for a qualitative understanding rather than a direct fit to the data.

We present results for a model with orbital parameters close to the W Aql system, with eccentricity  $e = 0.92$  and semi-major axis  $a = 125 \text{ au}$ , and taking the masses of the W Aql system (Methods 3.1). The Phantom model was evolved for around 5000 years and the snapshot that we plot in various figures was selected from a time step a little earlier than this to better match the current positions of the two stars. From a detailed analysis of the Phantom model we found that the orbital period increased slightly with time, owing to the mass being lost by the AGB star. This corresponded to a small increase in the semimajor axis but no change in the eccentricity over the time of the simulation. In Fig. 3c, we show the density distribution in a slice perpendicular to the orbital plane of this model. Plots of the same model showing the inner regions and a slice through the orbital plane are given in Fig. B.26. In general, we expect the companion to generate a spiral-like structure in the wind [102, 103, 104, 105]. However, owing to the high eccentricity of this system, concentric near-spherical density structures are created in the wind, visible as the near-circular structures in the edge-on density distribution in Figs. 3c and B.26b. The circular structures are not quite centred on either of the central stars but rather offset to the opposite side from the F9 position at apastron, similar to the offsets we find in the ALMA CO observations. These structures are remarkably similar to the circular structures traced out by the black and white circles in Fig. 3a. The offset centres of the circles, particularly the outer circle, agree well with the observed ALMA data (white circle in Fig. 3a). Similar structures at a  $90^\circ$  edge-on inclination were seen for other highly eccentric SPH simulations we performed, and are also seen in previous

1082 studies with  $e = 0.8$  and mass ratio  $M_1/M_2 = 2.75$ , compared with 1.5 for the W Aql  
1083 system [106].

1084 From a close study of our hydrodynamic simulations, we determine that the concen-  
1085 tric circles are formed during the relatively quick periastron passage of the F9 star. Dur-  
1086 ing the periastron passage, the stars reach their maximal orbital velocity ( $\sim 17 \text{ km s}^{-1}$  for  
1087 our chosen orbital parameters) and move hypersonically through the wind (which has a  
1088 sound speed of  $\sim 3 \text{ km s}^{-1}$  at 10 au), resulting in near-spherical shocks. The funnel-like  
1089 structure (see Fig. 3c) is formed through gravitational interactions between the com-  
1090 panion and the wind. More concretely, when the companion moves towards the AGB  
1091 star shortly before the periastron passage, its gravitational force results in a high-density  
1092 wake behind the companion (see first and second columns in Fig. B.23). Because there  
1093 is a velocity dispersion within this wake, it is delimited by a radially faster outer edge  
1094 and a denser inner edge. As the companion and the AGB star pass each other quickly  
1095 during periastron passage, the inner edge is shaped as a circular high-density shock,  
1096 that travels radially outwards and expands as the left side ( $x < 0$ ) of the 3D sphere-like  
1097 structure. Because the wind-companion interaction around periastron passage is strong,  
1098 the outer edge of the wake becomes a bow shock after periastron passage (second and  
1099 third columns of Fig. B.23, [103]). The formation of the spherical high-density shock is  
1100 enhanced, and is completed on the right side ( $x > 0$ ), by the fast wobble of the AGB star.  
1101 The orbital velocity of the stars reaches a maximum absolute value during this close en-  
1102 counter, however, the direction of the orbital velocity vectors changes by almost 180  
1103 degrees due to the elliptical nature of the orbit. The wobble of the AGB creates a strong  
1104 gradient in the radial wind velocity (mainly of the material on the  $x > 0$  side of the  
1105 AGB, where the wind is not disturbed by the companion shock wake). The transition  
1106 from faster outflowing material to slower wind particles results in a low-density region  
1107 (around  $x = 40\text{--}80$  au in the right column of Fig. B.23). The edge between this low-  
1108 density region and the inner denser material completes the spherical high-density shock  
1109 (see the bottom row of Fig. B.23, showing the orbit with an inclination of  $90^\circ$ ). The  
1110 spherical structures are slightly offset because of the movement of the stars. From this,  
1111 and the similar results of [106] and [71], we can conclude that such circular structures  
1112 are typical of highly elliptical systems, including when those systems are seen edge on.

1113 We emphasise that the circular structures are a consequence of binary interaction  
1114 and do not, in our model, represent a period of enhanced mass loss. This is in contrast  
1115 with the simplified model of CW Leo [71] where the increase in density was caused  
1116 by an assumed increase in mass-loss rate during periastron, in addition to the wobble  
1117 of the AGB star. [Some discussion of the impact of anisotropic mass loss is given in](#)  
1118 [the Supplementary Materials B.2](#). To illustrate the effect of our constant mass-loss rate,  
1119 we extracted the number density of our model along the  $x$ -axis with  $z = y = 0$  and  
1120 compared this with the 1D smooth model with an overdensity described in Methods 3.5  
1121 and [23]. In Fig. B.22a we show the number densities from the hydrodynamic model

1122 along the positive and negative  $x$  directions. Because the orbital parameters of our main  
1123 hydrodynamic model do not precisely match the orbital parameters that we derive in  
1124 this work, we performed an additional hydrodynamic model using the orbital solution  
1125 discussed in Methods 3.9 ( $e = 0.93, r_p = 10$  au). To reduce the required computational  
1126 resources, we set a large accretion radius for the F9 star (1 au compared with 0.05 au  
1127 in our main model), which reduces the more complex (and computationally expensive)  
1128 close gravitational interactions between the companion star and the wind particles. This  
1129 eliminates the funnel-like structure seen on the right of Fig. 3c but retains the sphere-  
1130 like structures resulting from the motions of the two stars. For this model, the same  
1131 number density plot, Fig. B.22b, reveals density peaks at radii in good agreement with  
1132 the overdensity found by [23]. Note that, overall, the number density of the hydro-  
1133 dynamic models can be averaged to equal the number density of a smooth 1D model  
1134 (without any overdensity). However, we also note that our main model, which better  
1135 allows for the close gravitational interactions between the wind and the F9 star, results  
1136 in a less symmetric distribution of over- and under-dense regions (as shown for the  $x$ -  
1137 axis in Fig. B.22a and seen in the funnel-like structure in Fig. 3c) and contributes to the  
1138 large-scale asymmetries discussed below.

1139 Based on the circular structures formed during periastron, we can estimate the time  
1140 of the most recent periastron from the expansion time of the black circle in Fig. 3a and  
1141 the orbital period from the difference in expansion times between the black and white  
1142 circles. These calculations are outlined in Methods 3.8. The fact that the black circle  
1143 overlaps with the edge of the SiN emission (Fig. 3b) also supports our hypothesis that  
1144 the SiN was created during the most recent periastron passage.

1145 To enable a better comparison of the SPH model to the observations, we processed  
1146 the Phantom model with the radiative transfer code MCFOST [107, 108], using the ef-  
1147 fective stellar temperatures of both the AGB (2300 K) and F9 (6000 K) stars and silicate  
1148 dust from [109]. The computation was sped up by only considering the lowest 6 CO  
1149 levels since this was sufficient for the task at hand. MCFOST includes a routine for  
1150 determining the photodissociation of CO by the interstellar UV field [110], which we  
1151 used to determine the drop off in CO distribution (set to  $6 \times 10^{-4}$  relative to H<sub>2</sub> at the  
1152 centre of the model), based on our 3D structures. This resulted in the near-complete  
1153 photodissociation of CO in the outermost density structures and left only (parts of) the  
1154 innermost four circular structures visible in CO. The resultant central velocity channel  
1155 is plotted in Fig. 3d, rotated to match the orientation of the W Aql system on the sky.  
1156 Although the model is not a perfect reproduction of the observed CO emission (expected  
1157 in light of the missing physics mentioned above), there are many qualitative similarities.  
1158 We also extracted an angle-radius plot from the central channel of the MCFOST output  
1159 (Fig. B.24), in which we see similar sinusoidal structures as those found in the observa-  
1160 tions (Figs. A.8 and B.25). The structures outlined by the pink and red circles identified  
1161 in Fig. 3a are not apparent in the MCFOST output, although they do qualitatively re-

1162 semble the structures formed at periastron. The main distinguishing feature is that the  
1163 pink and red circles are offset in the opposite direction (south rather than north). If we  
1164 were to ignore the offset and assume that one or both of these circles have the same  
1165 origin as the black and white circles, we find that the period calculated between all the  
1166 identified circles would be too short to agree with the HST and SPHERE observations  
1167 of the stellar separations. Therefore, the red and pink circles cannot have formed during  
1168 periastron. Noting that the Phantom model overestimates the wind velocity in the inner  
1169 regions, we suggest that the difference between the observed and modelled structures  
1170 partially arises from this as well as the other missing physics mentioned at the start of  
1171 this section.

1172 We also examined the channel maps generated by MCFOST at high and low ve-  
1173 locities and compared these with equivalent channels from the ALMA observations in  
1174 Fig. A.12. The observations are taken from channels  $\pm 13 \text{ km s}^{-1}$  from the LSR veloc-  
1175 ity of  $v_{\text{LSR}} = -23 \text{ km s}^{-1}$ . The blue channel exhibits CO emission elongated to the  
1176 southwest, approximately along the companion axis, while the red channel has a more  
1177 circular CO emitting region. These differences are qualitatively reproduced in their re-  
1178 spective MCFOST channels. This asymmetry in velocity space is also responsible for  
1179 the enhanced blue emission seen in the wings of several line profiles observed towards  
1180 W Aql [21]. The asymmetry arises from the orientation of the orbital plane such that  
1181 the observations are reproduced if the Phantom model is orientated so that motion of  
1182 the F9 star at periastron is into the plane of the sky.

1183 Finally, we comment on the large-scale asymmetry to the southwest, revealed by  
1184 past observations, in the CO [22] and dust [19, 20] emission on scales of  $10''$  and  $60''$ .  
1185 Although this more extended emission is in the same direction as the F9 star, the emis-  
1186 sion extent is much larger than the current or maximal separation between AGB and F9  
1187 stars ( $\sim 0.5$  to  $0.8''$ , Fig. 4). The luminosity of the F9 star is insufficient for its radiation  
1188 to drive the dust outwards, as the AGB star does (Supplementary Materials B.1); in-  
1189 stead, it contributes to the large-scale shaping of the wind through its gravitational pull.  
1190 We do not detect any accretion disc around the F9 star, either in the ALMA continuum  
1191 or in any molecular lines, and an accretion disc is not predicted for the W Aql system  
1192 by the SPH model. However, the F9 star does gravitationally attract some circumstel-  
1193 lar material, which is then pushed outwards by the radiation pressure from the AGB  
1194 star, and results in the large scale asymmetry seen in the dust and more extended gas  
1195 [19, 20, 22], and reproduced in our hydrodynamic model. The enhanced emission in this  
1196 direction can be seen in the full extent of the central CO channel output by MCFOST  
1197 (Fig. B.26c), where the CO extends out farther to the southwest.

### 1198 **3.8 Orbital parameters from ALMA observations**

1199 Here we constrain some orbital parameters from the ALMA observations. First we make  
1200 an estimate of the period based on the round structures seen in the CO observations. As

1201 determined in Methods 3.7, the black and white circles shown in Fig. 3 were created  
 1202 during periastron interactions between the AGB and F9 stars. Assuming the velocity  
 1203 profile from Eq. 2, we find the expansion time between the two circles, and hence the  
 1204 orbital period, through the integral:

$$T = \int_{R_{\text{black}}}^{R_{\text{white}}} \frac{dr}{v(r)} = \int_{R_{\text{black}}}^{R_{\text{white}}} \frac{dr}{v_0 + (v_\infty - v_0) \left(1 - \frac{R_{\text{in}}}{r}\right)^\beta} \quad (9)$$

1205 where  $R_{\text{black}}$  and  $R_{\text{white}}$  are the radii of the black and white circles, and  $R_{\text{in}} = 2 \times 10^{14}$  cm  
 1206 is the dust condensation radius, with  $v_0 = 3 \text{ km s}^{-1}$  the velocity for  $r < R_{\text{in}}$ , taken to  
 1207 be the sound speed [21]. The period is found to be  $1082_{-108}^{+89}$  years. The uncertainty is  
 1208 based on the width of the circles as fit from the angle-radius plot (Fig. A.8). There we  
 1209 found the uncertainties in the radii of the circles to be  $10.75 \pm 0.75''$  for the white circle  
 1210 and  $1.35 \pm 0.10''$  for the black circle.

1211 Another crucial parameter needed to constrain the orbital solution of the W Aql  
 1212 system is the time since periastron. As previously discussed, the most recent periastron  
 1213 passage generated the black circle seen in CO (Fig. 3) and the arc of SiN (Fig. 1). We can  
 1214 estimate the time of periastron by calculating the expansion time of these two structures.  
 1215 Since we are now considering expansion in the inner part of the envelope, we need to  
 1216 also consider the velocity inside the dust condensation radius, which we assume to be  
 1217 close to the sound speed at  $v = 3 \text{ km s}^{-1}$ . Equation 9 can then be rewritten:

$$\Delta t = \int_{R_{\text{in}}}^{R_{\text{black}}} \frac{dr}{v_0 + (v_\infty - v_0) \left(1 - \frac{R_{\text{in}}}{r}\right)^\beta} + \int_{R_{\text{form}}}^{R_{\text{in}}} \frac{dr}{v_0} \quad (10)$$

1218 where  $R_{\text{black}}$  is the radius of the black circle and the radial extent of the SiN arc, and  
 1219  $R_{\text{form}}$  is the radial distance at which these two structures formed.

1220 The value of  $R_{\text{form}}$  is uncertain so we take it to be the periastron distance between  
 1221 stars. The smallest periastron distance we obtain is  $\sim 3$  au, while the largest is equal  
 1222 to the dust condensation radius. Using these values as a guide and assuming a constant  
 1223 velocity of  $v_0 = 3 \text{ km s}^{-1}$  for  $r < R_{\text{in}} = 2 \times 10^{14}$  cm, we estimate the time since the  
 1224 most recent periastron as  $172 \pm 22$  years ago. These derived values are listed with other  
 1225 orbital parameters in Table A.2.

1226 Finally, we can determine the direction of the orbit from the PV diagrams of the  
 1227 species formed at periastron, namely SiN, SiC, and NS. Taking into account that 1) the  
 1228 redder emission is brighter for all three of these molecules (and indeed only red emission  
 1229 is seen above the noise in the NS PV diagram, Fig. B.15) and 2) the line profiles of SiN  
 1230 and SiC are slightly blue-shifted relative to the stellar LSR velocity, suggests that these  
 1231 species formed first on the blue side of the envelope and then more recently on the red  
 1232 side. Hence, there has been slightly more time for the blue emission to expand, shifting  
 1233 the line profiles and PV diagrams bluewards. From this we conclude that the direction

1234 of the periastron passage was, for the F9 star, into the plane of the sky. This agrees with  
 1235 the evidence from the SPH model discussed above.

### 1236 **3.9 Orbital solutions**

1237 The orbit of the W Aql system cannot be solved analytically, so instead we solve it  
 1238 numerically by calculating a series of possible orbits and checking which agree with  
 1239 the parameters derived from observations (i.e. the parameters listed in Table A.2). We  
 1240 adjust our basic orbital solution by leaving as free parameters the eccentricity,  $e$ , and the  
 1241 periastron distance,  $r_p$ . All other primary orbital parameters are either input from prior  
 1242 results or calculated from  $e$  and  $r_p$  as follows.

1243 The apastron,  $r_a$ , is defined by

$$r_a = r_p \left( \frac{e + 1}{1 - e} \right) \quad (11)$$

1244 and the semimajor axis,  $a$ , is then

$$a = \frac{r_p + r_a}{2}. \quad (12)$$

1245 Working in the reference frame of the AGB star, we define the focus of the ellipse traced  
 1246 by the F9 star as the location of the AGB star, defined here as (0,0,0) in our cartesian  
 1247 co-ordinate scheme.

1248 From the system mass ( $M + m = 2.66 M_\odot$ ) and the semimajor axis, we can then  
 1249 calculate the orbital period,  $T$

$$T = 2\pi \sqrt{\left( \frac{a^3}{G(M + m)} \right)}. \quad (13)$$

1250 This is enough information to plot a top-down view of the orbit, as shown in Fig.  
 1251 B.27. However, we know from observations that the orbit is inclined and rotated in  
 1252 the plane of the sky (relative to north). From the observations of SiN, we estimate the  
 1253 inclination angle of the orbit to be close to edge-on,  $i = 90 \pm 7^\circ$ . We plot  $i = 85^\circ$   
 1254 to better illustrate the orbit in the plane of the sky, but note that a completely edge-  
 1255 on system ( $i = 90^\circ$ ) satisfies the observations and does not significantly change our  
 1256 results. From the photometry of the two stars, we rotate the orbit in the plane of the  
 1257 sky by  $\omega = 120^\circ$  to fit the SPHERE observation (Fig. 4). We note that the uncertainty  
 1258 in  $\omega$  comes mainly from the precise values of the inclination and eccentricity, but the  
 1259 selection of  $\omega = 120^\circ$  is a good fit given the rest of our results. The sky projection of a  
 1260 selected orbit and the locations of the stars are plotted in Fig. 4. We assume no rotation  
 1261 out of the plane of the sky along the third orthogonal axis because the relative symmetry  
 1262 of the SiN PV-diagram (Fig. 1b) suggests this value is small ( $< 5^\circ$ ).

1263 For a possible orbital solution, we must calculate the time since periastron and the  
 1264 time between the SPHERE and HST observations. For this we must consider the angle  
 1265  $\theta$  made between the periastron, the AGB star and the F9 star, as well as the eccentric  
 1266 anomaly,  $E$ . Both of these angles are shown in Fig. B.27 and are mathematically related  
 1267 by

$$\tan\left(\frac{\theta}{2}\right) = \tan\left(\frac{E}{2}\right) \sqrt{\frac{1+e}{1-e}} \quad (14)$$

$$E = 2 \tan^{-1}\left(\tan\left(\frac{\theta}{2}\right) \sqrt{\frac{1-e}{1+e}}\right) . \quad (15)$$

1268 The time since periastron,  $\Delta t$ , can then be calculated

$$\Delta t = \frac{T}{2\pi} (E - e \sin(E)) . \quad (16)$$

1269 We also check the possible solution against the known time between the HST and  
 1270 SPHERE observations by comparing  $\Delta t_{\text{SPHERE}} - \Delta t_{\text{HST}}$  against the time difference be-  
 1271 tween those observations.

1272 To find the best solutions, we modify the input parameters ( $r_p$  and  $e$ ) until we find a  
 1273 suitable orbit which agrees with the values we found for the period, time since periastron  
 1274 and time between HST and SPHERE observations. Because of the uncertainties, we find  
 1275 a group of compatible solutions rather than one single definition of the orbit. From a  
 1276 grid with steps of  $\Delta e = 0.01 \in [0.70, 0.99]$  and  $\Delta r_p = 0.1 \times 10^{14} \text{ cm} \in [0.4 \times 10^{14} \text{ cm}, 5 \times$   
 1277  $10^{14} \text{ cm}]$ , we found a set of compatible solutions, all of which are given in Table A.3.  
 1278 For the highest eccentricities  $e > 0.95$  we additionally tested a finer grid for  $r_p$ , with  
 1279  $\Delta r_p = 0.5 \times 10^{13} \text{ cm} \in [5 \times 10^{13} \text{ cm}, 1 \times 10^{14} \text{ cm}]$ , because the orbital timing becomes  
 1280 sensitive to small variations in  $r_p$  at these high eccentricities. The compatible solutions  
 1281 range from the extremes of  $e = 0.98$ ,  $r_p = 4.5 \times 10^{13} \text{ cm}$  to  $e = 0.91$ ,  $r_p = 2.0 \times 10^{14} \text{ cm}$ .  
 1282 We plot one of these solutions ( $e = 0.93$ ,  $r_p = 1.5 \times 10^{14} \text{ cm}$ ) in Fig. 4, where we  
 1283 also show the orbit superposed on the HST and SPHERE photometric observations.  
 1284 Note that although some of our solutions have very small periastron distances, none are  
 1285 smaller than the Roche limit, so direct accretion of the AGB star onto the F9 star is not  
 1286 expected.

1287 In Table A.3, we also include  $t_{\text{close}}$  which we define as the time the AGB and F9 stars  
 1288 spend “close” to each other. More precisely, in the AGB frame, this is the time the F9  
 1289 star takes to pass through the  $-90^\circ \leq \theta \leq 90^\circ$  region of the orbit (see Fig. B.27) and can  
 1290 be derived from equations 15 and 16. As noted in Table A.3,  $t_{\text{close}}$  ranges from 2 years  
 1291 at the highest eccentricity to 18 years at  $e = 0.91$ . This corresponds to  $\sim 0.1$  to 2% of  
 1292 the total orbital period.

## 1293 **Data Availability**

1294 The observational data used here is openly available through the data archives for ALMA  
1295 (<https://almascience.nrao.edu/aq/>), ESO for the APEX and SPHERE data (<http://archive.eso.org>), and HST (<https://hla.stsci.edu>). Custom ALMA data  
1296 products are available from TD or AMSR upon reasonable request.  
1297

## 1298 **Code Availability**

1299 Phantom is open source under the GPLv3 license and can be downloaded via <https://github.com/danieljprice/phantom>. MCFOST is open source under the GPLv3  
1300 license and can be downloaded via <https://mcfost.readthedocs.io/en/latest/overview.html>. ALI, the 1D radiative transfer code, is available from TD upon rea-  
1301 sonable request.  
1302  
1303

## 1304 **References**

- 1305 [1] Höfner, S. & Olofsson, H. Mass loss of stars on the asymptotic giant branch.  
1306 Mechanisms, models and measurements. *The Astronomy and Astrophysics Re-*  
1307 *view* **26**, 1 (2018).
- 1308 [2] Kobayashi, C., Karakas, A. I. & Lugaro, M. The Origin of Elements from Carbon  
1309 to Uranium. *The Astrophysical Journal* **900**, 179 (2020). 2008.04660.
- 1310 [3] Decin, L. *et al.* Reduction of the maximum mass-loss rate of OH/IR stars due to  
1311 unnoticed binary interaction. *Nature Astronomy* 213 (2019). 1902.09259.
- 1312 [4] Van de Sande, M. & Millar, T. J. The impact of stellar companion UV photons  
1313 on the chemistry of the circumstellar environments of AGB stars. *MNRAS* **510**,  
1314 1204–1222 (2022). 2111.05053.
- 1315 [5] De Marco, O. *et al.* The messy death of a multiple star system and the resulting  
1316 planetary nebula as observed by jwst. *Nature Astronomy* **6**, 1421–1432 (2022).  
1317 URL <https://doi.org/10.1038/s41550-022-01845-2>.
- 1318 [6] Decin, L. *et al.* (sub)stellar companions shape the winds of evolved stars. *Sci-*  
1319 *ence* **369**, 1497–1500 (2020). URL [https://science.sciencemag.org/](https://science.sciencemag.org/content/369/6510/1497)  
1320 [content/369/6510/1497](https://science.sciencemag.org/content/369/6510/1497). [https://science.sciencemag.org/content/](https://science.sciencemag.org/content/369/6510/1497.full.pdf)  
1321 [369/6510/1497.full.pdf](https://science.sciencemag.org/content/369/6510/1497.full.pdf).
- 1322 [7] Jorissen, A. AGB Stars in Binaries and Their Progeny. In *Asymptotic Giant*  
1323 *Branch Stars*, 461–518 (Springer, 2004).



- 1324 [8] Karovska, M., Hack, W., Raymond, J. & Guinan, E. First Hubble Space Tele-  
1325 scope Observations of Mira AB Wind-accreting Binary Systems. *The Astrophys-*  
1326 *ical Journal Letters* **482**, L175–L178 (1997).
- 1327 [9] Ramstedt, S. *et al.* The wonderful complexity of the Mira AB system. *Astronomy*  
1328 *& Astrophysics* **570**, L14 (2014). 1410.1529.
- 1329 [10] Kervella, P. *et al.* ALMA observations of the nearby AGB star L<sub>2</sub> Puppis. I. Mass  
1330 of the central star and detection of a candidate planet. *Astronomy & Astrophysics*  
1331 **596**, A92 (2016). 1611.06231.
- 1332 [11] Homan, W. *et al.* ATOMIUM: A high-resolution view on the highly asymmetric  
1333 wind of the AGB star  $\pi^1$ Grus. I. First detection of a new companion and its effect  
1334 on the inner wind. *Astronomy & Astrophysics* **644**, A61 (2020). 2010.05509.
- 1335 [12] Mauron, N. & Huggins, P. J. Imaging the circumstellar envelopes of AGB stars.  
1336 *Astronomy & Astrophysics* **452**, 257–268 (2006). astro-ph/0602623.
- 1337 [13] Kim, H. *et al.* The large-scale nebular pattern of a superwind binary in an eccen-  
1338 tric orbit. *Nature Astronomy* **1**, 0060 (2017). 1704.00449.
- 1339 [14] Maercker, M. *et al.* Unexpectedly large mass loss during the thermal pulse cycle  
1340 of the red giant star R Sculptoris. *Nature* **490**, 232–234 (2012). 1210.3030.
- 1341 [15] Sahai, R. *et al.* The Rapidly Evolving Asymptotic Giant Branch Star, V Hya:  
1342 ALMA Finds a Multiring Circus with High-velocity Outflows. *The Astrophysical*  
1343 *Journal* **929**, 59 (2022). 2202.09335.
- 1344 [16] Ramos-Larios, G. *et al.* Rings and arcs around evolved stars - I. Fingerprints  
1345 of the last gasps in the formation process of planetary nebulae. *MNRAS* **462**,  
1346 610–635 (2016).
- 1347 [17] Herbig, G. H. Physical Companions to Long-Period Variables. *Veroeffentlichun-*  
1348 *gen der Remeis-Sternwarte zu Bamberg* **27**, 164 (1965).
- 1349 [18] Danilovich, T., Olofsson, G., Black, J. H., Justtanont, K. & Olofsson, H. Clas-  
1350 sifying the secondary component of the binary star W Aquilae. *Astronomy &*  
1351 *Astrophysics* **574**, A23 (2015). 1501.00863.
- 1352 [19] Ramstedt, S., Maercker, M., Olofsson, G., Olofsson, H. & Schöier, F. L. Imaging  
1353 the circumstellar dust around AGB stars with PolCor. *Astronomy & Astrophysics*  
1354 **531**, A148 (2011). 1105.5405.

- 1355 [20] Mayer, A. *et al.* Large-scale environments of binary AGB stars probed by Her-  
1356 schel. I. Morphology statistics and case studies of R Aquarii and W Aquilae.  
1357 *Astronomy & Astrophysics* **549**, A69 (2013). 1211.3595.
- 1358 [21] Danilovich, T. *et al.* Detailed modelling of the circumstellar molecular line emis-  
1359 sion of the S-type AGB star W Aquilae. *Astronomy & Astrophysics* **569**, A76  
1360 (2014).
- 1361 [22] Ramstedt, S. *et al.* The circumstellar envelope around the S-type AGB star W  
1362 Aql. Effects of an eccentric binary orbit. *Astronomy & Astrophysics* **605**, A126  
1363 (2017). 1709.07327.
- 1364 [23] Brunner, M. *et al.* Molecular line study of the S-type AGB star W Aquilae.  
1365 ALMA observations of CS, SiS, SiO and HCN. *Astronomy & Astrophysics* **617**,  
1366 A23 (2018). 1806.01622.
- 1367 [24] Danilovich, T. *et al.* ATOMIUM: halide molecules around the S-type AGB star  
1368 W Aquilae. *Astronomy & Astrophysics* **655**, A80 (2021). 2109.04747.
- 1369 [25] Richichi, A., Percheron, I. & Khristoforova, M. CHARM2: An updated Catalog  
1370 of High Angular Resolution Measurements. *Astronomy & Astrophysics* **431**, 773–  
1371 777 (2005).
- 1372 [26] Turner, B. E. Detection of SiN in IRC +10216. *The Astrophysical Journal Letters*  
1373 **388**, L35 (1992).
- 1374 [27] Huggins, P. J., Glassgold, A. E. & Morris, M. CN and C<sub>2</sub>H in IRC +10216. *The*  
1375 *Astrophysical Journal* **279**, 284–290 (1984).
- 1376 [28] Montargès, M. *et al.* The VLT/SPHERE view of the ATOMIUM cool evolved  
1377 star sample. I. Overview: Sample characterization through polarization analysis.  
1378 *Astronomy & Astrophysics* **671**, A96 (2023). 2301.02081.
- 1379 [29] Tokovinin, A. & Kiyaveva, O. Eccentricity distribution of wide binaries. *MNRAS*  
1380 **456**, 2070–2079 (2016). 1512.00278.
- 1381 [30] Boffin, H. M. J., Cerf, N. & Paulus, G. Statistical analysis of a sample of spec-  
1382 troscopic binaries containing late-type giants. *Astronomy & Astrophysics* **271**,  
1383 125–138 (1993).
- 1384 [31] Moe, M. & Di Stefano, R. Mind Your Ps and Qs: The Interrelation between Pe-  
1385 riod (P) and Mass-ratio (Q) Distributions of Binary Stars. *Astrophysical Journal*  
1386 *Supplement Series* **230**, 15 (2017). 1606.05347.

- 1387 [32] Maercker, M. *et al.* A detailed view of the gas shell around R Sculptoris with  
1388 ALMA. *Astronomy & Astrophysics* **586**, A5 (2016). 1512.01350.
- 1389 [33] Lykou, F. *et al.* The curious case of II Lup: a complex morphology revealed with  
1390 SAM/NACO and ALMA. *MNRAS* **480**, 1006–1021 (2018). 1808.00279.
- 1391 [34] Doan, L. *et al.* The extended molecular envelope of the asymptotic giant branch  
1392 star  $\pi^1$  Gruis as seen by ALMA. I. Large-scale kinematic structure and CO exci-  
1393 tation properties. *Astronomy & Astrophysics* **605**, A28 (2017). 1709.09435.
- 1394 [35] Sahai, R., Scibelli, S. & Morris, M. R. High-speed Bullet Ejections during the  
1395 AGB-to-Planetary Nebula Transition: HST Observations of the Carbon Star, V  
1396 Hydrae. *The Astrophysical Journal* **827**, 92 (2016). 1605.06728.
- 1397 [36] Oomen, G.-M. *et al.* Orbital properties of binary post-AGB stars. *Astronomy &*  
1398 *Astrophysics* **620**, A85 (2018). 1810.01842.
- 1399 [37] Jorissen, A., Van Eck, S., Mayor, M. & Udry, S. Insights into the formation of  
1400 barium and Tc-poor S stars from an extended sample of orbital elements. *Astron-*  
1401 *omy & Astrophysics* **332**, 877–903 (1998). astro-ph/9801272.
- 1402 [38] Ramstedt, S., Schöier, F. L. & Olofsson, H. Circumstellar molecular line emis-  
1403 sion from S-type AGB stars: mass-loss rates and SiO abundances. *Astronomy &*  
1404 *Astrophysics* **499**, 515–527 (2009). 0903.1672.
- 1405 [39] Knapp, G. R. & Morris, M. Mass loss from evolved stars. III - Mass loss rates  
1406 for fifty stars from CO J = 1-0 observations. *The Astrophysical Journal* **292**,  
1407 640–669 (1985).
- 1408 [40] Jura, M. Mass Loss from S Stars. *Astrophysical Journal Supplement Series* **66**,  
1409 33 (1988).
- 1410 [41] Groenewegen, M. & De Jong, T. Co observations and mass loss of ms-  
1411 and s-stars. *Astronomy & Astrophysics* **337**, 797–807 (1998). URL <http://www.scopus.com/inward/record.url?eid=2-s2.0-0001632031&partnerID=40&md5=083cdfb2ae34c4d507fffc05fd912f9b>.
- 1412  
1413
- 1414 [42] Gaia Collaboration *et al.* The Gaia mission. *Astronomy & Astrophysics* **595**, A1  
1415 (2016). 1609.04153.
- 1416 [43] Andriantsaralaza, M., Ramstedt, S., Vlemmings, W. H. T. & De Beck, E. Dis-  
1417 tance estimates for AGB stars from parallax measurements. *arXiv e-prints*  
1418 arXiv:2209.03906 (2022). 2209.03906.

- 1419 [44] Gaia Collaboration *et al.* Gaia Early Data Release 3. Summary of the contents  
1420 and survey properties. *Astronomy & Astrophysics* **649**, A1 (2021). 2012.01533.
- 1421 [45] Habets, G. M. H. J. & Heintze, J. R. W. Empirical bolometric corrections for  
1422 the main-sequence. *Astronomy & Astrophysics Supplement Series* **46**, 193–237  
1423 (1981).
- 1424 [46] De Nutte, R. *et al.* Nucleosynthesis in AGB stars traced by oxygen isotopic ratios.  
1425 I. Determining the stellar initial mass by means of the  $^{17}\text{O}/^{18}\text{O}$  ratio. *Astronomy*  
1426 *& Astrophysics* **600**, A71 (2017). 1606.07445.
- 1427 [47] De Beck, E. & Olofsson, H. The surprisingly carbon-rich environment of the  
1428 S-type star W Aql. *Astronomy & Astrophysics* **642**, A20 (2020). 2007.01756.
- 1429 [48] Vassiliadis, E. & Wood, P. R. Evolution of low- and intermediate-mass stars to  
1430 the end of the asymptotic giant branch with mass loss. *The Astrophysical Journal*  
1431 **413**, 641–657 (1993).
- 1432 [49] Maire, A. L. *et al.* High-precision Astrometric Studies in Direct Imaging with  
1433 SPHERE. *The Messenger* **183**, 7–12 (2021). 2103.13700.
- 1434 [50] Gottlieb, C. A. *et al.* ATOMIUM: ALMA tracing the origins of molecules in dust  
1435 forming oxygen rich M-type stars. Motivation, sample, calibration, and initial  
1436 results. *Astronomy & Astrophysics* **660**, A94 (2022). 2112.04399.
- 1437 [51] The CASA Team *et al.* CASA, the Common Astronomy Software Applications  
1438 for Radio Astronomy. *arXiv e-prints* arXiv:2210.02276 (2022). 2210.02276.
- 1439 [52] Thompson, A. R., Moran, J. M. & Swenson, J., George W. *Interferometry and*  
1440 *Synthesis in Radio Astronomy, 3rd Edition* (Springer, Berlin Heidelberg, 2017).
- 1441 [53] Winnewisser, G., Belov, S. P., Klaus, T. & Schieder, R. Sub-Doppler Measure-  
1442 ments on the Rotational Transitions of Carbon Monoxide. *Journal of Molecular*  
1443 *Spectroscopy* **184**, 468–472 (1997).
- 1444 [54] Cernicharo, J., Gottlieb, C. A., Guelin, M., Thaddeus, P. & Vrtilik, J. M. Astro-  
1445 nomical and Laboratory Detection of the SiC Radical. *The Astrophysical Journal*  
1446 *Letters* **341**, L25 (1989).
- 1447 [55] Bogey, M., Demuynck, C. & Destombes, J. L. Laboratory Measurement of the  
1448 Submillimeter Wave Spectrum of SiC and Isotopomers. *Astronomy & Astro-*  
1449 *physics* **232**, L19 (1990).

- 1450 [56] Lee, S. K., Ozeki, H. & Saito, S. Microwave Spectrum of the NS Radical in the 2  
1451 Pi R Ground Electronic State. *Astrophysical Journal Supplement Series* **98**, 351  
1452 (1995).
- 1453 [57] Yamada, K. M. T., Moravec, A. & Winnewisser, G. Sub-millimeter Wave Spec-  
1454 tra of Cyanoacetylene and Revised Ground State Constants. *Zeitschrift Natur-  
1455 forschung Teil A* **50**, 1179–1181 (1995).
- 1456 [58] Müller, H. S. P. *et al.* Rotational Spectroscopy of Isotopologues of Silicon  
1457 Monoxide, SiO, and Spectroscopic Parameters from a Combined Fit of Rota-  
1458 tional and Rovibrational Data. *Journal of Physical Chemistry A* **117**, 13843–  
1459 13854 (2013).
- 1460 [59] Müller, H. S. P. *et al.* Rotational spectroscopy of the isotopic species of silicon  
1461 monosulfide, SiS. *Physical Chemistry Chemical Physics* **9**, 1579 (2007).
- 1462 [60] Gottlieb, C. A., Myers, P. C. & Thaddeus, P. Precise Millimeter-Wave Laboratory  
1463 Frequencies for CS and C<sup>34</sup>S. *The Astrophysical Journal* **588**, 655–661 (2003).
- 1464 [61] Ahrens, V. *et al.* Sub-Doppler Saturation Spectroscopy of HCN up to 1 THz  
1465 and Detection of J = 3 —<sub>i</sub> 2 (4—<sub>i</sub> 3) Emission from TMC1. *Zeitschrift Natur-  
1466 forschung Teil A* **57**, 669–681 (2002).
- 1467 [62] Fuchs, U. *et al.* High Resolution Spectroscopy of HCN Isotopomers: H<sup>13</sup>CN,  
1468 HC<sup>15</sup>N, and H<sup>13</sup>C<sup>15</sup>N in the Ground and First Excited Bending Vibrational  
1469 State. *Zeitschrift Naturforschung Teil A* **59**, 861–872 (2004).
- 1470 [63] Bogey, M., Demuyne, C. & Destombes, J. L. The millimetre wave spectrum of  
1471 the <sup>13</sup>C<sup>14</sup>N radical in its ground state. *Canadian Journal of Physics* **62**, 1248–  
1472 1253 (1984).
- 1473 [64] Müller, H. S. P., Thorwirth, S., Roth, D. A. & Winnewisser, G. The Cologne  
1474 Database for Molecular Spectroscopy, CDMS. *Astronomy & Astrophysics* **370**,  
1475 L49–L52 (2001).
- 1476 [65] Müller, H. S. P., Schlöder, F., Stutzki, J. & Winnewisser, G. The Cologne  
1477 Database for Molecular Spectroscopy, CDMS: a useful tool for astronomers and  
1478 spectroscopists. *J Mol. Struct.* **742**, 215–227 (2005).
- 1479 [66] Olofsson, H., Eriksson, K., Gustafsson, B. & Carlstrom, U. A study of cir-  
1480 cumstellar envelopes around bright carbon stars. I - Structure, kinematics, and  
1481 mass-loss rate. *Astrophysical Journal Supplement Series* **87**, 267–304 (1993).

- 1482 [67] Homan, W. *et al.* ATOMIUM: The astounding complexity of the near circum-  
1483 stellar environment of the M-type AGB star R Hydrae. I. Morpho-kinematical  
1484 interpretation of CO and SiO emission. *Astronomy & Astrophysics* **651**, A82  
1485 (2021).
- 1486 [68] Vlemmings, W. H. T., Khouri, T. & Olofsson, H. Resolving the extended stel-  
1487 lar atmospheres of asymptotic giant branch stars at (sub)millimetre wavelengths.  
1488 *Astronomy & Astrophysics* **626**, A81 (2019). 1904.06374.
- 1489 [69] Baudry, A. *et al.* ATOMIUM: Probing the inner wind of evolved O-rich stars  
1490 with new, highly excited H<sub>2</sub>O and OH lines. *Astronomy & Astrophysics* **674**,  
1491 A125 (2023). 2305.03171.
- 1492 [70] Massalkhi, S. *et al.* Abundance of SiC<sub>2</sub> in carbon star envelopes. *Astronomy &*  
1493 *Astrophysics* **611**, A29 (2018). 1710.11409.
- 1494 [71] Cernicharo, J., Marcelino, N., Agúndez, M. & Guélin, M. Molecular shells in  
1495 IRC+10216: tracing the mass loss history. *Astronomy & Astrophysics* **575**, A91  
1496 (2015). 1412.1948.
- 1497 [72] Decin, L. *et al.* ALMA data suggest the presence of spiral structure in the inner  
1498 wind of CW Leonis. *Astronomy & Astrophysics* **574**, A5 (2015). 1410.2060.
- 1499 [73] Siebert, M. A., Van de Sande, M., Millar, T. J. & Remijan, A. J. Investigat-  
1500 ing Anomalous Photochemistry in the Inner Wind of IRC+10216 through Inter-  
1501 ferometric Observations of HC<sub>3</sub>N. *The Astrophysical Journal* **941**, 90 (2022).  
1502 2210.14941.
- 1503 [74] Patel, N., Gottlieb, C. & Young, K. Probing the dust formation zone in  
1504 IRC+10216 with the SMA. In *Proceedings of The Life Cycle of Dust in the*  
1505 *Universe: Observations*, 98 (2013).
- 1506 [75] Velilla-Prieto, L. *et al.* Circumstellar chemistry of Si-C bearing molecules in the  
1507 C-rich AGB star IRC+10216. *IAU Symposium* **343**, 535–537 (2019).
- 1508 [76] Velilla Prieto, L. *et al.* The millimeter IRAM-30 m line survey toward IK Tauri.  
1509 *Astronomy & Astrophysics* **597**, A25 (2017). 1609.01904.
- 1510 [77] Decin, L., Richards, A. M. S., Danilovich, T., Homan, W. & Nuth, J. A. ALMA  
1511 spectral line and imaging survey of a low and a high mass-loss rate AGB star  
1512 between 335 and 362 GHz. *Astronomy & Astrophysics* **615**, A28 (2018). 1801.  
1513 09291.

- 1514 [78] Decin, L. *et al.* Discovery of multiple dust shells beyond 1 arcmin in the circum-  
1515 stellar envelope of IRC +10216 using Herschel/PACS. *Astronomy & Astrophysics*  
1516 **534**, A1 (2011). 1210.3483.
- 1517 [79] Guélin, M. *et al.* IRC +10 216 in 3D: morphology of a TP-AGB star envelope.  
1518 *Astronomy & Astrophysics* **610**, A4 (2018). 1709.04738.
- 1519 [80] Schöier, F. L. *et al.* The abundance of HCN in circumstellar envelopes of AGB  
1520 stars of different chemical type. *Astronomy & Astrophysics* **550**, A78 (2013).  
1521 1301.2129.
- 1522 [81] Danilovich, T. *et al.* Sulphur-bearing molecules in AGB stars. II. Abundances  
1523 and distributions of CS and SiS. *Astronomy & Astrophysics* **617**, A132 (2018).  
1524 1807.05144.
- 1525 [82] Massalkhi, S., Agúndez, M. & Cernicharo, J. Study of CS, SiO, and SiS abun-  
1526 dances in carbon star envelopes: assessing their role as gas-phase precursors of  
1527 dust. *Astronomy & Astrophysics* **628**, A62 (2019). 1906.09461.
- 1528 [83] Morris, M. & Jura, M. Molecular self-shielding in the outflows from late-type  
1529 stars. *The Astrophysical Journal* **264**, 546–553 (1983).
- 1530 [84] Bachiller, R. *et al.* A survey of CN in circumstellar envelopes. *Astronomy &*  
1531 *Astrophysics* **319**, 235–243 (1997).
- 1532 [85] Rybicki, G. B. & Hummer, D. G. An accelerated lambda iteration method for  
1533 multilevel radiative transfer. I - Non-overlapping lines with background contin-  
1534 uum. *Astronomy & Astrophysics* **245**, 171–181 (1991).
- 1535 [86] Pickett, H. M. The fitting and prediction of vibration-rotation spectra with spin  
1536 interactions. *Journal of Molecular Spectroscopy* **148**, 371–377 (1991).
- 1537 [87] Lique, F. *et al.* Rotational excitation of CN(X  $^2\Sigma^+$ ) by He: Theory and compari-  
1538 son with experiments. *Journal of Chemical Physics* **132**, 024303 (2010).
- 1539 [88] Montez, J., Rodolfo, Ramstedt, S., Kastner, J. H., Vlemmings, W. & Sanchez,  
1540 E. A Catalog of GALEX Ultraviolet Emission from Asymptotic Giant Branch  
1541 Stars. *The Astrophysical Journal* **841**, 33 (2017). 1705.05371.
- 1542 [89] Schrijver, C. J. Magnetic structure in cool stars. XI. Relations between radia-  
1543 tive fluxes measuring stellar activity, and evidence for two components in stellar  
1544 chromospheres. *Astronomy & Astrophysics* **172**, 111–123 (1987).

- 1545 [90] Gálvez, M. C. *et al.* Multiwavelength optical observations of chromospheri-  
1546 cally active binary systems. IV. The X-ray/EUV selected binary BK Psc (2RE  
1547 J0039+103). *Astronomy & Astrophysics* **389**, 524–536 (2002). astro-ph/  
1548 0204490.
- 1549 [91] Gray, R., Corbally, C. & Burgasser, A. *Stellar Spectral Classification*. Princeton  
1550 Series in Astrophysics (Princeton University Press, 2009). URL [http://books.](http://books.google.com.au/books?id=S_Sh1i226wwC)  
1551 [google.com.au/books?id=S\\_Sh1i226wwC](http://books.google.com.au/books?id=S_Sh1i226wwC).
- 1552 [92] Asplund, M., Amarsi, A. M. & Grevesse, N. The chemical make-up of the Sun:  
1553 A 2020 vision. *Astronomy & Astrophysics* **653**, A141 (2021). 2105.01661.
- 1554 [93] Agúndez, M., Martínez, J. I., de Andres, P. L., Cernicharo, J. & Martín-Gago,  
1555 J. A. Chemical equilibrium in AGB atmospheres: successes, failures, and  
1556 prospects for small molecules, clusters, and condensates. *Astronomy & Astro-*  
1557 *physics* **637**, A59 (2020). 2004.00519.
- 1558 [94] Agúndez, M. *et al.* Growth of carbon chains in IRC +10216 mapped with ALMA.  
1559 *Astronomy & Astrophysics* **601**, A4 (2017). 1702.04429.
- 1560 [95] Cordiner, M. A. & Millar, T. J. Density-Enhanced Gas and Dust Shells in a New  
1561 Chemical Model for IRC+10216. *The Astrophysical Journal* **697**, 68–78 (2009).  
1562 0903.0890.
- 1563 [96] Kerkines, I. S. K. & Mavridis, A. On the electron affinity of SiN and spectro-  
1564 scopic constants of SiN<sup>-</sup>. *Journal of Chemical Physics* **123**, 124301–124301  
1565 (2005).
- 1566 [97] Thomson, R. & Dalby, F. W. Experimental determination of the dipole moments  
1567 of the X(<sup>2</sup>Σ<sup>+</sup>) and B(<sup>2</sup>Σ<sup>+</sup>) states of the CN molecule. *Canadian Journal of Physics*  
1568 **46**, 2815 (1968).
- 1569 [98] Monaghan, J. J. Smoothed particle hydrodynamics. *Reports on Progress in*  
1570 *Physics* **68**, 1703–1759 (2005).
- 1571 [99] Price, D. J. Smoothed particle hydrodynamics and magnetohydrodynamics. *Jour-*  
1572 *nal of Computational Physics* **231**, 759–794 (2012). 1012.1885.
- 1573 [100] Price, D. J. *et al.* Phantom: A Smoothed Particle Hydrodynamics and Magneto-  
1574 hydrodynamics Code for Astrophysics. *Publications of the Astronomical Society*  
1575 *of Australia* **35**, e031 (2018). 1702.03930.
- 1576 [101] Siess, L., Homan, W., Toupin, S. & Price, D. J. 3D simulations of AGB stellar  
1577 winds. I. Steady winds and dust formation. *Astronomy & Astrophysics* **667**, A75  
1578 (2022). 2208.13869.



- 1579 [102] Maes, S. *et al.* SPH modelling of companion-perturbed AGB outflows including  
 1580 a new morphology classification scheme. *Astronomy & Astrophysics* **653**, A25  
 1581 (2021). 2107.00505.
- 1582 [103] Malfait, J. *et al.* SPH modelling of wind-companion interactions in eccentric  
 1583 AGB binary systems. *Astronomy & Astrophysics* **652**, A51 (2021). 2107.01074.
- 1584 [104] Mastrodemos, N. & Morris, M. Bipolar Preplanetary Nebulae: Hydrodynam-  
 1585 ics of Dusty Winds in Binary Systems. I. Formation of Accretion Disks. *The*  
 1586 *Astrophysical Journal* **497**, 303–329 (1998).
- 1587 [105] Mastrodemos, N. & Morris, M. Bipolar Pre-Planetary Nebulae: Hydrodynam-  
 1588 ics of Dusty Winds in Binary Systems. II. Morphology of the Circumstellar En-  
 1589 velopes. *The Astrophysical Journal* **523**, 357–380 (1999).
- 1590 [106] Kim, H., Liu, S.-Y. & Taam, R. E. Templates of Binary-induced Spiral-shell  
 1591 Patterns around Mass-losing Post-main-sequence Stars. *Astrophysical Journal*  
 1592 *Supplement Series* **243**, 35 (2019). 1906.06333.
- 1593 [107] Pinte, C., Ménard, F., Duchêne, G. & Bastien, P. Monte Carlo radiative trans-  
 1594 fer in protoplanetary disks. *Astronomy & Astrophysics* **459**, 797–804 (2006).  
 1595 astro-ph/0606550.
- 1596 [108] Pinte, C. *et al.* Benchmark problems for continuum radiative transfer. High op-  
 1597 tical depths, anisotropic scattering, and polarisation. *Astronomy & Astrophysics*  
 1598 **498**, 967–980 (2009). 0903.1231.
- 1599 [109] Weingartner, J. C. & Draine, B. T. Dust Grain-Size Distributions and Extinction  
 1600 in the Milky Way, Large Magellanic Cloud, and Small Magellanic Cloud. *The*  
 1601 *Astrophysical Journal* **548**, 296–309 (2001). astro-ph/0008146.
- 1602 [110] Pinte, C. *et al.* Direct mapping of the temperature and velocity gradients in discs.  
 1603 Imaging the vertical CO snow line around IM Lupi. *Astronomy & Astrophysics*  
 1604 **609**, A47 (2018). 1710.06450.
- 1605 [111] Tielens, A. G. G. M. Stationary flows in the circumstellar envelopes of M giants.  
 1606 *The Astrophysical Journal* **271**, 702–716 (1983).
- 1607 [112] Ohnaka, K., Weigelt, G. & Hofmann, K. H. Clumpy dust clouds and extended  
 1608 atmosphere of the AGB star W Hydrae revealed with VLT/SPHERE-ZIMPOL  
 1609 and VLTI/AMBER. *Astronomy & Astrophysics* **589**, A91 (2016). 1603.01197.
- 1610 [113] Khouri, T. *et al.* Study of the inner dust envelope and stellar photosphere of the  
 1611 AGB star R Doradus using SPHERE/ZIMPOL. *Astronomy & Astrophysics* **591**,  
 1612 A70 (2016). 1605.05504.

- 1613 [114] Wittkowski, M. *et al.* Aperture synthesis imaging of the carbon AGB star R  
1614 Sculptoris. Detection of a complex structure and a dominating spot on the stellar  
1615 disk. *Astronomy & Astrophysics* **601**, A3 (2017). 1702.02574.
- 1616 [115] Paladini, C. *et al.* Large granulation cells on the surface of the giant star  $\pi^1$  Gruis.  
1617 *Nature* **553**, 310–312 (2018).
- 1618 [116] Khouri, T. *et al.* Inner dusty envelope of the AGB stars W Hydrae, SW Virginis,  
1619 and R Crateris using SPHERE/ZIMPOL. *Astronomy & Astrophysics* **635**, A200  
1620 (2020). 2003.06195.
- 1621 [117] Freytag, B. & Höfner, S. Three-dimensional simulations of the atmosphere of an  
1622 AGB star. *Astronomy & Astrophysics* **483**, 571–583 (2008).
- 1623 [118] Freytag, B., Liljegren, S. & Höfner, S. Global 3D radiation-hydrodynamics mod-  
1624 els of AGB stars. Effects of convection and radial pulsations on atmospheric  
1625 structures. *Astronomy & Astrophysics* **600**, A137 (2017). 1702.05433.
- 1626 [119] Freytag, B. & Höfner, S. Global 3D radiation-hydrodynamical models of AGB  
1627 stars with dust-driven winds. *Astronomy & Astrophysics* **669**, A155 (2023).  
1628 2301.11836.
- 1629 [120] Vlemmings, W. *et al.* The shock-heated atmosphere of an asymptotic giant  
1630 branch star resolved by alma. *Nature Astronomy* **1**, 848–853 (2017). URL  
1631 <https://doi.org/10.1038/s41550-017-0288-9>.
- 1632 [121] Takigawa, A., Kamizuka, T., Tachibana, S. & Yamamura, I. Dust formation and  
1633 wind acceleration around the aluminum oxide-rich AGB star W Hydrae. *Science*  
1634 *Advances* **3** (2017).
- 1635 [122] Khouri, T. *et al.* Detection of highly excited OH towards AGB stars. A new probe  
1636 of shocked gas in the extended atmospheres. *Astronomy & Astrophysics* **623**, L1  
1637 (2019). 1902.11033.
- 1638 [123] Velilla-Prieto, L. *et al.* Atmospheric molecular blobs shape up circumstellar  
1639 envelopes of agb stars. *Nature* (2023). URL <https://doi.org/10.1038/s41586-023-05917-9>.
- 1641 [124] Martin, W. C., deL. Musgrove, A. R., Kotochigova, S. & Sansonetti, J. E. Ground  
1642 levels and ionization energies for the neutral atoms (1998). URL <https://api.semanticscholar.org/CorpusID:103628738>.
- 1644 [125] Aydi, E. & Mohamed, S. 3D models of the circumstellar environments of evolved  
1645 stars: Formation of multiple spiral structures. *MNRAS* **513**, 4405–4430 (2022).  
1646 2203.08318.

1647

1648 Correspondence and requests for materials should be addressed to Taïssa Danilovich.

## 1649 **Acknowledgements**

1650 We would like to thank Se-Hyung Cho of the Korean VLBI Network for KVN observa-  
1651 tions of W Aql to confirm consistency with our ALMA results. TD is supported in part  
1652 by the Australian Research Council through a Discovery Early Career Researcher Award  
1653 (DE230100183). TD and SHJW acknowledge support from the Research Foundation  
1654 Flanders (FWO) through grants 12N9920N, and 1285221N, respectively. JM and SM  
1655 acknowledge support from the Research Foundation Flanders (FWO) grant G099720N.  
1656 MVdS acknowledges support from European Union’s Horizon 2020 research and in-  
1657 novation programme under the Marie Skłodowska-Curie grant agreement No 882991.  
1658 MM acknowledges funding from the Programme Paris Region fellowship supported  
1659 by the Région Ile-de-France. PK acknowledges funding from the European Research  
1660 Council (ERC) under the European Union’s Horizon 2020 research and innovation pro-  
1661 gram (synergy grant project UniverScale, grant agreement 951549). TJM is grateful  
1662 to the STFC for support through grant ST/P000312/1 and thanks the Leverhulme Trust  
1663 for the award of an Emeritus Fellowship. JMCP was supported by STFC grant number  
1664 ST/T000287/1. LD, JMCP, SHJW, SM and DG acknowledge support from ERC consol-  
1665 idator grant 646758 AEROSOL. EDB acknowledges support from the Swedish National  
1666 Space Agency. DG was funded by the project grant ‘The Origin and Fate of Dust in Our  
1667 Universe’ from the Knut and Alice Wallenberg Foundation. EC acknowledges funding  
1668 from the KU Leuven C1 grant MAESTRO C16/17/007. FH, AB and LM acknowledge  
1669 funding from the French National Research Agency (ANR) project PEPPER (ANR-20-  
1670 CE31- 0002). KTW acknowledges support from the European Research Council (ERC)  
1671 under the European Union’s Horizon 2020 research and innovation programme (Grant  
1672 agreement no. 883867, project EXWINGS). AZ is funded by STFC/UKRI through  
1673 grant ST/T000414/1. This project has received funding from the Framework Program  
1674 for Research and Innovation “Horizon 2020” under the convention Marie Skłodowska-  
1675 Curie No 945298. Computational resources and services used in this work were pro-  
1676 vided by the VSC (Flemish Supercomputer Center), funded by the Research Foundation  
1677 Flanders (FWO) and the Flemish Government – department EWI. This research was un-  
1678 dertaken with the assistance of resources and services from the National Computational  
1679 Infrastructure (NCI), which is supported by the Australian Government. This paper  
1680 makes use of the following ALMA data: ADS/JAO.ALMA#2018.1.00659.L. ALMA is  
1681 a partnership of ESO (representing its member states), NSF (USA) and NINS (Japan),  
1682 together with NRC (Canada), MOST and ASIAA (Taiwan), and KASI (Republic of  
1683 Korea), in cooperation with the Republic of Chile. The Joint ALMA Observatory is

1684 operated by ESO, AUI/NRAO and NAOJ. Based on observations collected at the Euro-  
1685 pean Organisation for Astronomical Research in the Southern Hemisphere under ESO  
1686 programme 0103.D-0772(A). We acknowledge excellent support from the UK ALMA  
1687 Regional Centre (UK ARC), which is hosted by the Jodrell Bank Centre for Astro-  
1688 physics (JBCA) at the University of Manchester. The UK ARC Node is supported by  
1689 STFC Grant ST/P000827/1.

## 1690 **Author contributions**

1691 TD conceived of and led this publication, analysed and interpreted data, performed  
1692 the radiative transfer models, wrote the manuscript, and created most of the figures.  
1693 JM performed and interpreted the hydrodynamics model and made figures 3c, B.23,  
1694 and B.26a&b. MVdS led the chemical interpretation and made figures B.20 and B.21.  
1695 MM and PK contributed the analysis of the resolved imaging. AMSR performed the  
1696 ALMA data reduction. FDC and AC contributed to the 3D interpretation of the data.  
1697 TJM and JMCP contributed to the chemical interpretation. CAG contributed to the line  
1698 identifications and interpretation. CP assisted in the MCFOST modelling. DJP assisted  
1699 in the Phantom modelling and interpretation. EDB contributed the fully-reduced APEX  
1700 data. The ALMA proposal was led by LD and CAG, with contributions from MM, TD,  
1701 AdK, KMM, RS, AMSR, JMCP, HSPM, EDB, PK, AB, KTW, MVdS, EL, DG, JY and  
1702 DJP. All authors commented on the manuscript and analysis.

## A Extended Data

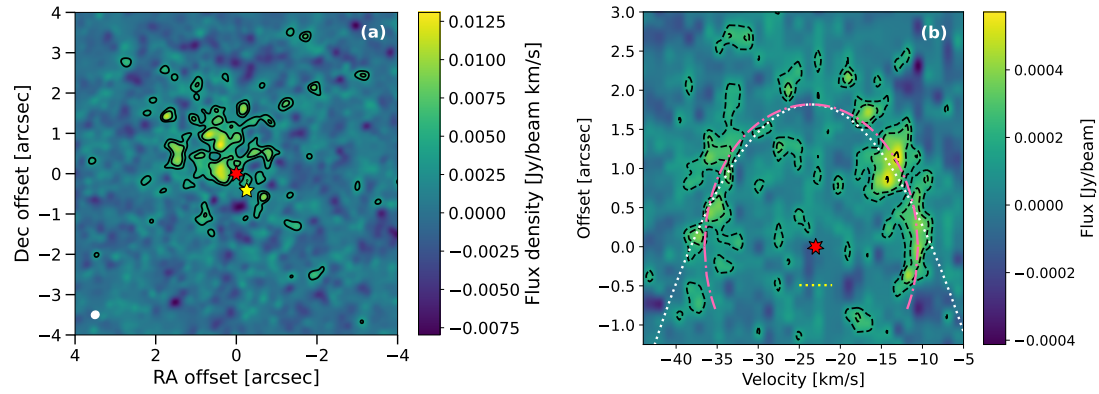


Figure A.5: **(a)** Zeroth moment map of SiC towards W Aql with contours at levels of  $3$  and  $5\sigma$ . Transition details are given in Table 1. North is up and east is to the left. The position of the AGB star is indicated by the red star at  $(0,0)$  and the location of the F9 companion is indicated by the yellow star to the south-west. North is up and east is left. The white ellipse in the bottom left corner indicates the size of the synthesised beam. **(b)** Position-velocity diagram of SiC towards W Aql, taken with the same wide slit as used for SiN (Fig. 1), with a position angle of north  $33^\circ$  east. Dashed black contours are at levels of  $3$  and  $5\sigma$ , a dotted white parabola is fit to the data (see Methods 3.4.3), and a dash-dotted pink ellipse is plotted to emphasise the shape of the emission in the PV diagram. The position and LSR velocity of the AGB star is indicated by the red star and the horizontal yellow dotted line indicates the present offset of the F9 star.

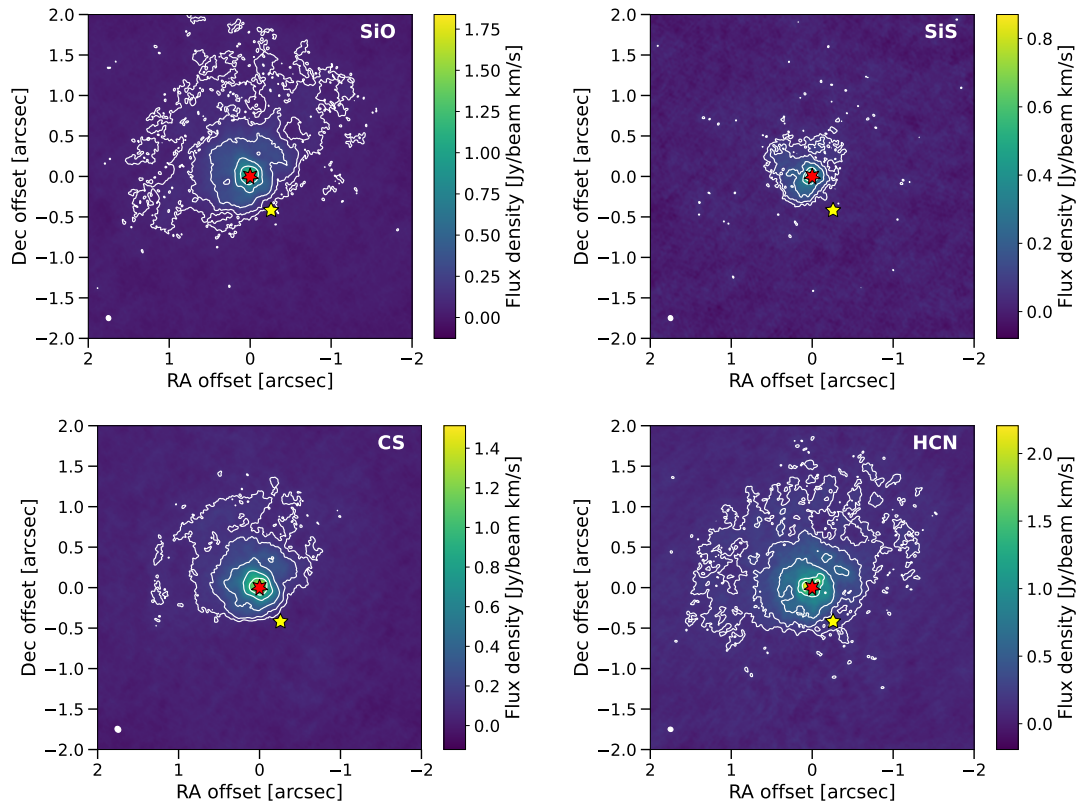


Figure A.6: Zeroth moment maps of SiO, SiS, CS and HCN towards W Aql (transitions give in Table 1). White contours are at levels of 3, 5, 10, 20, and  $30\sigma$ . The position of the AGB star is indicated by the red star at (0,0) and the location of the F9 companion is indicated by the yellow star to the south-west. North is up and east is left. The white ellipses in the bottom left corners indicate the sizes of the synthesised beams.

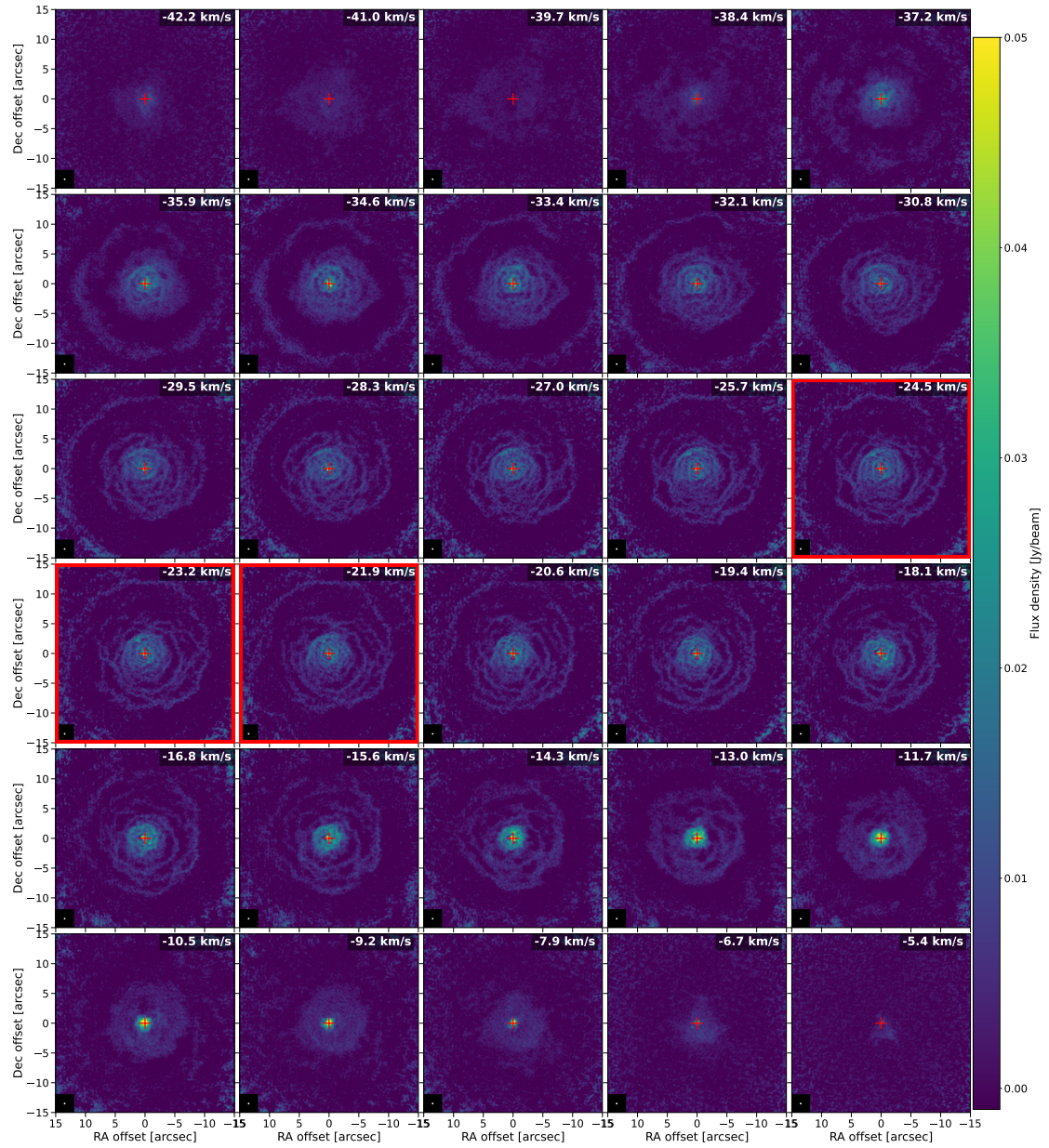


Figure A.7: Channel maps of CO ( $J = 2 \rightarrow 1$ ) towards W Aql, obtained by combining observations from three configurations of ALMA. The AGB star is located at (0,0) and is marked by a red cross. The LSR velocity of each channel is given in the top right hand corner and the three channels closest to the W Aql  $v_{\text{LSR}} = -23 \text{ km s}^{-1}$  are highlighted with red borders and summed for Fig. 3. The synthetic beam is given by the white ellipse in the bottom left corner of each channel. North is up and east is left.

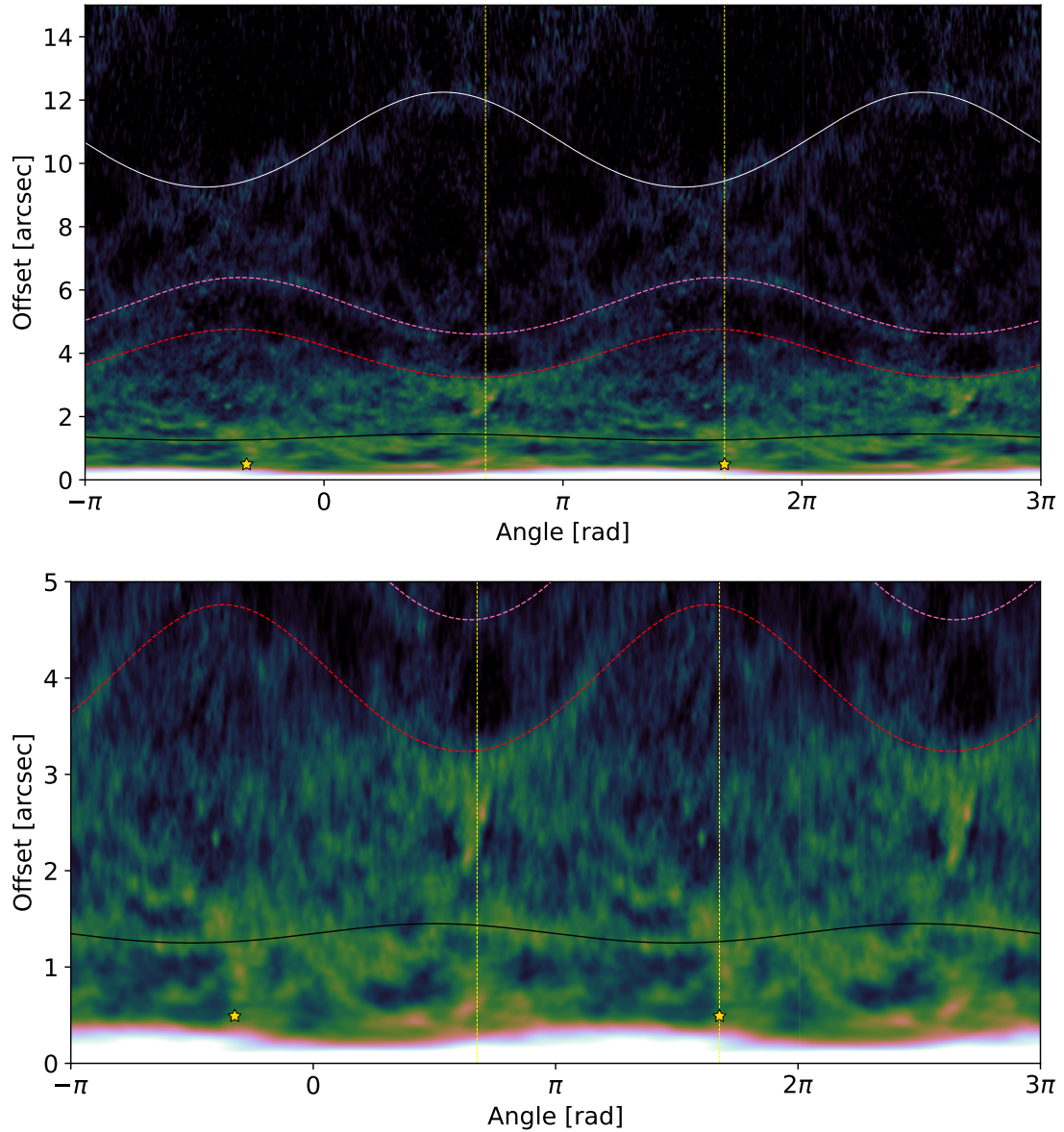


Figure A.8: Plots showing the radial emission distribution against angle for the summed central three channels of CO (Fig. 3) with a full revolution [shown in the centre \(0 to  \$2\pi\$ \)](#) and [half a revolution is shown on either side \( \$-\pi\$  to 0 and  \$2\pi\$  to  \$3\pi\$ \)](#) to show how the [structures extend onwards](#). The location of the F9 star is indicated by the yellow star and a yellow dotted line which passes through both stars and is plotted in the central winding to guide the eye. The black, red and white curves correspond to the same features highlighted in Fig. 3. The top plot shows the full observed extent of the CO emission (out to 15'') and the bottom plot focuses on the regions out to 5'' from the AGB star. [These plots are reproduced in the Supplementary Materials Fig. B.25 without the additional curves.](#)



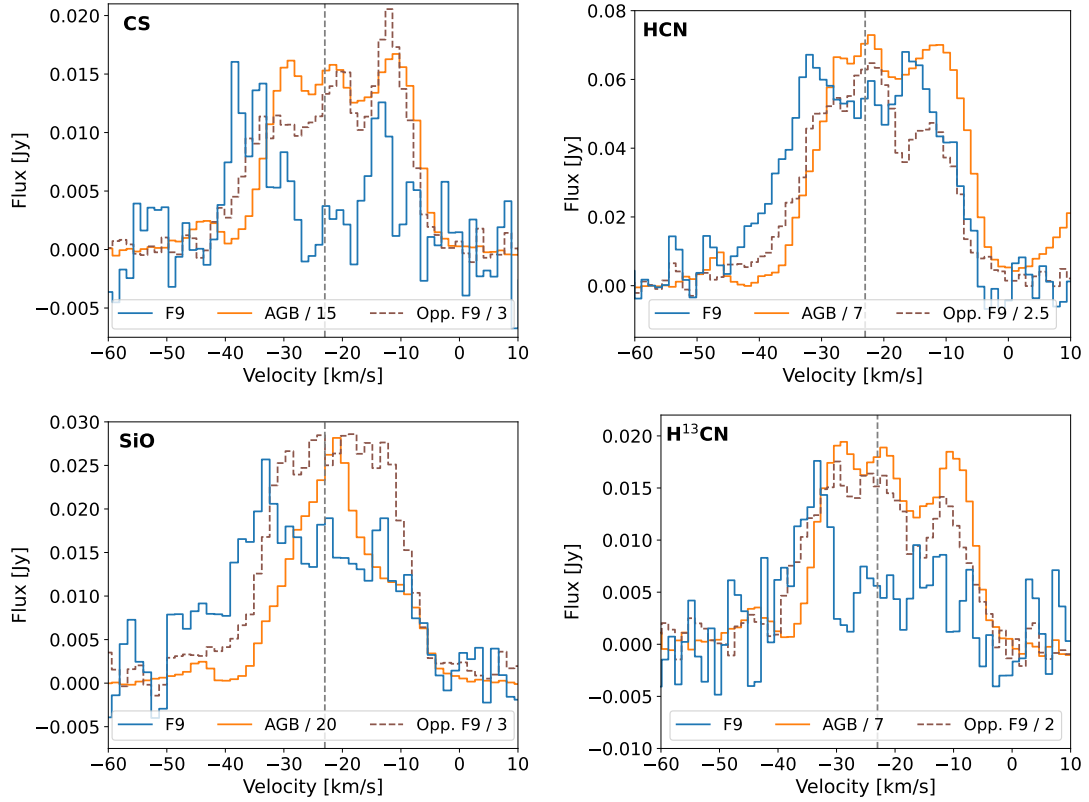


Figure A.9: Plots of CS, HCN, SiO and H<sup>13</sup>CN emission extracted from circular apertures with 100 mas radii centred on the F9 star (blue), on the AGB star (orange) and at the same separation as the F9 star but on the opposite side of the AGB (Opp. F9, brown, dashed). (See Table 1 for line frequencies.) The AGB and Opp. F9 line profiles are scaled by the factor given in the legend to facilitate comparison with the F9 line profiles. The vertical grey line indicates  $v_{\text{LSR}} = -23 \text{ km s}^{-1}$ .

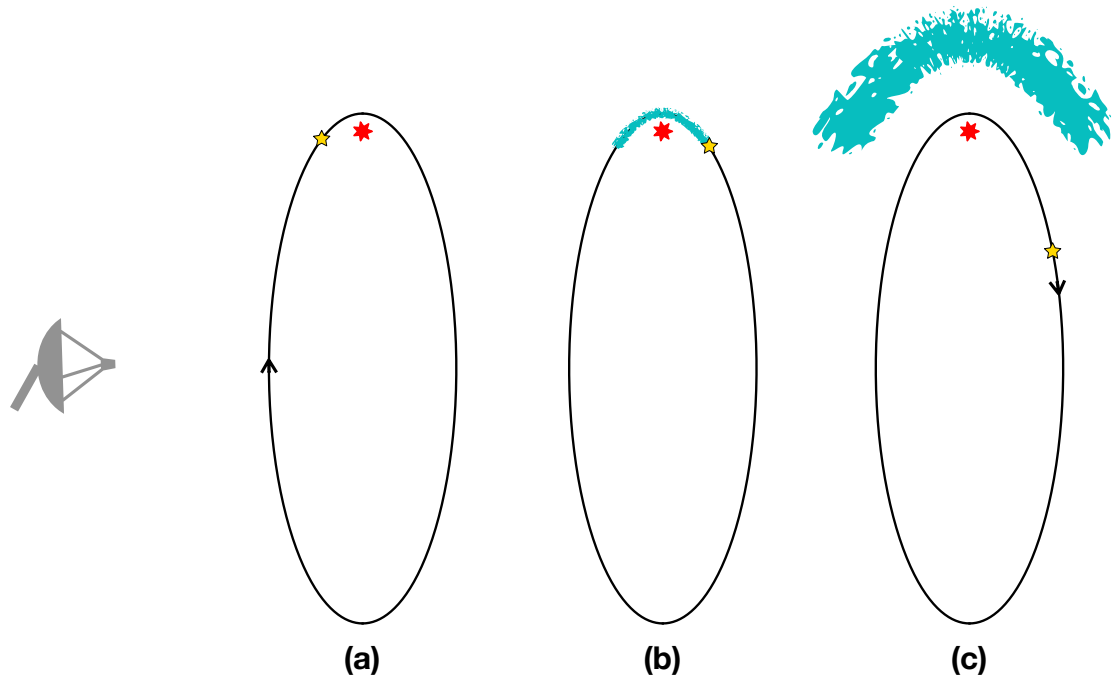


Figure A.10: A series of sketches illustrating the formation of SiN (or, similarly, SiC or NS) during the periastron passage of the W Aql system. The orbit (black line) is shown face on in the frame of the AGB star and the F9 star is assumed to be moving clockwise. Relative to our observations, the observer is located to the left, represented by the radio dish. **(a)** The F9 star (yellow) approaches the AGB star (red) and enters the dense inner wind region ( $n_{\text{H}_2} \sim 10^8$  to  $10^{10} \text{ cm}^{-3}$ ). **(b)** The rapid periastron passage is completed and SiN has formed in the wake of the F9 star (cyan region), with formation initiated by the F9 UV flux (see Methods 3.6). **(c)** As the F9 star continues on its orbit, the arc of SiN expands away from the AGB star, along with the stellar wind in which it is embedded. The present-day configuration of SiN can be seen in Fig. 1, where the PV diagram is a good approximation of the final arc shape that would be seen around the AGB star were the orbit viewed face-on.

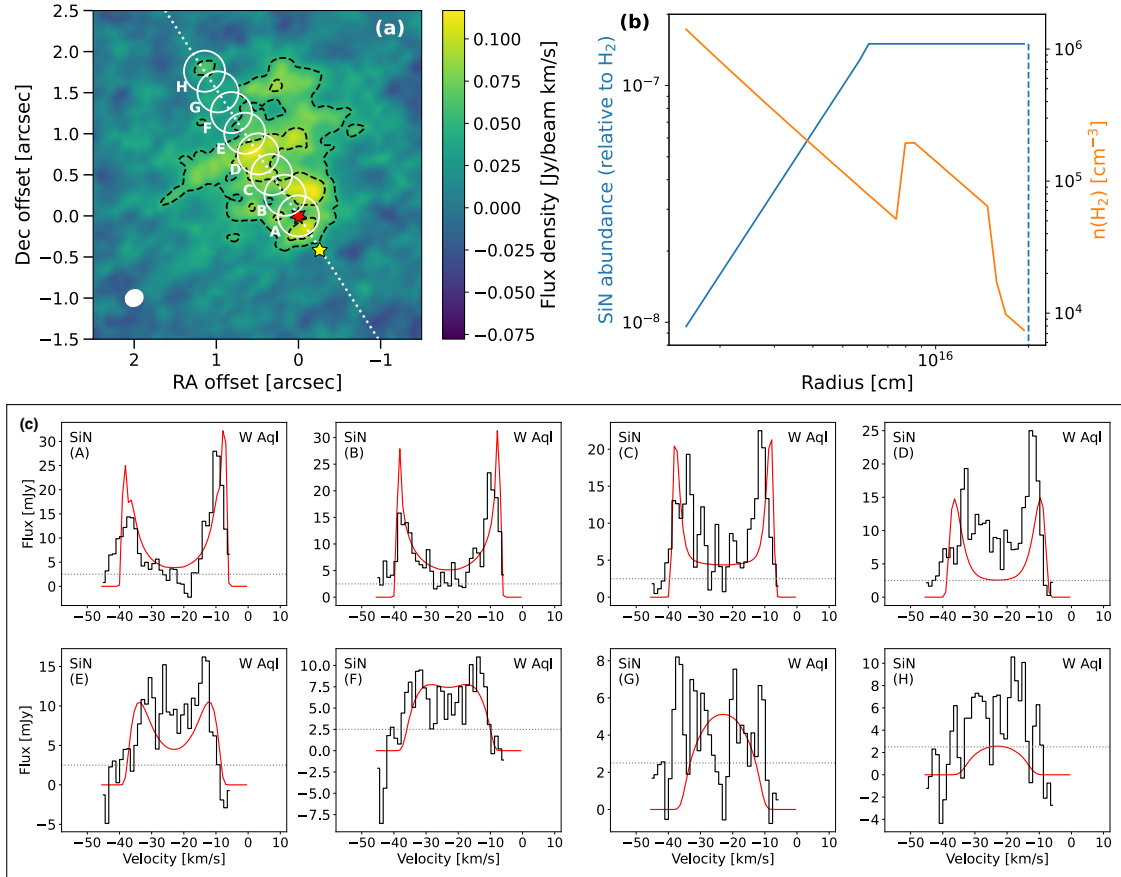


Figure A.11: **(a)** SiN zeroth moment map, as shown in Fig. 1, with the circular extraction apertures, labelled A to H, used to obtain spectra for radiative transfer modelling. The white dotted line lies at an angle of north 33° east, passing through the continuum peak. **(b)** SiN abundance (blue) and H<sub>2</sub> number density (orange) for the region of the CSE for which we model SiN. The dashed blue line represents the edge of the model, beyond which we do not include any SiN. **(c)** SiN spectra (black histograms) extracted for the regions (A to H) defined in (a) plotted with the results of the radiative transfer model (red curves). For these spectra rms = 2.5 mJy and is indicated by the dotted grey lines.

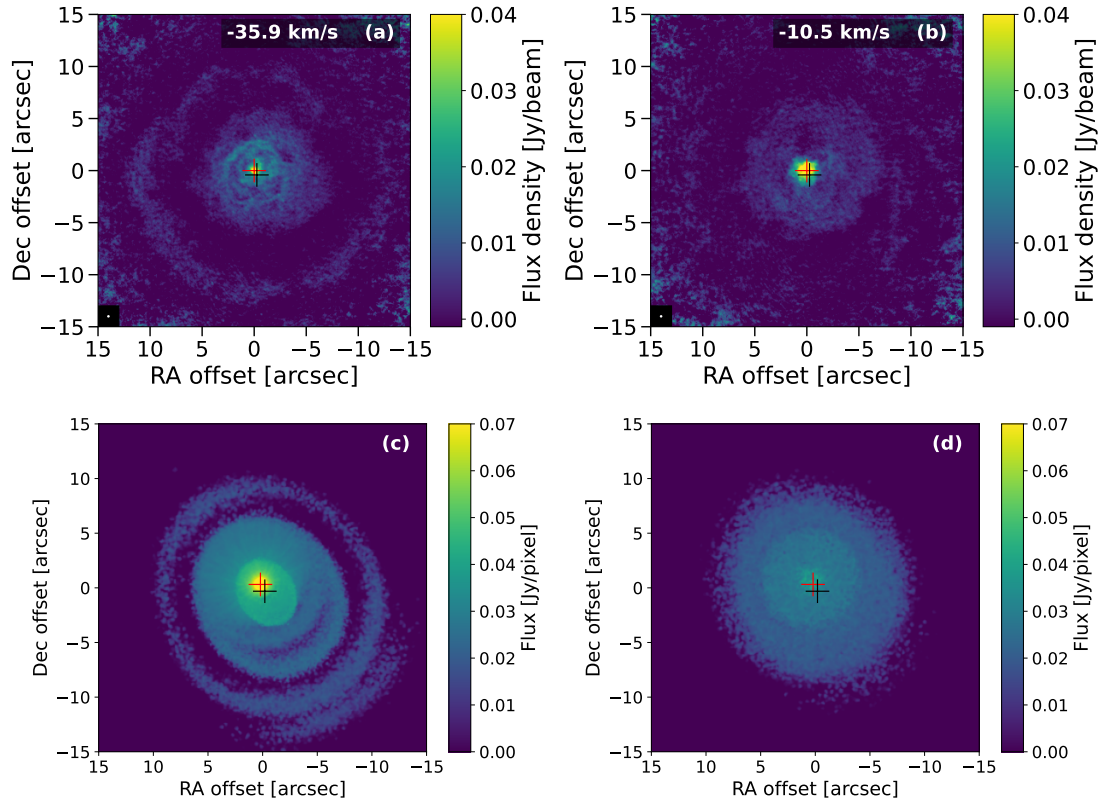


Figure A.12: Plots showing that blue (a and c) and red (b and d) channels equidistant from the stellar LSR velocity ( $v_{\text{LSR}} = -23 \text{ km s}^{-1}$ ) in velocity space do not exhibit identical CO emission patterns. The ALMA observations (a and b) show an elongated emission region on the blue side (a) and an approximately round emission region on the red side (b). The same pattern is mimicked in the red (c) and blue (d) channels of the hydrodynamic model processed with MCFOST. The red and black crosses correspond to the locations of the AGB and F9 stars. Note that the modelled and observed positions do not exactly correspond. Details are given in Methods 3.7.

Table A.2: Physical parameters of the W Aql system

<i>AGB and circumstellar parameters</i>	
LSR velocity, $v_{\text{LSR}}$	$-23 \text{ km s}^{-1}$
Mass-loss rate, $\dot{M}$	$3 \times 10^{-6} M_{\odot} \text{ yr}^{-1}$
Stellar effective temperature, $T_{\text{eff}}$	2300 K
Luminosity, $L_{\star}$	$7500 L_{\odot}$
Stellar radius, $R_{\star}$	8.3 mas
<i>System parameters</i>	
Distance, $D$	395 pc
AGB mass, $M_{\text{AGB}}$	$1.6 M_{\odot}$
F9 mass, $M_{\text{F9}}$	$1.06 M_{\odot}$
<i>Orbital parameters from ALMA observations</i>	
Orbital period, $T$	$1082^{+89}_{-108} \text{ years}$
Time since periastron, $\Delta t$	$172 \pm 22 \text{ years}$
Rotation in the plane of the sky, $\omega$	$120 \pm 5^{\circ}$
Inclination, $i$	$90 \pm 7^{\circ}$

Table A.3: Possible orbital solutions for the W Aql system.

$e$	$r_p$ [cm]	$r_p$ [au]	$a$ [au]	$T$ [years]	$\Delta t$ [years]	$t_{\text{close}}$ [years]
0.98	$4.5 \times 10^{13}$	3.0	150	1131	157	1.9
0.97	$6.5 \times 10^{13}$	4.3	145	1069	163	3.3
0.96	$8.5 \times 10^{13}$	5.7	142	1038	167	5.0
0.96	$9.0 \times 10^{13}$	6.0	150	1131	165	5.4
0.95	$1.1 \times 10^{14}$	7.4	147	1093	170	7.3
0.94	$1.3 \times 10^{14}$	8.7	145	1069	174	9.3
0.93	$1.5 \times 10^{14}$	10	143	1051	179	12
0.93	$1.6 \times 10^{14}$	11	153	1158	177	13
0.92	$1.7 \times 10^{14}$	11	142	1038	183	14
0.92	$1.8 \times 10^{14}$	12	150	1131	181	15
0.91	$1.9 \times 10^{14}$	13	141	1028	187	16
0.91	$2.0 \times 10^{14}$	13	149	1110	186	18

Notes:  $e$  is the eccentricity,  $r_p$  is the periastron,  $a$  is the semimajor axis,  $T$  is the orbital period,  $\Delta t$  is the time since the most recent periastron, and  $t_{\text{close}}$  is the amount of time the two stars spend close together (see Methods 3.9).

## 1704 B Supplementary Materials

### 1705 B.1 Radiation pressure on dust

1706 Here we compare the contribution to the radiation pressure on dust from the AGB and  
 1707 F9 stars. The ratio of the radiation pressure force on dust grains,  $F_{P_r} = |\vec{F}_{P_r}|$ , over the  
 1708 gravitational attraction,  $F_{\text{grav}} = |\vec{F}_{\text{grav}}|$ , is defined as

$$\Gamma = \frac{F_{P_r}}{F_{\text{grav}}} \simeq \frac{\sigma_d \bar{Q} \Psi}{4\pi c m_{\text{dust}} G M_\star} L_\star = \left( \frac{\bar{Q} \Psi}{3\pi c a \rho_d G} \right) \frac{L_\star}{M_\star} \quad (17)$$

1709 where  $\sigma_d = \pi a^2$  is the cross-section of the assumed spherical grain, with  $a$  the radius,  
 1710  $\bar{Q} = 2 \times 10^{-2}$  is the mean radiation pressure efficiency of the grains [111],  $\Psi = 2 \times 10^{-3}$   
 1711 is the dust to gas ratio [21],  $c$  is the speed of light,  $m_{\text{dust}} = \frac{4}{3}\pi a^3 \rho_d$  is the mass of  
 1712 a dust grain (derived from volume, assuming a sphere, and a specific dust density of  
 1713  $\rho_d = 3.3 \text{ g cm}^{-3}$ ), and  $M_\star$  and  $L_\star$  are the stellar mass and luminosity. A dust driven  
 1714 wind is achieved for  $\Gamma > 1$ .

1715 When comparing the ability of the AGB and F9 stars to drive the wind through  
 1716 radiation pressure, the properties in brackets on the right-hand side of equation 17 do not  
 1717 change, so the dust driving potential comes mainly from the luminosity of the star. For  
 1718 the AGB star, the luminosity is  $7500 L_\odot$  [21], while for the F9 star it is  $\sim 1.5 L_\odot$ . We use  
 1719 the system mass of  $2.66 M_\odot$  as this is the maximum possible gravitational force that must  
 1720 be overcome by the radiation pressure. For relatively small grains with  $a = 0.03 \mu\text{m}$ ,  
 1721 we find  $\Gamma_{\text{AGB}} = 1.1$  and  $\Gamma_{\text{F9}} = 2.3 \times 10^{-4}$ , indicating that the F9 star's contribution to  
 1722 driving the wind is negligible.

### 1723 B.2 Anisotropic mass loss

1724 Recent observational studies of AGB stellar discs and inner winds at near-infrared wave-  
 1725 lengths have shown asymmetric and clumpy surface brightnesses [112, 113, 114, 115,  
 1726 116]. These broadly agree with 3D hydrodynamical simulations of AGB atmospheres,  
 1727 which predict the formation of large convective shells in the low-gravity environment  
 1728 of the AGB star's extended atmosphere, resulting in a clumpy and non-spherical atmo-  
 1729 spheric structure and asymmetric dust formation [117, 118, 119]. Similar asymmet-  
 1730 ric features have also been observed in the millimetre range with ALMA, in both the  
 1731 continuum emission and for molecular lines that originate in, or close to, the stellar  
 1732 atmosphere [120, 121, 122, 123]. A recent study of the nearby carbon star CW Leo  
 1733 determined that the asymmetries in the stellar atmosphere and inner wind are unlikely  
 1734 to have been formed as a result of binary interactions, but rather as a result of varying  
 1735 temperature and density conditions caused by convection cells [123]. This is despite the  
 1736 larger-scale shells observed around this star being thought to have formed as a result

1737 of binary interactions [71]. In light of these observational and modelling results, we  
1738 analysed whether the various anisotropies reported in the molecular emission around  
1739 W Aql could be related to random convection cells rather than formed through binary  
1740 interactions.

1741 The asymmetries we see on the largest scales in the molecular emission around  
1742 W Aql are those that we associate with the photodissociation of common species (SiO,  
1743 SiS, CS, HCN) by the F9 companion, as discussed in the Results and in Methods 3.4.7  
1744 and 3.6.4. While we do see some smaller-scale asymmetries in these molecular lines,  
1745 which may have originated as a result of the chaotic distributions of convective cells  
1746 before expanding in the wind (e.g. see the non-uniform distributions of SiS and CS in  
1747 their central channels, shown in Fig. B.18, or the smaller-scale arcs and clumps seen  
1748 in the CO emission in Figs. 3 and A.7), these are unlikely to account for the overall  
1749 asymmetry on a larger scale.

1750 The asymmetric emission detected for SiN, SiC and NS is generally seen on smaller  
1751 scales than the asymmetries in the common species discussed above and has higher de-  
1752 grees of asymmetry. Such an arc-like distribution is unlikely be formed as a result of  
1753 localised (and necessarily very specific, based on the observations) fluctuations of tem-  
1754 perature and density caused by convective cells. If these asymmetries were formed as a  
1755 result of random fluctuations, we would expect them to be formed in several directions  
1756 (e.g. see [119]), not just in an arc on one side of the AGB star, and would expect ad-  
1757 ditional similar fluctuations to have occurred in the  $\sim 170$  years since the formation of  
1758 the observed SiN arc. For example, the model by Freytag et al. [119] that most closely  
1759 resembles W Aql has events of elevated dust production on a time scale of a few to tens  
1760 of years. We also note that the formation of both SiN and SiC is driven by  $\text{Si}^+$  (Methods  
1761 3.6.1), which has an ionisation energy of 8.2 eV [124] and hence is most easily ionised  
1762 by UV photons. Ergo, as discussed in Results and Methods 3.4.3 and 3.6.1, the for-  
1763 mation of SiN in an arc to one side of the AGB star suggests formation during a close  
1764 periastron interaction between the AGB and F9 stars.

1765 However, the distribution of SiN emission seen in the zeroth moment map and PV  
1766 diagram in Fig. 1 does not reveal a perfectly uniform structure. For example, there are  
1767 regions of brighter flux in the zeroth moment map, enclosed in the  $5\sigma$  contours, which  
1768 are not symmetric along the axis connecting the AGB and F9 stars. Similarly, the PV  
1769 diagram is not perfectly symmetric across the LSR velocity axis and shows clumps of  
1770 brighter emission. These clumpy asymmetries are more likely to be caused by variations  
1771 in density and temperature driven by chaotic motions of convection cells, similar to the  
1772 clumpy emission seen in the inner wind of CW Leo [123]. It is also possible that some  
1773 of the enhancements were caused by the interaction between the shock created by the  
1774 companion's passage and the pulsation of the AGB star, as modelled in the simulations  
1775 of Aydi et al [125]. Such varying conditions could explain why, for example, there is  
1776 only one bright clump of NS in the PV diagram (Fig. B.15) but several bright clumps of

1777 SiN and SiC.

1778 We conclude that the large arc-like structure of the molecular emission is more con-  
1779 sistent with enhanced formation during the periastron interaction of the AGB and F9  
1780 stars. However, anisotropic mass loss processes may also have contributed to the pre-  
1781 cise small-scale structure of the SiN, SiC and NS emission.

### 1782 B.3 Additional figures

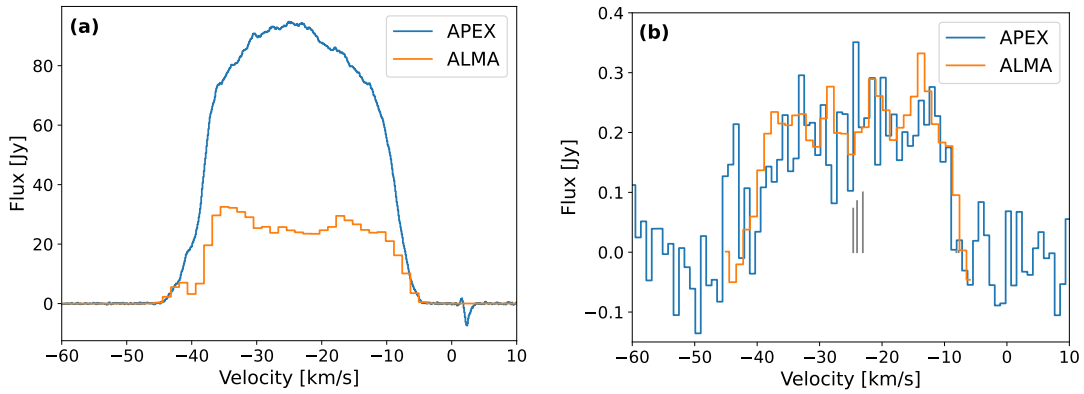


Figure B.13: A comparison between ALMA (orange) and APEX (blue, [47]) observations of the same molecular lines. **(a)** Spectra of CO ( $J = 2 \rightarrow 1$ ), showing that around 66% of the CO flux was not recovered with ALMA for a spectrum extracted from an aperture with radius  $5.4''$  from the low-resolution ALMA data. **(b)** Spectra of SiN ( $N, J = 6, 13/2 \rightarrow 5, 11/2$ ) extracted from an aperture with radius  $2.5''$ , showing that all the SiN flux has been recovered by ALMA. The vertical grey lines indicate the relative velocities and intensities of the hyperfine components of the SiN, assuming an LSR velocity of  $-24 \text{ km s}^{-1}$ .



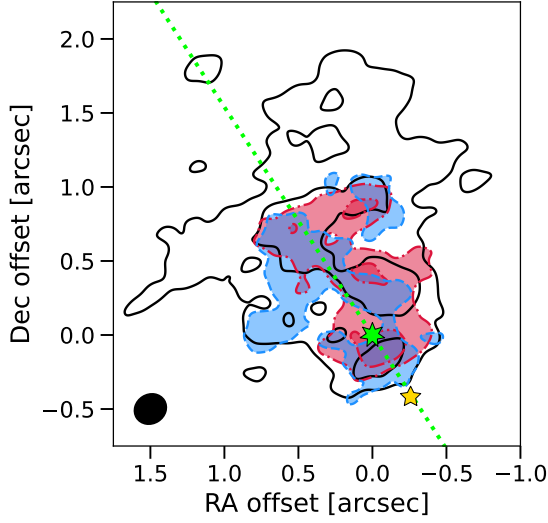


Figure B.14: The blue- and red-shifted components of the SiN emission overplotted with the full zeroth moment map contours from Fig. 1a. In all cases, contours are at levels of  $3$  and  $5\sigma$ . The synthetic beam size is given by the black ellipse in the bottom left corner and the locations of the AGB and F9 stars are indicated by the green and yellow stars, respectively. The dotted green line is at north  $33^\circ$  east.

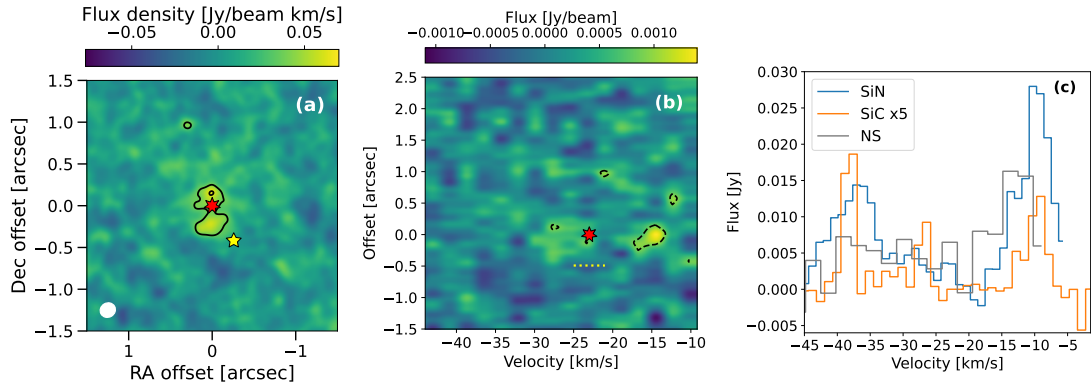


Figure B.15: **(a)** Zeroth moment map of NS towards W Aql with contours at levels of  $3$  and  $5\sigma$ . North is up and east is to the left. The position of the AGB star is indicated by the red star at  $(0,0)$  and the location of the F9 companion is indicated by the yellow star to the south-west. The white ellipse in the bottom left corner indicates the size of the synthesised beam. **(b)** Position-velocity diagram of NS taken with the same wide slit as used for SiN (Fig. 1). The position and LSR velocity of the AGB star is indicated by the red star and the horizontal dotted yellow line indicates the present offset of the F9 star. **(c)** Spectra of the NS, SiN and SiC lines given in Table 1. All lines were extracted for circular apertures with radii  $0.25''$ , centred on the continuum peak. The flux of the SiC spectrum is multiplied by 5 to allow for a more direct comparison to SiN and NS.

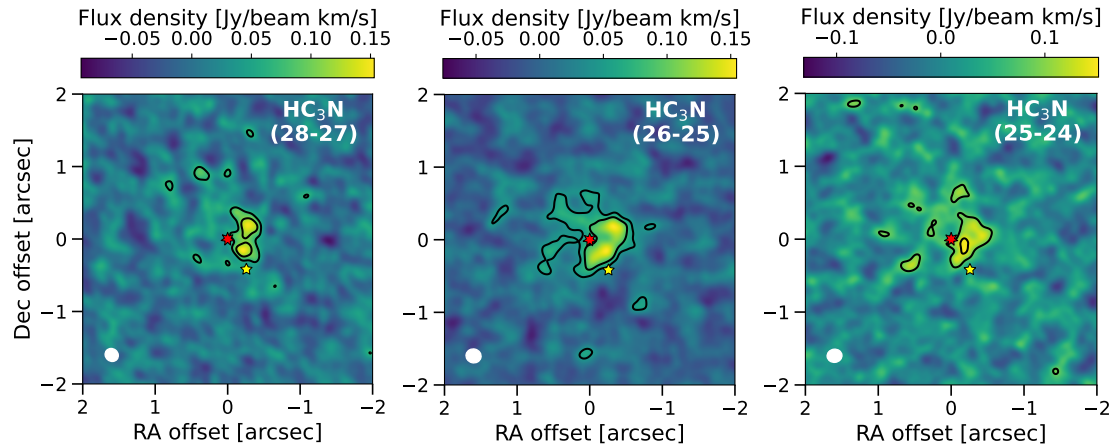


Figure B.16: Zeroth moment maps of  $\text{HC}_3\text{N}$  towards W Aql with contours at levels of  $3$  and  $5\sigma$ . The transition is given in the top right of each map. North is up and east is to the left. The position of the AGB star is indicated by the red star at  $(0,0)$ , also corresponding to the continuum peak, and the location of the F9 companion is indicated by the yellow star to the south-west. The white ellipse in the bottom left corner indicates the size of the synthesised beam.

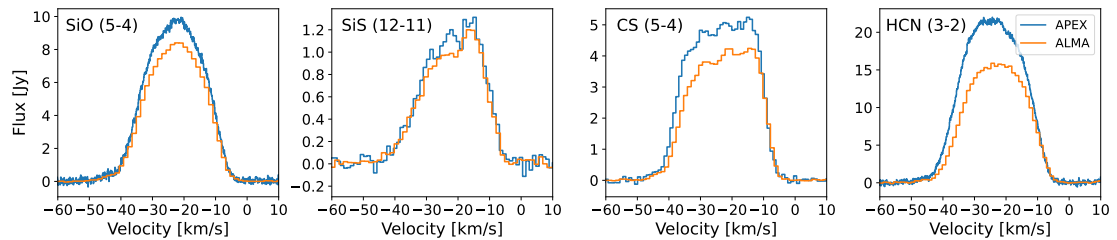


Figure B.17: Comparisons of ALMA and APEX data for SiO, SiS, CS and HCN, showing relatively low levels of resolved out flux (10–30%) for the ALMA observations. All ALMA spectra were extracted from apertures with radii of  $5.4''$ .

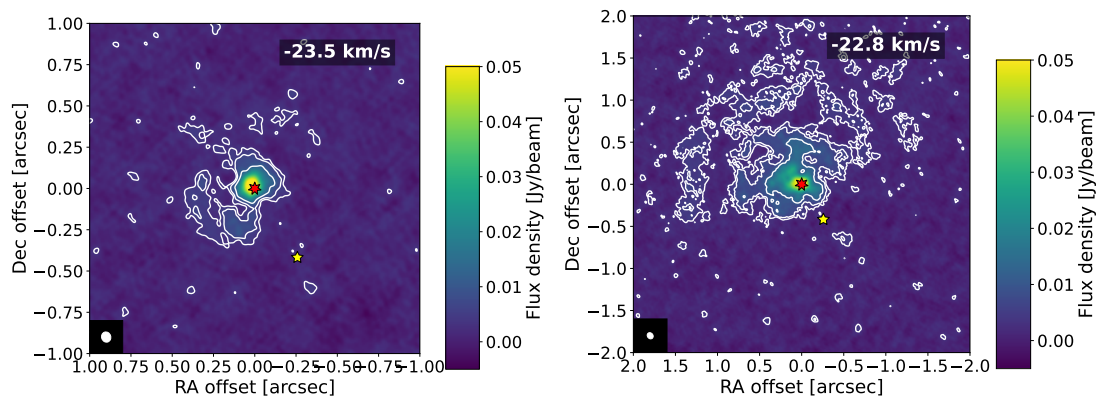


Figure B.18: Plots of the central channels of SiS (left) and CS (right), showing the asymmetric distribution of these molecules caused by the flux from the F9 star. The positions of the AGB and F9 stars are indicated by the red and yellow stars, respectively. The channel velocities are given in the top right corners and the beam is shown in the bottom left corner. Contours are plotted for levels of 3, 5, and  $10\sigma$ . North is up and east is left.

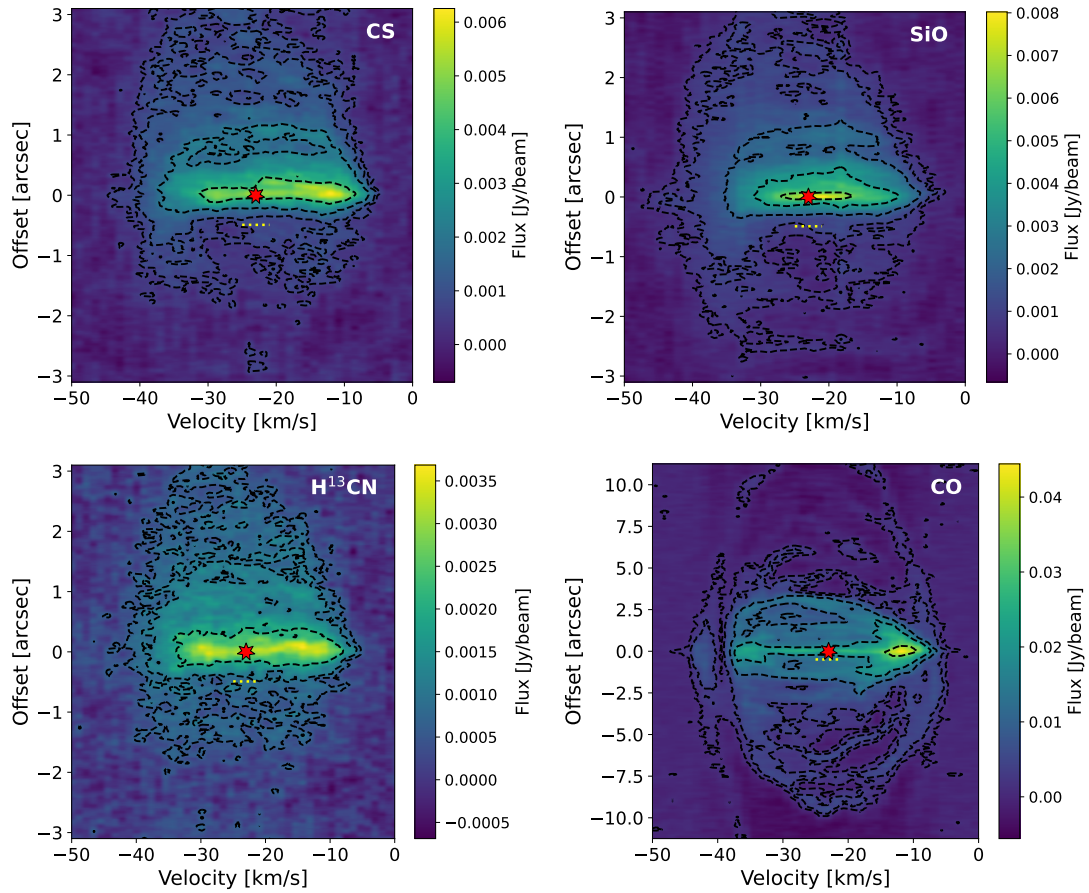


Figure B.19: Position-velocity diagrams of CS, SiO, H<sup>13</sup>CN and CO, taken with the same slit that was used for SiN (Fig. 1). The black contours are at levels of 3, 5, 10, 20 $\sigma$ , except for CO, where they are at levels of 3, 10, 30, 50, 100 $\sigma$ . The position and LSR velocity of the AGB star are indicated by the red star and the horizontal dotted yellow line indicates the present offset of the F9 star. Note that the reduced emission at positive offsets for CO is the result of resolved out flux.

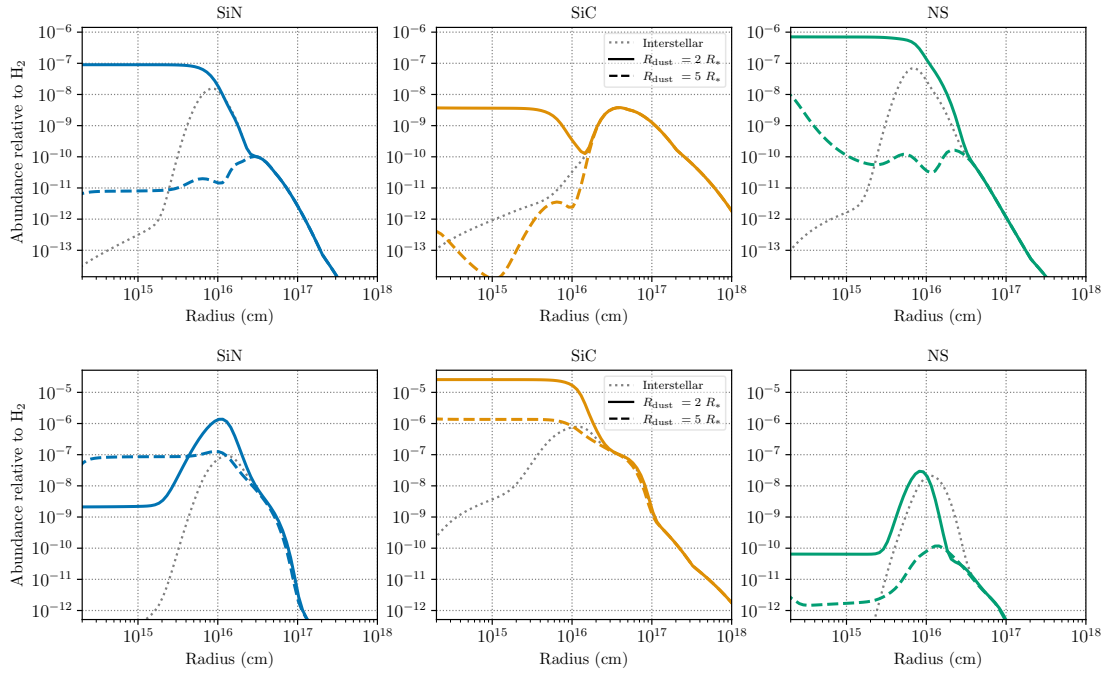


Figure B.20: Predicted abundances of SiN (*left*), SiC (*middle*) and NS (*right*) based on chemical models for a stellar wind with a similar density as W Aql. Plots show the predicted abundances in the absence of a companion (*grey dotted lines*), and for when the effects of the companion are felt from  $5R_{\star}$  (*dashed coloured lines*) and  $2R_{\star}$  (*solid coloured lines*). Predictions for an oxygen-rich outflow are shown in the *top* row and for a carbon-rich outflow in the *bottom* row. Plotted models assume a 6000 K companion and are for a clumpy (two-component) outflow with full details given in [4].

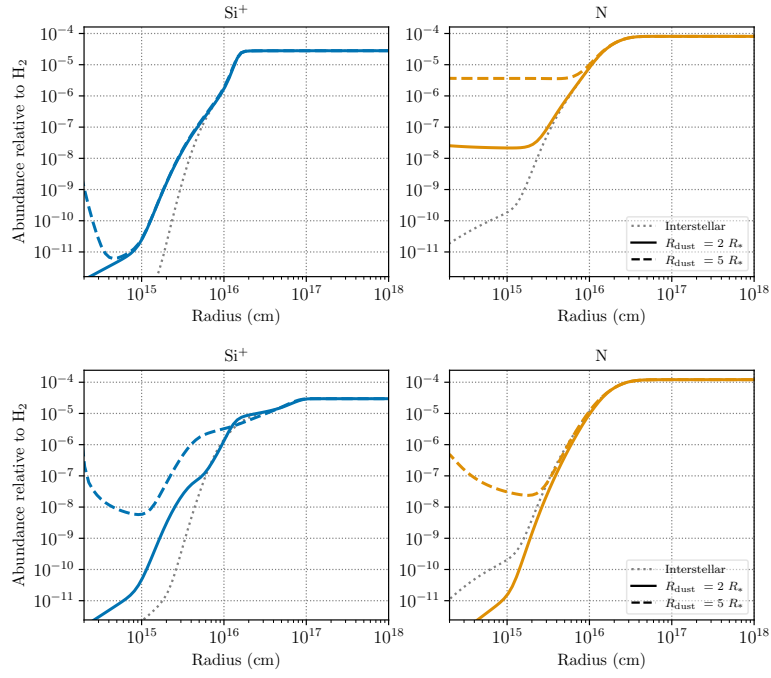


Figure B.21: Predicted abundances of  $\text{Si}^+$  (*left*) and  $\text{N}$  (*right*) based on chemical models for a stellar wind with a similar density as W Aql. Plots show the predicted abundances in the absence of a companion (*grey dotted lines*), and for when the effects of the companion are felt from  $5R_*$  (*dashed coloured lines*) and  $2R_*$  (*solid coloured lines*). Predictions for an oxygen-rich outflow are shown in the *top* row and for a carbon-rich outflow in the *bottom* row. Plotted models assume a 6000 K companion and are for a clumpy (two-component) outflow with full details given in [4].

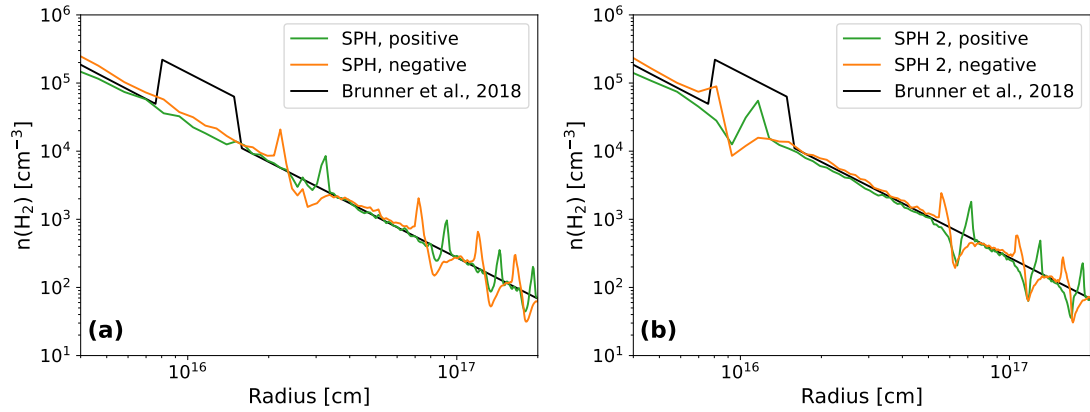


Figure B.22: Plots of number density in the hydrodynamic models along the  $x$ -axis (with  $y = z = 0$ ), showing number densities with increasing distance from the AGB star in both the positive (green) and negative (orange)  $x$  directions (see Figures 3c and B.26a for the definition of the axes), and compared with the spherically symmetric model of Brunner et al. [23] (black). The innermost regions are excluded owing to limitations in the resolutions of our models. **(a)** The number density for our main hydrodynamic model (see Methods 3.7 for details); **(b)** As for (a) but plotted for a second model with the orbital parameters derived in Methods 3.9 and neglecting the more complex structures formed in the companion's wake. For this model, the location of the first higher-density circle agrees well with the location of the overdensity found from low-resolution ALMA observations [23].

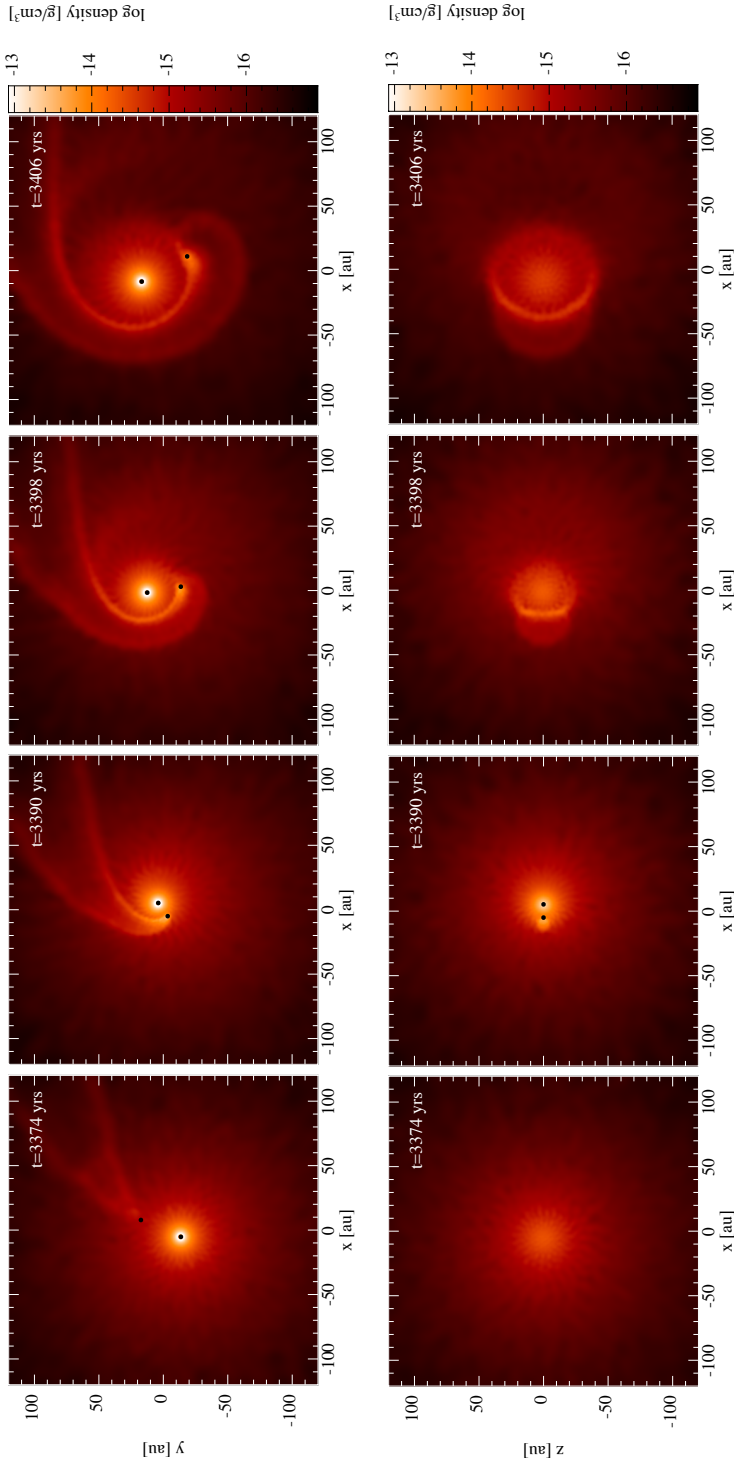


Figure B.23: Plots of the density in the inner regions of the hydrodynamic model at snapshots taken before, during and after the periastron passage. The time since the start of the simulation is shown in the top right hand corner of each plot. The top row of plots show a slice through the orbital plane and the bottom row shows the same time steps but for a slice perpendicular to the orbital plane.



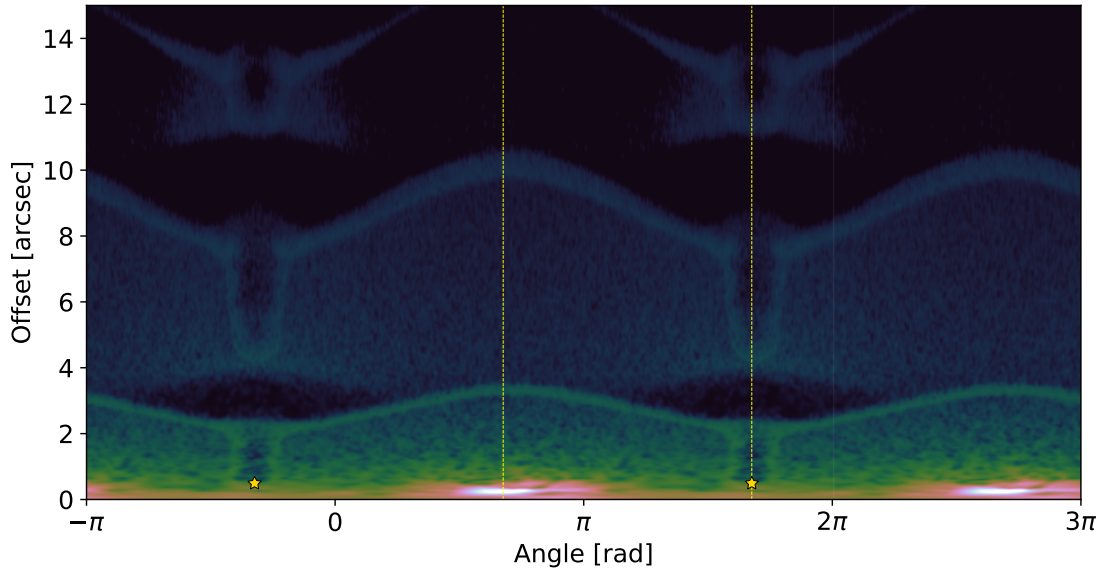


Figure B.24: Plot of the modelled radial emission distribution against angle for the central channel of CO generated from the MCFOST radiative transfer output of our Phantom model. One full revolution is shown in the centre (0 to  $2\pi$ ) and half a revolution is shown on either side ( $-\pi$  to 0 and  $2\pi$  to  $3\pi$ ) to show how the structures extend onwards, and to match the equivalent plot constructed for the ALMA observations in Figs. A.8 and B.25. The location of the F9 star in the model is indicated by the yellow star and the yellow dotted line passes through both stars and is plotted in the central winding to guide the eye. Similar sinusoidal features are seen to those in the ALMA observations.

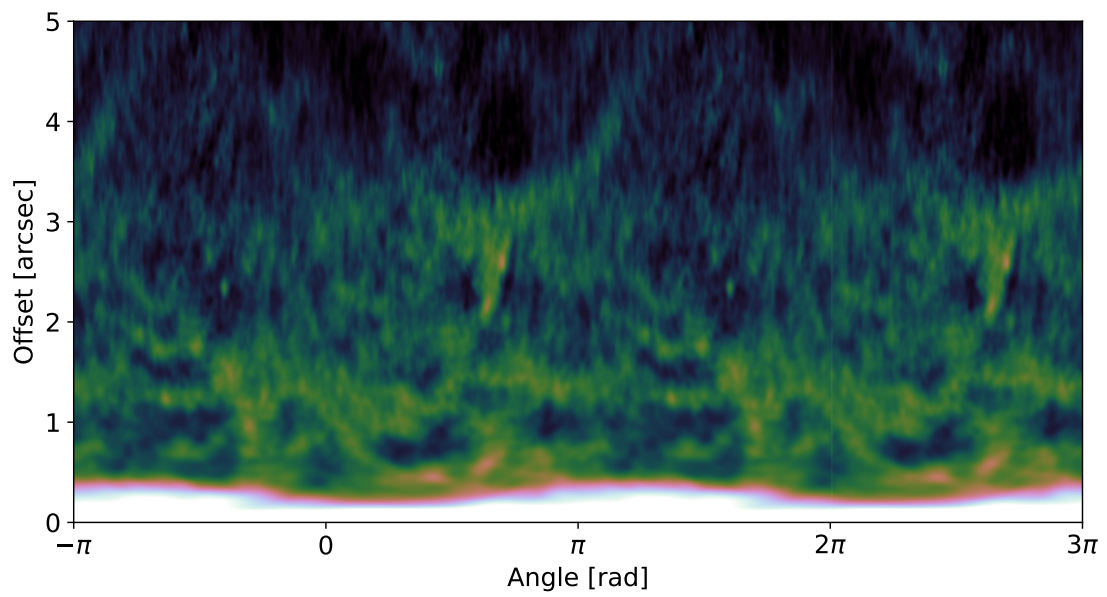
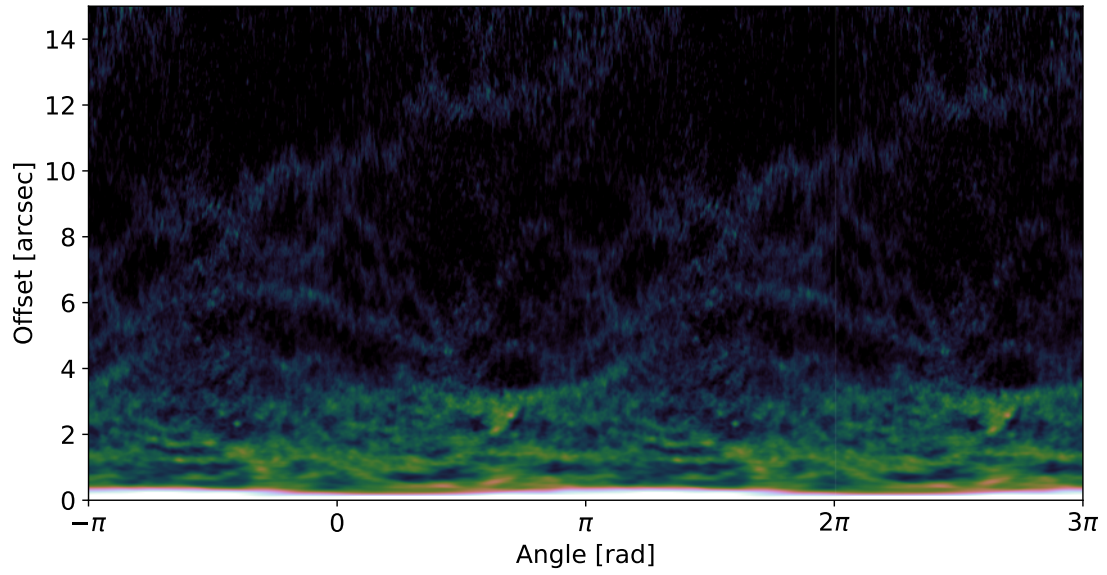


Figure B.25: As for Fig. A.8 but without the additional annotations to highlight structures.

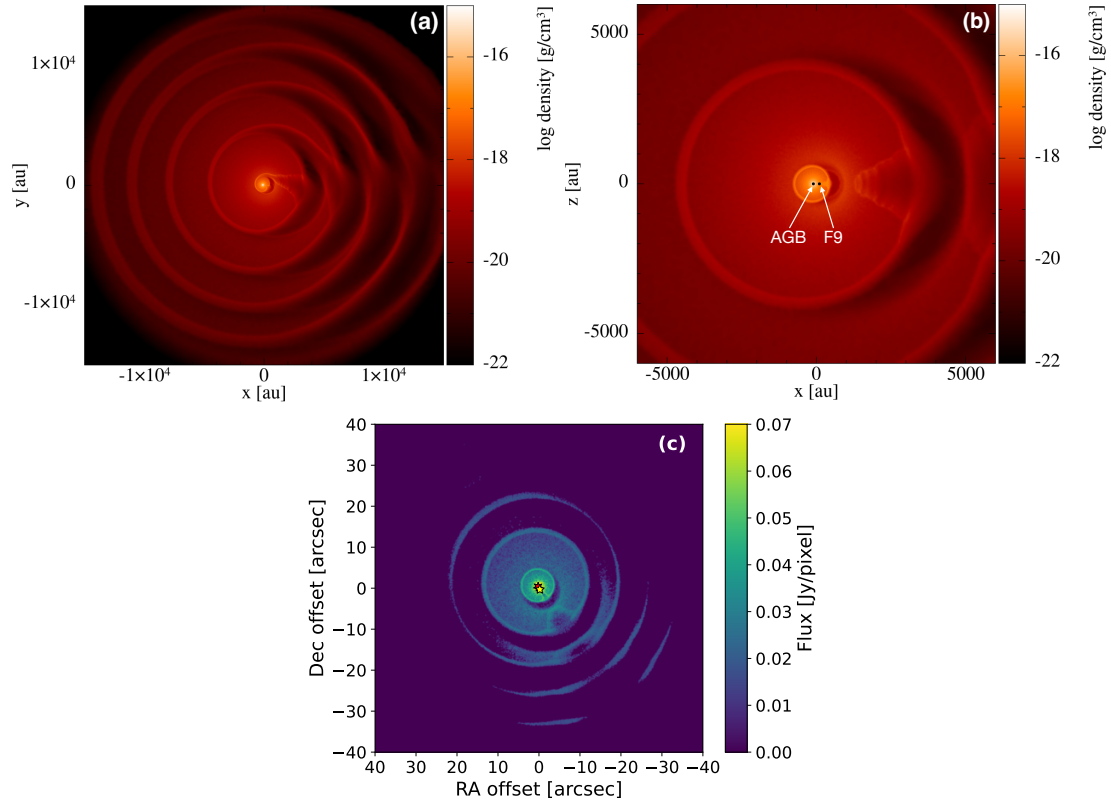


Figure B.26: **(a)** Density distribution in a 2D slice through the orbital plane ( $z = 0$ ) from a 3D SPH model with masses  $M_{\text{AGB}} = 1.6 M_{\odot}$  and  $M_2 = 1.06 M_{\odot}$ , eccentricity  $e = 0.92$ , and semimajor axis  $a = 125$  au; i.e. a face-on view of Fig. 3c. See Methods 3.7 for more details. **(b)** The central part of a slice perpendicular to the orbital plane of the same model, i.e. the central part of Fig. 3c with the stars labelled and the  $x$  and  $y$  axes chosen to match the scale of Fig. 3a. **(c)** The full emission distribution predicted by MCFOST for the central channel at the LSR velocity, based on the SPH model, extending further than the field of view of our ALMA observations.

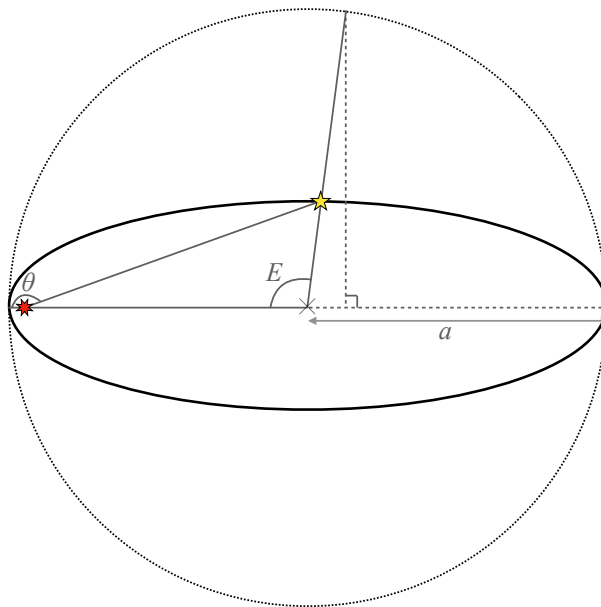


Figure B.27: A schematic view of the W Aql system looking down onto the orbital plane in the frame of reference of the AGB star (red). The solid black ellipse shows a representative orbit of the F9 star (yellow) and the cross shows the centre of the orbital ellipse. The semimajor axis,  $a$ , and the angles  $\theta$  and  $E$  are also shown, with the dotted outer circle having a radius equal to the semimajor axis.